Numerical and Experimental Studies of Air and Particle Flow in the Realistic Human Upper Airway Models

A thesis submitted in fulfilment of the requirement for the degree of Doctor of Philosophy

Huafeng Li
B.E., M.E.S

School of Aerospace, Manufacturing & Mechanical Engineering
RMIT University
August 2009

Author's Declaration

I hereby declare that this submission is my own work and to the best of my knowledge it contains no materials previously published or written by another person, nor material which to a substantial extent has been accepted for the award of any other degree or diploma at RMIT or any other educational institution, except where due acknowledgement is made in the thesis. Any contribution made to the research by others, with whom I have worked at RMIT or elsewhere, is explicitly acknowledged in the thesis.

I also declare that the intellectual content of this thesis is the product of my own work, except to the extent that assistance from others in the project's design and conception or in style, presentation and linguistic expression is acknowledged.

……

Huafeng Li

Abstract

The human upper airway structure provides access of ambient air to the lower respiratory tract, and it warms and humidifies inspired air to near body core temperature and full water saturation. It also acts as an efficient filter to cleanse inspired air of dust bacteria, and other environmental pollutants. When air passes through airway passages, it constantly changes direction, which may lead to flow separation, recirculation, secondary flow and shear stress variations along the airway surface. Therefore, it is essential to understanding the air transport processes within the upper airway system. The functions are respiratory defence mechanisms that protecting the delicate tissues of the lower airway from the often harsh conditions of the ambient air. While protecting the lower respiratory system, however, the upper airway itself becomes susceptible to various lesions and infections from filtration of environmental pollutants. Inhaled particle pollutants have been implicated as a potential cause of respiratory diseases. In contrast, inhalation of drug particles deposited directly to the lung periphery results in rapid absorption across bronchopulmonary mucosal membranes and reduction of the adverse reactions in the therapy of asthma and other respiratory disorders. For this purpose, it is desirable that the particles should not deposit in the upper airways before reaching the lung periphery. Therefore, accurate prediction of local and regional pattern of inhaled particle deposition in the human upper airway should provide useful information to clinical researchers in assessing the pathogenic potential and possibly lead to innovation in inhalation therapies.

With the development of the increasing computer power and advancement of modeling software, computational fluid dynamics (CFD) technique to study dilute gas-particle flow problems is gradually becoming an attractive investigative tool. This research will provide a more complete picture of the detailed physical processes within the human

upper airway system. Owing to the significant advancements in computer technologies, it will allow us to efficiently construct a full-scaled model integrating the various functional biological elements including the nasal, oral, laryngeal and more generations of the bifurcation of the human upper airway system through state-of-the-art fine resolution imagining methodologies. A significant advantage of this human model is that the differences in airway morphology and ventilation parameters that exist between healthy and diseased airways, and other factors, can be accommodated. This model will provide extensive experimental and numerical studies to probe significant insights to the particle deposition characteristics within the complex airway passages and better understanding of any important phenomena associated with the fluid-particle flow. It will also lead to an improved understanding of fluid/particle transport under realistic physiological conditions. New concepts and numerical models to capture the main features observed in the experimental program and innovative techniques will be formulated. The ability to numerically model and a better physical understanding of the complex phenomena associated with the fluid dynamics and biological processes will be one of the major medical contributions especially targeting drug delivery and health risk analysis. Its biomedical engineering significance lies in the fact that this will enable us to accurately evaluate potential biological effects by the inhaled drug particles, facilitating new drug research and development. Researchers can also be significantly benefited by the wealth of experimental data and observations towards improvements of the numerical models for better prediction of the particle deposition in the human upper airway system under different physiological conditions.

Acknowledgements

First and foremost, I would like to express my deepest gratitude to my supervisor, Professor Jiyuan Tu of the School of Aerospace, Manufacturing & Mechanical Engineering in RMIT University for his fruitful, organised and patient guidance in every aspect of my research work. The immense influence he presented in shaping my research attitude and approach can never be overestimated.

I would also like to express sincere gratitude to my co-supervisor, Professor Charlie Xue of School of Health Sciences, RMIT University, for the guidance in the scientific writing.

I would also like to express sincere thanks to Dr William Yang of Commonwealth Scientific and Industrial Research Organization, and Dr Li Chen of Defence Science and Technology Organisation, for their kindly help in developing my knowledge in experimental and numerical approaches.

I would like to thank members of RMIT CFD group and my colleagues in the research office who have always provided assistance where necessary.

A special acknowledgement to my family back in China for their care and encouragement throughout my student years, my mother Fuling Zhang for her concern and love, my father Zhen Li for his constant motivation and support, and my wife Jie Meng for her love and encouragement.

List of Figures

List of Tables

List of Publications

Journal paper

L. T. CHOI, J. Y. TU, **H. F. LI**, and F. THIEN, 2007F. Flow and Particle Deposition Patterns in a Realistic Human Double Bifurcation Airway Model, *Inhalation Toxicology*, 19:117-137.

K. Inthavong, Z.F. Tian, **H.F. Li**, J.Y. Tu, W. Yang, C.L. Xue, and C.G. Li, 2006, A numerical study of spray particle deposition in a human nasal cavity, *Aerosol Science and Technology*, 40:1034–1045.

Conference paper

H.F. Li, J.Y. Tu, H. Tang, C.G. Li, and C. C. Xue, Aerosol Transport in Laminar and Turbulent Flow in the Human Nasal Cavity, *The International Conference on Computational Methods*, Singapore,15-17 December, 2004.

H. Tang, J.Y. Tu, **H.F. Li**, B. Abu-Hijleh, C.C. Xue, and C.G. Li, Dynamic Analysis of Airflow Features in a 3D Real-anatomical Geometry of the Human Nasal Cavity, *15th Australasian Fluid Mechanics Conference*, Sydney, Australia, 13-17 December 2004.

H.F. Li, Z.F. Tian, J.Y. Tu, W. Yang, G.H. Yeoh, C.L. Xue and C.G. Li, Studies of airflow through a human nasopharynx and pharynx airway, *the Fifth International Conference on CFD in the Process Industries,* Melbourne, Australia, 13-15 December 2006.

H.F. Li, J.Y. Tu, D.K. SHANMUGAM, C.L. Xue and C.G. Li, A CFD study of fluid-particle behaviour in a porous vestibule of a human nasal and pharynx airway, *the Fifth International Conference on CFD in the Process Industries,* Melbourne, Australia,13-15 December 2006.

Nomenclature

A	cross-sectional inlet area
C_D	drag coefficient
D	Diameter
dp	particle diameter
F_D	drag force
k	turbulence kinetic energy
L	Length
Le	eddy length scale
p	pressure
Q	Respiratory rate of inhalation
r	uniform random number
Re	Reynolds number
Re_p	particle Reynolds number
St	Stoke number
t	time
t_{cross}	particle eddy crossing time
t_p	particle relaxation time
T_L	Lagrangian integral time
u	velocity

u_i	velocity vector (same for u_j)
μ	dynamic viscosity
u^g	gas (air) velocity
u^p	particle velocity
U	mean velocity
x_i, x_j, x_k	spatial coordinate system

Greek letters

ρ	density
ω	Pseudo-vorticity
v	kinetic viscosity
τ_e	eddy lifetime
τ_i	Reynolds stress tensor

Subscripts and Superscripts

air	air phase
p	particle phase
g	gas phase
k	turbulent kinetic energy
p	discrete particle phase
t	turbulent phase

Chapter 1: Introduction

1.1 Motivations and Background

The human upper airway structure provides access of ambient air to the lower respiratory tract, and has three main physiological functions. First, the upper airway warms and humidifies inspired air to near body core temperature and full water saturation. Second, it acts as an efficient filter to cleanse inspired air of dust bacteria, and other environmental pollutants (Proctor, 1982). Third, odor perception, the key function of the nose starts with the transport of volatile chemical molecules by airflow to the olfactory receptors. When air passes through airway passages, it constantly changes direction, which may lead to flow separation, recirculation, secondary flow and shear stress variations along the airway surface. Therefore, it is essential to understanding the air transport processes within the upper airway system.

Also, the first two functions are respiratory defense mechanisms that protecting the delicate tissues of the lower airway from the often harsh conditions of the ambient air. While protecting the lower respiratory system, however, the upper airway itself becomes susceptible to various lesions and infections from filtration of environmental pollutants. Inhaled particle pollutants have been implicated as a potential cause of respiratory diseases (Pope et al., 1995; Kreuzer et al., 2000; Balásházy et al., 2003). Deposition of inhaled particle pollutants can result in acute bronchoconstriction in asthmatics (Gonda, 1997), and even lung cancer (Spencer, 1985). Consequently, knowledge regarding particle deposition processes in the upper airway is important in inhalation toxicology applications. In contrast, inhalation of drug particles deposited

directly to the lung periphery results in rapid absorption across bronchopulmonary mucosal membranes and reduction of the adverse reactions in the therapy of asthma and other respiratory disorders (Smith and Bernstein, 1996). For this purpose, it is desirable that the particles should not deposit in the upper airways before reaching the lung periphery. This is because excessive deposition of drug particles in the upper airways will cause less therapeutic effects in the lung or local side effects in the upper airways, which may lead to considerable additional treatment costs and reduce adherence to treatment. Currently marketed inhalation therapies can only deliver 10-20% of a drug load into the lung with an effective inhalation (Clark, 1995) and Roland el al. (2004) reviewed that the extra drug load (80-90%, the rest of the drug) for certain types of drug can cause side effects to patient. Therefore, accurate prediction of local and regional pattern of inhaled particle deposition in the human upper airway should provide useful information to clinical researchers in assessing the pathogenic potential and possibly lead to innovation in inhalation therapies.

The deposition characteristics of inhaled particles are strongly affected by the nature of fluid motion within the human upper airways. For example, increase in the respiratory flow rate through the nose/mouth can lead to enhanced inertial deposition of particles, whereas reduction of the flow rate can result in gravitational deposition. Other parameters that also influence the transportation and deposition of inhaled particles include particle size and density, particle tendency to agglomerate, particle delivery mechanisms, as well as turbulent and fluctuating levels in the airflow. Improper choice of any of these parameters can cause mal-deposition of the drug particles thereby reducing their effectiveness, or worse may contribute to undesired/unwanted side effects. Moreover, when air flows through the human nasal or mouth cavity, it may

result in flow separation, recirculation, secondary flow, and shear stress variations along the cavity/airway surfaces. All of these complex flow behaviours affect significantly the particle deposition characteristics.

For the past decade, advancements in computational models employing the Computational Fluid Dynamics (CFD) techniques have emerged from the simultaneous modelling of the airflow field distribution, particle trajectory and deposition in human airways. Some of the notable works are: Balashazy and Hofmann (1993), Yu et al. (1998), Zhang et al. (2002a,b), Martonen et al. (2002), Gemci et al. (2003) and Matida et al. (2004). In parallel with these computational efforts, a number of important experimental works on particle deposition in the human airways have also been performed, for example, Hahn et al. (1993), Swift and Strong (1996) and Hörschler et al., (2003).

From the above numerical and *in vitro* experimental investigations, all of these research works have thus far provided only incremental progress towards better describing the particle deposition within the human respiratory airway architecture. These studies focused mainly on isolated airway segment and/or simplified geometrical models with ideal flow conditions. In reality, the fluid and particle flow generally do not correspond to these *idealised* investigative models. Importantly, the skewed velocity profiles from upstream airway elements subsequently affect the flow patterns downstream. There is therefore a need to *develop* an integrated model, which warrants all the segments of human upper airways to be combined as a unified respiratory system. This kind of study is also important (Yu et al., 1998) because humans are naturally-born nasal and/or mouth breathers, while laboratory rats, the major surrogates used in

inhalation-exposure experiments, are only nasal breathers. This difference is carefully addressed for the sole purpose of accurate interspecies modelling. Other important factors include investigation of the human oral airway to act as a major obstacle/filter in inhaled medication delivery and on the ratio of nasal flow to oral flow that will affect downstream airway (laryngeal airway) flows and particle transport patterns. The development of an integrated model for the human respiratory upper airway architecture is one of the main objectives of this proposal for extensive experimental and computational studies.

One prevalent problem experienced in numerical modelling is the lack/availability of experimental benchmarking data while using actual airway geometry for validating numerical predictions. Such experimental study is not only deemed necessary for model validation but also crucial towards better understanding of the complex physics involved in the process. A comprehensive experimental study will allow the deposition characteristics, and improvements to the intended drug delivery mechanisms.

1.2 Research objectives

The understanding and prediction of particle transport and deposition characteristics in the human upper respiratory airways is important for targeting the delivery of drug particles or assessing the health risks of inhaled pollutant particles. However, as will be shown in the following of the literature review, there are still many important issues that require to be addressed for better understanding and analysis of the particle flow deposition in the upper respiratory tract. Both experimental and numerical studies have so far employed idealised geometries and flow conditions.

These studies were not in accordance to the actual fluid and particle flow behaviours in the human airway system. Several important effects were neglected: realistic airway geometry for accurate flow description, turbulent fluctuating eddies acting on the particle trajectory ultimately influenced on deposition patterns, and the consideration of mucus of airway and nasal hair affecting the particle deposition. There is a great need for more representative experimental studies of these complex phenomena. New and innovative numerical models are also required further development and formulation towards better prediction of the internal airflow and particle behaviour within the human upper airway system.

The uniqueness of this study is the strong interaction between the numerical simulation and the experimental study to achieve the following aims:

1) Comprehensive *in vitro* experimental studies of the air/particle flow distribution using state-of-the-art Particle Image Velocimetry (PIV); and
2) Development of numerical simulation that can accurately predict both the air and particle flow and deposition patterns under the realistic physiological conditions of the upper airway system.

This research will provide a more complete picture of the detailed physical processes within the human upper airway system. Owing to the significant advancements in computer technologies, it will allow us to efficiently construct a full-scaled model integrating the various functional biological elements including the nasal, oral, laryngeal and more generations of the bifurcation of the human upper airway system through state-of-the-art fine resolution imagining methodologies. A significant advantage of this human model is that the differences in airway morphology and ventilation parameters that exist between healthy and diseased airways, and other

factors, can be accommodated. This model will provide extensive experimental and numerical studies to probe significant insights to the particle deposition characteristics within the complex airway passages and better understanding of any important phenomena associated with the fluid-particle flow. It will also lead to an improved understanding of fluid/particle transport under realistic physiological conditions. New concepts and numerical models to capture the main features observed in the experimental program and innovative techniques will be formulated. The ability to numerically model and a better physical understanding of the complex phenomena associated with the fluid dynamics and biological processes will be one of the major medical contributions especially targeting drug delivery and health risk analysis. Its biomedical engineering significance lies in the fact that this will enable us to accurately evaluate potential biological effects by the inhaled drug particles, facilitating new drug research and development. Researchers can also be significantly benefited by the wealth of experimental data and observations towards improvements of the numerical models for better prediction of the particle deposition in the human upper airway system under different physiological conditions.

1.3 Outline of the dissertation

The rationales of conducting this research, the scope and outlines of this thesis are explained in Chapter 1.

Chapter 2 provides an in-depth review of the background for this research. Some previous studies that highly related to this research are covered. There are mainly two aspects included in flow-particle studies of human airways: experimental and

numerical approaches. The methods used in these approaches, their differences, advantage and disadvantages of the methods are discussed and compared. This literature review provides the main frame of what this research will develop from.

In Chapter 3, since the main focus on this research is the realistic airway being used in the flow-particle study, the airway modeling becomes one of the important parts. Anatomical studies on lower airways are covered here. The classification of generations and the past conducting airway models that have been widely used are introduced. Based on these studies, the important issues in reconstructing the numerical model used in this research are drawn. The methods and reconstructing processes are described in the later section of this chapter.

The fundamental knowledge in numerical modeling and the chosen modeling method are listed and explained in Chapter 4. The rationale of using the chosen turbulence model and the equations being solved in this simulation are listed.

Chapter 5 is focus on the experimental method and measurement, expectantly the PIV system and set-up.

The main body of this research starts in Chapter 6. The development and evaluation of the proposed CFD approach for flow-particle analysis covers the methods in extracting CT data, geometry generation, boundary conditions setting and numerical setup are completed. Results are verified against experimental data. The interaction and phenomena of flow and particles in human airways are investigated based on the obtained results in terms of velocity profile, deposition efficiency and particle deposition pattern. After the evaluation of the CFD approach, a study of comparing two

aerosol delivery methods is conducted and its details of issue (i.e. velocity profile, deposition efficiency and deposition pattern) are incorporated in Chapter 6.

The final chapter concludes the findings and summarizes the significance of the outcomes. Final sections highlight with the potential clinical significance of this study and draw some recommendations for further study.

Chapter 2: Literature Survey

The research conducted on the physics of aerosols and airflow in the human upper airway was mostly incorporated with experimental and numerical studies. The experimental approach has been used to obtain either velocity profile or particle deposition efficiency. Nowadays, computational fluid dynamics (CFD) has been seen as an excellent technique in studying flow and particle behaviors within airways. One obvious advantage is being more economical than experimental method and it can also incorporate more complicated flow and particle phenomena in a more complex airway. There have been numerous numerical studies related to flow profile, deposition efficiency and aerosol deposition pattern, where the close interactions between these three subjects have been researched.

2.1 Experimental studies of airflow and particle transport in human airways

Generally, experimental studies can be categorized into two major approaches, using human cadaver replicate airway models and glass (or silicone) physical airway models. Previously researches used human cadavers to construct their models. For visual observation, smoke, dyed water or xenon were used as the flow medium. Nowadays, state-of-the-art 3D Laser Doppler Velocimetry (LDV) and Particle Image Velocimetry (PIV) have been utilized to investigate the air/particle flow distribution inside the glass or clear silicone models.

From a flow profile perspective, Schroter & Sudlow (1969) observed how secondary flow formed in inspiration and expiration in a single bifurcation glass tube model using dye tracing method under either flat or parabolic profiles entering the inlet.

The profile of secondary motions was dependent on the direction of flow along the tube. Double vortices were formed during inspiration in the daughter tubes. On the contrary, quadruple vortices were created during expiration in the parent tube. Depending upon the curvature of the junction, flow separation with sluggish reversed flow could be observed in daughter tube during inspiration. Axial velocity profiles were highly asymmetric. Peak velocities swung to the inner walls. During expiration, velocity profiles developed an axial peak. Chang & El Masry (1982) measured detailed steady inspiratory velocity profiles in a scaled plastic tube model of the human tracheobronchial airways using anemometer probes, in which the model had 12 pre-drilled stations of measurement and the dimensions of their model were consistent with the lung geometry reported by Horsfield (1974).

Swift and Proctor (1967) mapped out the velocity field of the inspiratory nasal airflow with a Pitot tube and indicated recirculating eddy currents in the superior nose of the model they used. Menon et al. (1984) used the same method and model from Chang and El Masry (1982) and drawn detailed velocity profiles obtained during inspiration and expiration. The results of both studies showed a high degree of asymmetry in all branches, with peak velocities near the inner wall of the bifurcation. Overall, the velocity profiles were more sensitive to airway geometry than to flow rate. However, at low oscillatory frequencies (e.g. 0.25 Hz) of inlet flow, the velocity profiles attained at peak flow rate resemble the profiles seen under steady flow conditions at the corresponding Reynolds number. As the frequency increased (e.g. 4 Hz) the velocity profiles throughout most branches tend to flatten, the details, however, wouldn't be included here because high oscillatory frequency flow is beyond the scope of this research.

Girardin et al. (1983) model measured the velocity field with a Laser Doppler Velocimetry. Velocity fields were mapped in a model of a human nasal fossa by Laser Doppler velocimetry, an innovative, quantitative and noninvasive method of optical anemometry, and by computerization. Other pertinent parameters were also calculated. Studies made at different cross sections of the nasal fossa showed the very definite influence not only of shapes and dimensions but also of direction of flow on velocity fields. The turbinates had a streamlining effect on the velocity fields while the liminal valve had a directional effect. Flow was usually greater in the lower half of the fossa and closer to the septum. The flow was generally turbulent. Velocity fields appear to give more information on intranasal aerodynamics than the calculated flow and Reynolds number for the sections studied, and this allows one to at least theorize that there may be an aerodynamic basis to certain pathological conditions of the nasal airway and its adjoining cavities, the paranasal sinuses, and the eustachian tubes. Hornung et al. (1987) used xenon to image the airflow pattern in their model. Nasal airflow patterns were studied by using xenon 133 gas to image the course taken by air as it flowed through a plastic model of the human nasal cavity. The model was produced from the head of a human cadaver, and was anatomically correct. A needle catheter was used to infuse the radioactive xenon into a continuous flow of room air maintained through the model by a variable vacuum source connected to the nasopharynx. The radioactive gas was infused at one of five release sites in the nostril, and the distribution of the radioactivity was imaged in the sagittal plane with a scintillation camera. The data were organized to show the activity in six contiguous regions of the midnose. For each catheter, release site activity patterns were determined for three flow rates. The results of this experiment showed that both catheter position

and flow rate had significant and reproducible effects on the distribution of radioactivity within the model. Hess et al. (1992) reported flow visualization results of dye-streak photos and their model was made of clear silicone through casting in a death body.

In these studies, the effect of post mortem changes and the introduction of an artificial septum must raise doubts about the validity of the conclusions reached. With medical imaging technology, researchers developed their models non-invasively based on tomographic slices of anatomic structure scanned with modalities, such as computed tomography (CT) or magnetic resonance imaging (MRI). Although anatomically accurate physical models can be reconstructed from the image slices, it is extremely difficult to obtain detailed flow field due to the small and complicated nasal structures. The resolution of the measurements was poor because of the small size of the cast model. To overcome these difficulties, scaled-up physical models were developed.

Hahn et al. (1993) measured the velocity distributions of nasal airway flows from a large-scale nasal model with a hot-film anemometer probe. An anatomically accurate ×20 enlarged scale model of a healthy right human adult nasal cavity was constructed from computerized axial tomography scans for the study of nasal airflow patterns. Detailed velocity profiles for inspiratory and expiratory flow through the model and turbulence intensity were measured with a hot-film anemometer probe with 1 mm spatial resolution. Steady flow rates equivalent to 1100, 560, and 180 ml/s through one side of the real human nose were studied. Airflows were determined to be moderately turbulent, but changes in the velocity profiles between the highest and lowest flow rates suggest that for normal breathing laminar flow may be present in much of the nasal cavity. The velocity measurements closest to the model wall were estimated to be inside the laminar sublayer, such that the slopes of the velocity profiles

are reasonably good estimates of the velocity gradients at the walls. The overall longitudinal pressure drop inside the nasal cavity for the three inspiratory flow rates was estimated from the average total shear stress measured at the central nasal wall and showed good agreement with literature values measured in human subjects.

Schreck et al. (1993) studied the relationship between the pressure losses within the nasal airways and nasal geometry in a 3:1 scale model. The geometry of the model was based on magnetic resonance images of the skull of a healthy male subject. Pressure measurements, flow visualization, and hot-wire anemometry studies were performed at flow rates that, in vivo, corresponded to flows of between 0.05 and 1.50 l/s. The influence of nasal congestion and the collapse of the external nares were examined by using modelling clay to simulate local constrictions in the cross section. A dimensionless analysis of the pressure losses within three sections of the airway revealed the influence of various anatomic dimensions on nasal resistance. The region of the exterior nose behaves as a contraction-expansion nozzle in which the pressure losses are a function of the smallest cross-sectional area. Losses in the interior nose resemble those associated with channel flow. The nasopharynx is modelled as a sharp bend in a circular duct. Good correspondence was found between the predicted and actual pressure losses in the model under conditions that simulated local obstructions and congestion. Gemci et al. (2002) used Phase Doppler Interferometry to measure the axial velocity and turbulent intensity within a simple throat model. They found that turbulence occurred after the laryngeal constriction even for low Reynolds number flows.

Particle Image Velocimetry (PIV) is a powerful technique for measuring fluid velocities over global domains. In brief, the flow passage is constructed using optically

transparent materials. The flow is seeded with tracer particles and is illuminated with a sheet of laser light. By pulse the laser twice in rapid succession, two subsequent positions of the particle are recorded. Post-processing yields two- or three-dimensional instantaneous velocity vectors within the illuminated. Translation of the sheet across the flow elucidates its full three-dimensional character. Hopkins et al. (2000) established the containing a model of the nasal cavity for PIV measured by a combination of RP form CT and curing of clear silicon. Kelly et al. (2000) used particle image velocimetry to determine two-dimensional instantaneous velocity vector fields in parallel planes throughout a model of the nasal cavity that was subjected to a nonoscillatory flow rate of 125 ml/s. The model, which was fabricated from 26 computed tomography scans by using rapid prototyping techniques, is a scaled replica of a human right nasal cavity. The resulting vector plots show that the flow is laminar and regions of highest velocity are in the nasal valve and in the inferior airway. The relatively low flow in the olfactory region appears to protect the olfactory bulb from particulate pollutants. Low flows were also observed in the nasal meatus, whose primary function has been the subject of debate. Comparison of sequentially recorded data suggests a steady flow. Heenan et al. (2003) measured the velocity field in the central sagittal plane of an idealized representation of the human oropharynx (HOP) during steady inspiration using endoscopic PIV. The PIV data indicated the complex nature of HOP flow, with three-dimensionality and several regions of separation and recirculation evident. The main objective of the present investigation was to evaluate fluid dynamic characteristics in the human pharynx. In doing so, in vitro PIV measurements were carried out at various section of the pharynx. This article reports the findings of experimental studies to characterize airflow within the human pharynx under a physiologic condition.

Due to the nature of the complex setup involved in the experimental study, the velocity profile and particle transport was often investigated separately and the interaction between fluid (airflow) and particles (aerosols) was rarely explored in experimental studies.

Schlesinger et al. (1977) developed a hollow silicone rubber cast of the larynx and tracheobronchial tree which extended to bronchi of approximately 0.2 cm diameter. The cast was exposed to radioactively tagged, ferric oxide aerosols, having mass median aerodynamic diameters ranging from 2.5 to 8.1 μm, at three constant inspiratory flow rates. Their study found that bifurcation deposition generally peaked in generation 3 and high flow rate led to higher deposition in all generations. Similar study was also conducted by Schlesinger et al. (1982), except cyclic flow was used. Deposition efficiencies at bifurcation and length sub regions of each generation were greater under cyclic flow and these differences were greater for the smaller sized aerosol. They studied the surface density distribution on the first bifurcation and showed that higher concentration appeared at the carina ridges and the inner wall of the bifurcation under both constant and cyclic flow conditions. Chan and Lippmann (1980) measured the particle deposition for the first six branching generations of replicate hollow casts of a human tracheobronchial tree with a mechanical larynx and drawn some basic agreements when they compared their results with data obtained from twenty-six non-smoker human volunteers in vivo, where a liner dependence of particle deposition efficiency on the Stokes number for aerosols with aerodynamic diameters >2 μm. Cheng et al. (1999) also provided similar results as they measured deposition efficiencies in a replicate cast of human oral-tracheobronchial airways made from an adult cadaver under different flow rates. They found that 90% of particle > 20 μm

would be trapped within oral cavity when flow rate reached 60 L/min. This is why particle larger than that size would not be studied in tracheobronchial airways in this research. Deposition efficiency is a unique function of the Stokes number, suggesting that impaction is the dominant deposition mechanism. Zhou and Cheng (2005) used the same method as Cheng et al. (1999) and indicated that the deposition efficiency with the larynx effect is generally larger than without it and hence the larynx affects the flow pattern of the tracheal region, causing more particles to be deposited. They also suggested that the turbulence induced by the laryngeal jet could likely persist in the first few generations of the tracheobronchial airways, resulting in higher deposition efficiencies. Kim and Fisher (1999) established a logistic function to describe the deposition efficiency that they measured on a symmetrical double bifurcation glass tube model with dimensions similar to Generation 3 to Generation 5 (G3-G5) in Weibel's symmetrical model. Their results showed that DE in each bifurcation increased with increasing Stokes number, ranging from ~ 1% at St = 0.02 to ~ 40% at St = 0.2. Their deposition pattern also showed highly localized deposition on and in the immediate vicinity of each bifurcation ridge at Stokes numbers as low as 0.02, regardless of branching patterns and flow distribution used.

The research above demonstrates that the Stokes number is one of the important factors in determining deposition efficiency, but the research also showed that experimental data from various studies have large variations but the same characteristic of trends for DE vs. Stokes number is still presented. Velocity profiles measured in different experiments can be comparable when correct Reynolds number, oscillatory frequency and geometrical details are met. These two issues will be good indicators in verifying the present numerical study.

2.2 Numerical studies of airflow and particle transport in human airways

With increasing computational resources and the widespread availability of commercial and self-developed Computational Fluid Dynamics (CFD) codes, the methodology is gaining in popularity as an attractive research tool to study the airflow pattern in the human respiratory system. Research works such as found in Elad et al. (1993), Yu et al. (1998) and many others have exploited the use of both commercial and self-developed codes towards the prediction of airflow in the EX airway. Despite the many encouraging results reported, some uncertainties still prevail concerning the use of current CFD models.

The first uncertainty of the CFD approach is the lack of anatomically accurate geometry. In most numerical studies of the EX flows (Luo et al., 2004, Stapleton et al., 2000, Zhang et al., 2004), surrogate or idealized geometries are usually employed instead of realistic constructions. However, the airflow is strongly dependent on the airway geometries and simplifications to the geometry may lead to the lost of physiology information. Therefore, the anatomically accurate airway geometry is rather important to obtain accurate flow behaviours information.

The second uncertainty is the ability of the CFD models to properly reproduce the physical phenomenon in the strongly three-dimensional flows within the complicated EX airway. Here, two specific physical phenomenons that contribute to the complexity are identified: (i) the presence of turbulent flows as well as laminar and transitional flow patterns and (ii) flow separation, recirculation, secondary flow and shear stress variations along the EX surface. It has been recognized that the flow pattern in the EX airway is the combination of laminar, transition and turbulent flows (Dekker,

1961). To account for the turbulent nature of the flow, turbulence models have to be employed to approximate the effects of turbulence.

Because of the application of approximate models, the selection of the appropriate choice of turbulence models for biomedical applications requires investigation. The standard k-ε model, which is based on a two-equation approach (k is the turbulent kinetic energy and ε is the dissipation of the turbulent kinetic energy) commonly used in many engineering applications, has demonstrated to perform rather poorly in predicting the EX flows (Stapleton et al., 2000). Zhang and Kleinstreuer (2003) evaluated other turbulence models that included four Eddy-Viscosity turbulence Models (EVMs) and reported that the Low Reynolds Number (LRN) k-ω model (Wilcox, 1998) gave the best performance in predicting of the flow within the EX surrounding space. Here, ω is defined as the inverse of the dissipation ε. However, these EVMs have been found to be insensitive to the orientation of the turbulence structure and its transporting and mixing mechanisms (Hanjalic, 1994), and their inability to account for the selective amplification or attenuation of different Reynolds stresses by curvature-related strain components. Furthermore, the EVMs under-predicted the pressure-driven secondary flows and produced a weak, highly diffused streamwise vorticity field in simulating the flow in a 90^{o} bend (Sotiropoulos and Ventikos, 1998). Thus, the suitability of EVMs for the EX airflow is doubtful due to the curvature streamline in the 90^{o} nasopharynx bend where secondary flow and strong anisotropy occur. Recently, Luo et al. (2004) employed Large Eddy Simulation (LES) to study the turbulent flow in a single asymmetric bifurcation model. However, uniform mesh requirement of LES lead to large number of grid cells in the vicinity of a solid boundary, longer time and large computational resources consumption.

Reynolds Stress Model (RSM) that solves the transport equations for each individual Reynolds stresses accounts automatically the effects of streamline curvature and stress anisotropy. It usually performs better than EVMs in applications where the anisotropy of the Reynolds stresses dominates the flow (Hanjalic, 1994). Thus, the RSM may be more suitable for the EX airflow than the EVMs. Although RSM does not represent the unsteady nature of turbulence as does dynamic model LES, it is effective in computing the time averaged quantities and is orders of magnitude cheaper than LES. To the best of the authors' knowledge, no investigation has been performed on the EX airflow simulation using the RSM.

In numerical studies, a smooth-walled (and hence simplified) airway model was mostly employed with only variation in geometry and method of dichotomy. Regular dichotomy (symmetry) airway models have been extensively studied by Comer et al. (2000a & b) and Zhang et al. (2002a & b). Irregular dichotomous airway models have also been investigated by Zhang et al. (1997) and Balásházy & Hofmann (1993). All these studies showed that the regional deposition efficiency (DE) can be expressed as a logistic function in terms of inlet Stokes (St) number for the studied bifurcation geometries.

In terms of validating CFD results, Zhang and Kleinstreuer (2002) and Comer et al. (2000 a & b) have extensively compared their numerical results with experimental results in regard to the velocity profile from Zhao & Lieber (1994) and the deposition efficiency from Kim & Fisher (1999). They demonstrated consistent results in a steady flow condition within Stokes number ranging from 0.01-0.12. They also explained how particles' trajectory was affected by airflow vortexes before and after bifurcation using G3-G5 model. Balásházy and Hofmann (1993) and Zhang et al. (1997) compared the

DE with different bifurcation angles using G3-G6 symmetric model. Their results indicated that DE increased with larger bifurcation angle. Furthermore, Zhang et al. (1997) investigated DE in different Reynolds (Re) numbers and showed that DE increased with increasing Reynolds number, but became almost independent of Re when $St > 0.1$. The above studies used idealised model which the model geometry was hardly comparable to real human airway structure. From a realistic human airway geometry perspective, Vial et al. (2005) reconstructed the tracheobronchial airway from the CT scan data and simulated airflow. Their results were examined in terms of the lobar flow distributions with Katz and Martonen (1996) and Corieri (1994)'s results and geometrical details with Weibel (1983)'s dichotomous model. Ertbruggen et al. (2005) although used smooth-walled models, the model was based on the morphometrical date of Horsfield et al. (1971), which Horsfield and his colleagues measured all structure down to generation 6 of a resin cast of a normal human bronchial tree. They compared their numerical results from experimental results with Kim et al. (1996) in terms of regional deposition efficiency and velocity profiles with Calay et al. (2002)'s measurement. Since experiments they compared with had either respiratory or geometrical differences, some rounding errors were thus expected, but basic characteristic of flow and particle behaviours were still reflected in their results.

Zhang & Finlay (2005) proved that trachea with cartilaginous rings would enhance particle deposition in the trachea for all inhalation rates and particle sizes when compared with smooth-walled trachea. The influence of larynx on the airflow and particle deposition in the trachea and its lower airways has been included in many experimental and numerical simulations through complete upper airways analysis (from oral cavity to lower generations). Zhang et al. (2005) also showed that the larynx effect

causes turbulent fluctuations at medium and high inspiratory flow rates (30 and 60 L/min) due to the enhancement of flow instabilities immediately upstream of the flow dividers. Moreover, the effects of turbulent fluctuations on micro-particle deposition are relatively important in the human upper airways. These phenomena therefore would be expected in the present study.

Asgharian and Price (2006) studied the influence of airflow distribution among bronchi on particle deposition and found that airflow rate entering each major bronchus was similar for uniform and non-uniform lung expansions and concluded that the assumption of uniform air expansion and contraction was sufficient for the predictions of regional and total deposition of particles in the lung. However, they also pointed out that accurate predictions of local and site-specific deposition of particles required more detailed models of lung ventilation that account for non-uniform lobar expansion due to the pressure variation in the pleural cavity. In this research, the assumption of uniform air expansion and contraction was taken into account, but the later issue was not considered in this study due to it complex modeling requirement.

2.3 Summary

In this study, an anatomically accurate geometry of human upper airway models, which have been generated by Computed Tomography (CT) scanner, is investigated by using a second order RSM turbulence model. To provide credibility of the numerical predictions, experimental models based on the geometry of numerical models, were built and measured by using the Particle Image Velocimetry (PIV) technique. The comparison between the numerical results and experimental data has been made, and a reasonable agreement is achieved. The combination of numerical and experimental

results will lead to a better understanding of the airflow behaviors as well as improvements to the numerical model. Descriptions and possible conclusions of the particular flow characteristics observed in these areas of the EX airway are discussed.

In addition, given a brief overview of the research related to this study, it can be seen that no research has been carried out to consider the effect of the nasal hair on particle deposition. It was assumed by Hahn et al. (1993) that the inclusions would not contribute to the difference in the particle deposition efficiency. But in nature, the main function of the nasal hair is to act as a filter for very small and very large particles (Mygind 1998). However the geometrical construction of nasal hair throughout the vestibule would be hypothetical as the distribution of nasal hairs varies from person to person. Another drawback is that it is time consuming and hence not feasible to simulate. Nevertheless, there is an alternate, simple, way of simulating the nasal hair, namely considering them a filtration medium.

Chapter 3: Model Construction

3.1 Introduction

Medical images can be obtained from various sources, yet all provide essentially similar information: a 3D matrix (or series of 2D matrices) of volume elements (voxels), in which tissues and structures are distinguished from one another by differences in brightness or greyscale. Visualization and reconstruction of morphological structures contained within these images is an area of active research. Although the extraction of airway structures and their reconstruction were not originally intended to be the focus of this research, they became by far the most time consuming aspect of the work.

In this chapter I summarized the basic segmentation and reconstruction techniques. Section 3.2 will review issues specifically related to obtaining 3D CT and MR image, while Section 3.3 will present a brief review of reconstruction methodologies. Section 3.4 describes the reconstruction methodology for this work, including image acquisition, image processing, segmentation and surface reconstruction.

3.2 Review of Image Modalities

Magnetic resonance images are 3D matrices where the greyscale value assigned to each voxel is determined by the magnetic behaviour of the protons contained within the voxel. Since different tissues contain different amounts of hydrogen, they can be distinguished in an image as regions of different greyscales. Various imaging sequences can be used to enhance the contrast of particular entities within the field of view. For example, the time-of-flight (TOF) sequence is used in magnetic resonance angiography to highlight motion perpendicular to the plane of the imaging slice. TOF images provide particularly good information about vascular structures, since the flow of air

normal to the plane of the imaging slice provides good contrast from the surrounding tissue structures. The contrast is provided by saturating the imaging plane with radio-frequency energy. Air that moves into the plane provides fresh spins and appears bright in the image, in contrast to the saturated tissues surrounding the airway.

Similar to MR, CT images are also matrices of voxel greyscale values determined by the CT number of the voxel tissue. Again, since different tissues have different attenuation characteristics, the resulting image distinguishes different tissues by greyscale. Although both MR and CT images provide 3D volumetric data sets, in this study, they are viewed as a series of stacked 2D pixels which have an associated depth, or slice thickness.

3.3 Review of Reconstruction methodologies

The construction of numerical models from medical images can be divided into four stages: image acquisition, data conversion, segmentation and surface reconstruction. Segmentation of a morphological structure is frequently based on various thresholding techniques, in which a voxel is marked if its properties are above a given threshold. The simplest examples of thresholding are greyscale thresholds, where the voxel property that is examined is its neighbours determines which voxels are marked. These simple methods are highly effective for clean images with high contrast.

There are two approaches of reconstructing the structures from segmented images: volume rendering and surface rendering. As the names suggested, volume rendering methods use the entire data set from a 3D medical image, whereas surface rendering techniques deal with a much smaller data set containing only information about the surface of a morphological structure.

Volume rendering combines segmentation of a morphological structure with reconstruction or visualization of the surface. This method relies on ray casting, where a ray from the eye is passed through each voxel in the image, and various thresholding techniques are used to determine whether the voxel is on the edge, or surface, of the morphological structure. Volume rendering provides excellent 3D visualization, and can even provide a very intuitive surface editing interface, but it is computationally expensive because it requires manipulation of the full 3D image set. However, fundamentally these methods are essentially only a display tool. In order to interface the extracted surface with any modeling or meshing algorithms, the volume rendered object must be successively sliced to obtain contours, and the contours must then be manipulated to mathematically define the surface.

Once the 2D contour information is extracted, the surface must be described. Direct tiling is frequently used to render the surface from the contour data. This method creates a surface triangularization directly from the contour points using nearest neighbor matching between points on the n^{th} contour with points on the $n + 1^{st}$ contour level. Direct tillers often encounter difficulties with bifurcating surfaces, such as those which are reconstructed in this research, although recently released tillers are more reliable.

Anther recently developed method is the volumetric marching cubes algorithm, which can automatically transform a 3D binary edge-detected image into a tetrahedral volume-filling mesh. Marching cubes produce very satisfactory results, but require clean, high resolution images with complete boundaries.

Smoother surface descriptions can also be obtained by using the 2D contours to define surface splines. Local surface spline patches have been stitched together to

describe morphological structures. Alternatively, entire surfaces may be lofted from the series of 2D contours. This lofting method to obtain smoothly rendered surfaces was chosen as the basis for the reconstruction methodology which will be presented in next section.

3.4 Reconstruction method in this work

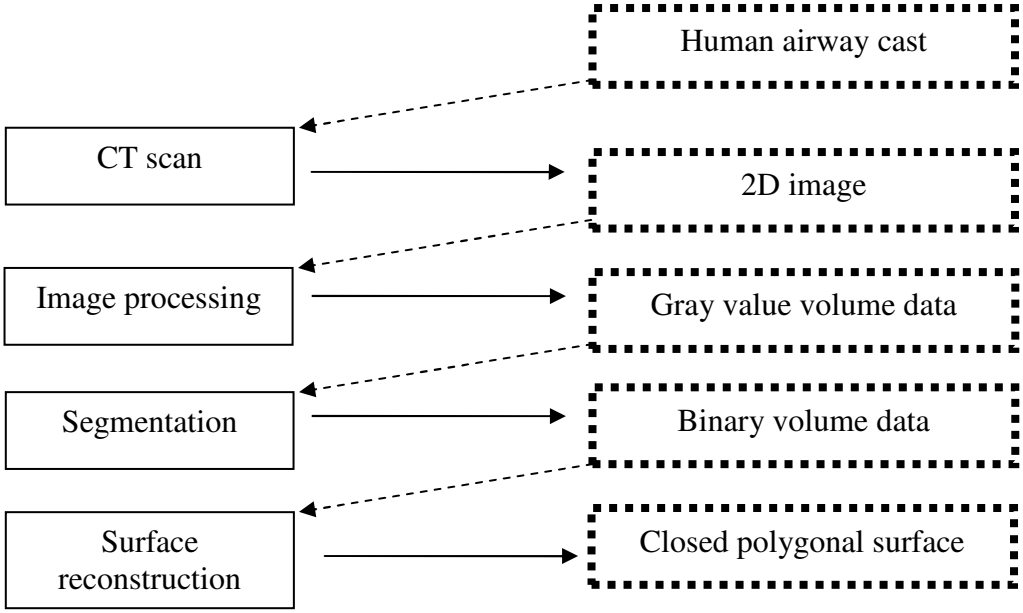

Fig. 3.1 Flow chart of the reconstruction methodology used in this research

In order to simulate the fluid dynamics for the airway aerodynamics from geometric data obtained from CT images, the following steps have been performed, as shown in Fig. 3.1.

1. CT images acquisition;
2. Image processing and editing to improve the quality of the image volume;

3. Segmentation;
4. Surface reconstruction.

3.4.1 Acquisition

Computed tomography (CT), originally known as computed axial tomography (CAT or CT scan) and body section rentenography, is a medical imaging method employing tomography where digital geometry processing is used to generate a three-dimensional image of the internals of an object from a large series of two-dimensional X-ray images taken around a single axis of rotation. The word "*tomography*" is derived from the Greek *tomos* (slice) and *graphein* (to write). CT produces a volume of data which can be manipulated, through a process known as *windowing*, in order to demonstrate various structures based on their ability to block the X-ray beam. Although historically (see below) the images generated were in the axial or transverse plane (orthogonal to the long axis of the body), modern scanners allow this volume of data to be reformatted in various planes or even as volumetric (3D) representations of structures.

In this study, airway geometry was obtained through a CT scan of the airways of a healthy 25 year old, non-smoking Asian male (170 cm height, 75 kg mass) for the nasal cavity and first three generations of airway (from trachea – G0 to lobar bronchi – G2, hence Generation 0 to Generation 2). CT scan was performed using a CTI Whole Body Scanner (General Electric). The single-matrix scanner was used in helical mode with 1-mm collimation, a 40-cm field of view (FOV), 120 kV peak and 200 mA. At baseline, 2 cm axial length of lung caudad to the inferior pulmonary ligament was scanned during a single breath-hold, which yielded 112 contiguous images (slices) of 1-mm thickness with voxel size 0.25×0.25×1 mm. Then, the CT data was fed into an

airway tree segmentation algorithm that can automatically identify the airway lumen in the CT image. Figure 3.2 shows the CT images of nasal cavity and airway bifurcations respectively.

(a)

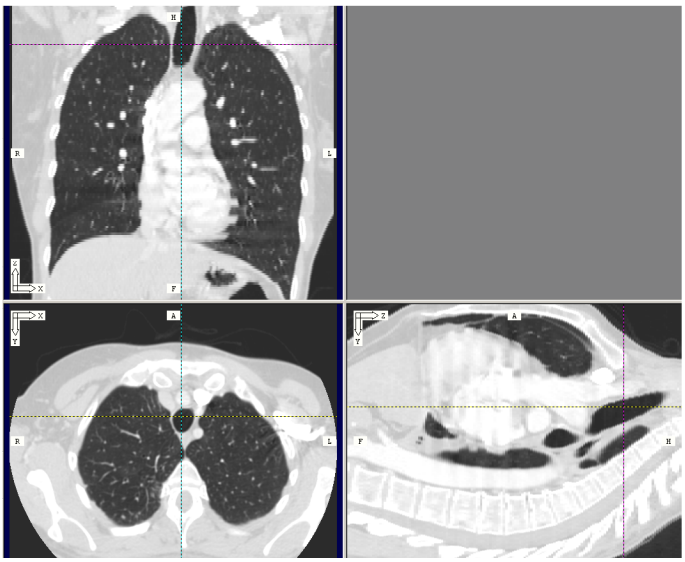

(b)

Fig. 3.2 (a) CT image of nasal cavity, (b) CT images of airway bifurcations

3.4.2 Data conversion and image processing

The original set of CT images is converted into a file format compatible with the package Mimics(Reference), a CT/MRI 3D imaging software to enable dentists, doctors and researchers to produce high quality polygonal models from CT/MRI slice. The conversion program also performs an image enhancement, by rescaling the grey-level histogram to 1-200 and remapping the image volume to an 8-bit/pixel depth file.

Image processing includes the following steps:

- Sub-image creation, which extracts a new volume from the original image. The sub-image extraction has a twofold purpose: (a) to reduce both the amount of calculations needed in the further processing steps and computational time and memory resources; and (b) to remove the noisy regions out the airway;
- 3D convolution with a Gaussian kernel, which reduces the background noise present in the images. Because of its isotropic shape, the Gaussian filter has optimal properties such as smoothing mask, removing small-scale texture and noise, which could alter the regional segmentation, without distorting lower spatial frequencies. Filtering has been applied in three dimensions in order to obtain a smoothed CT image volume also along the axial direction. Such a procedure attenuates the spatial discontinuities among the slices introduced during acquisition, as an effect of the slice thickness.

3.4.3 Regional segmentation

A 2D segmentation is used to detect and extract, slice by slice, the walls of the airway. For the segmentation process, a region growing algorithm, based on the Mumford and Shah method implemented Mimics is used.

The regional segmentation has been included because it allows the tracking only of the domains of interest, even in the presence of noise. A first regional segmentation with a greater number of partitioning regions than necessary is performed on each single slice. This allows the algorithm to detect the walls even in severely disturbed images.

A threshold binarisation process is then applied in order to remove sub-regions unrelated to the airway, which typically present a lower intensity value with respect to the signal. In this wok, the threshold has been empirically chosen and represents 45% of the maximum grey-level value of the study.

The airway contours may exhibit some irregularities due to the image discretisation, such as harsh corners, which may cause severe distortions in the flow field values, when the model is used in fluid-dynamic simulation. To avoid this effect a moving average between the spatial co-ordinates confining the airway lumen is performed. The number of average operations (n) is imposed by the user, so that the function executes n-times the computations. As an optimal trade-off between removing contour irregularities and preserving a suitable spatial resolution, moving average step was applied twice.

The algorithm provided the outlines of every slice (in X-Y plane) respected to its vertical position (Z location of the slice) in a 3-D space in which was stored as IGES file (Initial Graphics Exchange Specification).

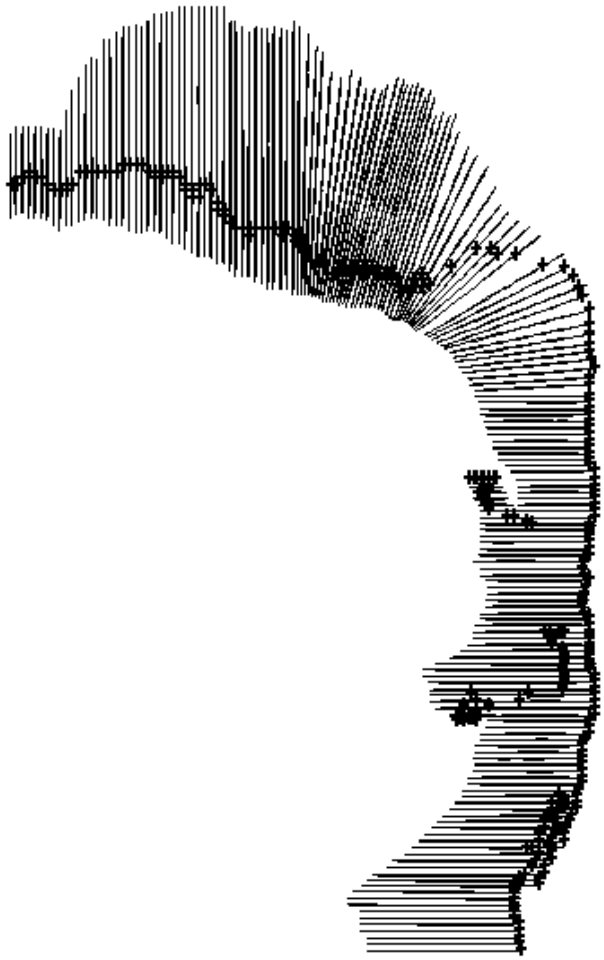

(a)

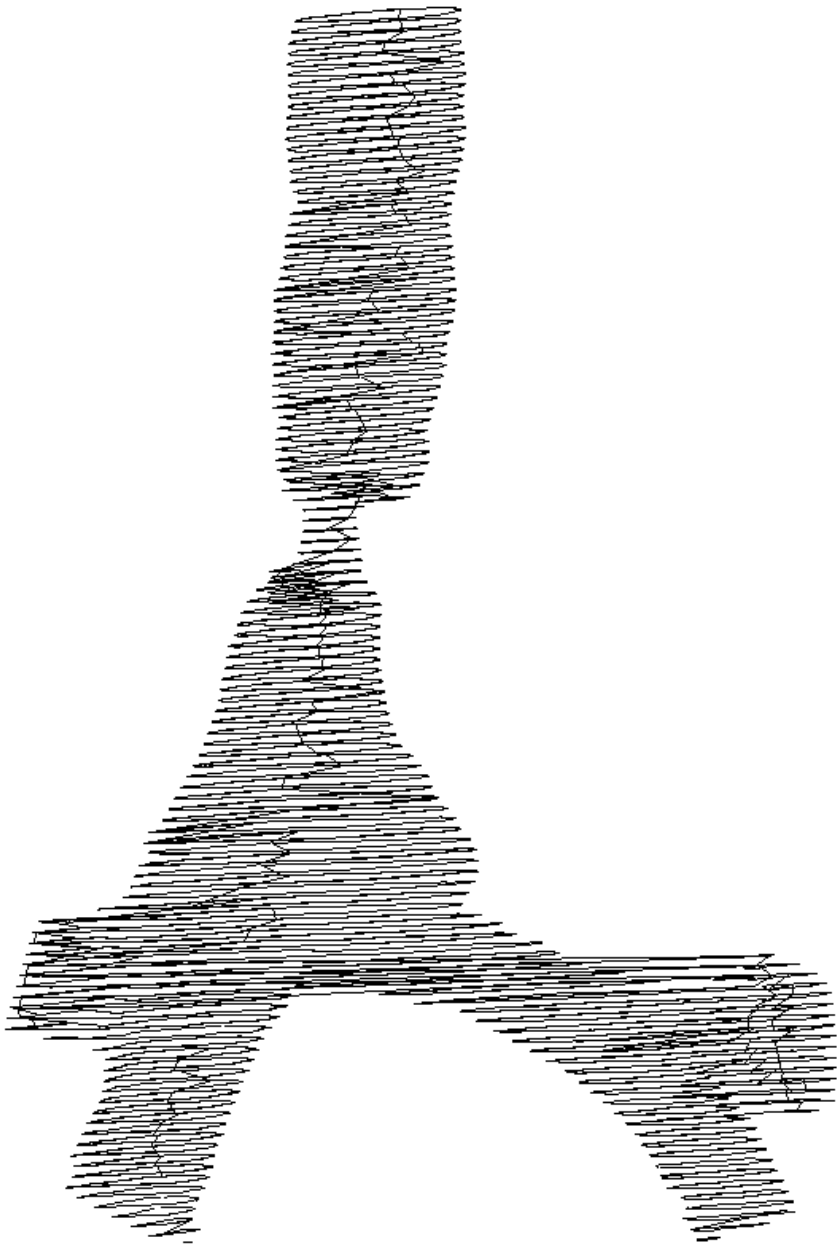

(b)

Fig. 3.3 Slice images obtained from CT scan: (a) Human nasal cavity, (b) Realistic double bifurcation airway

3.4.4 Surface generation

Generation of a surface or solid model from the 2D contour data began with the translation of the segmented, modified and smoothed contour points into a data series that was read into a package used in this study: Gambit, a pre-processor of Fluent

package. Based on the IGES file, GAMBIT was used to create face, volume, and modification using the outlines given by the algorithm. The contours were lofted to define surface splines which enclosed the airway volume.

The main difficulty encountered with surface generation was accommodating bifurcating geometries. Ultimately, it was found that a branching geometry could be most reliably reconstructed in three parts: the two child branches and the parent branch were constructed separately and then joined afterwards. One difficulty posed by this method is that in order to obtain a smooth transition from parent to child branches, the surface tangency must be matched, but only for the outer sections of the end contours. In practice, this limited tangency control was beyond the capabilities of the CAD package used. As a result, the reconstructed models often demonstrated a sharp, unphysiological seam where the parent and child branches were joined. The contour augmenting significantly reduced the appearance of these seams by more closely matching the original data and forcing a natural change in surface tangency from the parent to the child branch. In some cases however, additional smoothing had to be employed to remove these seams. As a result, some modifications have also been done, such as correcting overlapping surfaces, smoothing some of the unreasonable sharp curves in the airway. As shown in Fig. 3.4, a vestibule region was attached with the nasal cavity (a), and at the top of the trachea was also modified and an inlet was attached (b). Extended tubes were attached at the lowest generations for numerical purpose.

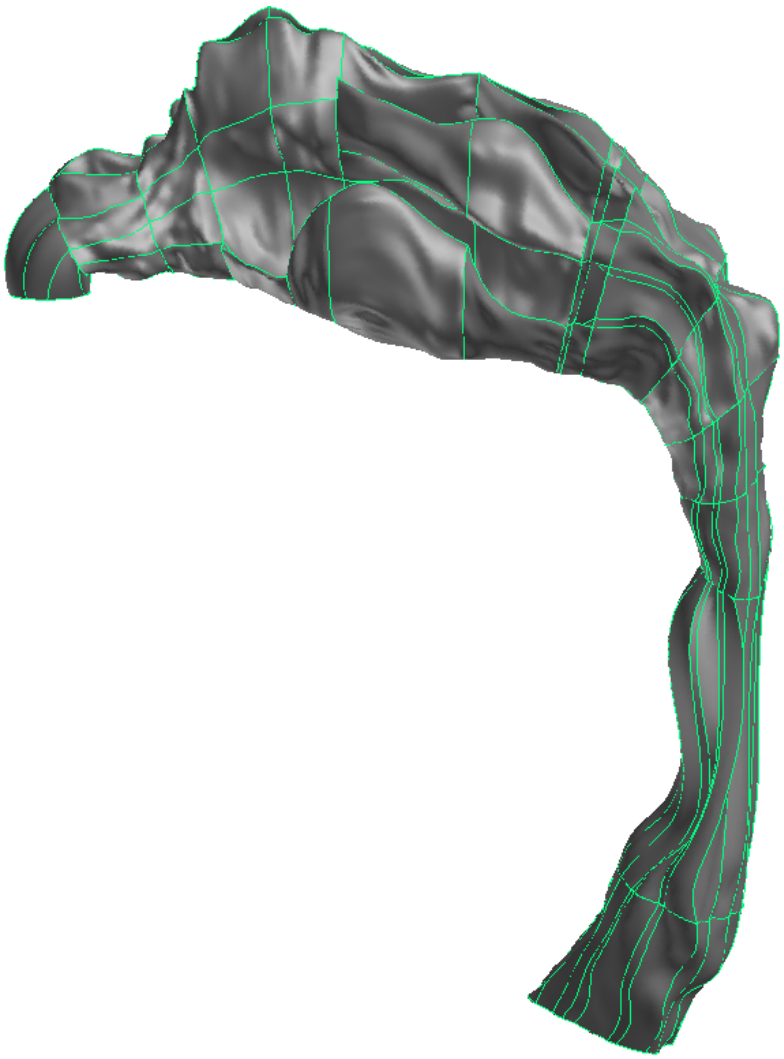

(a)

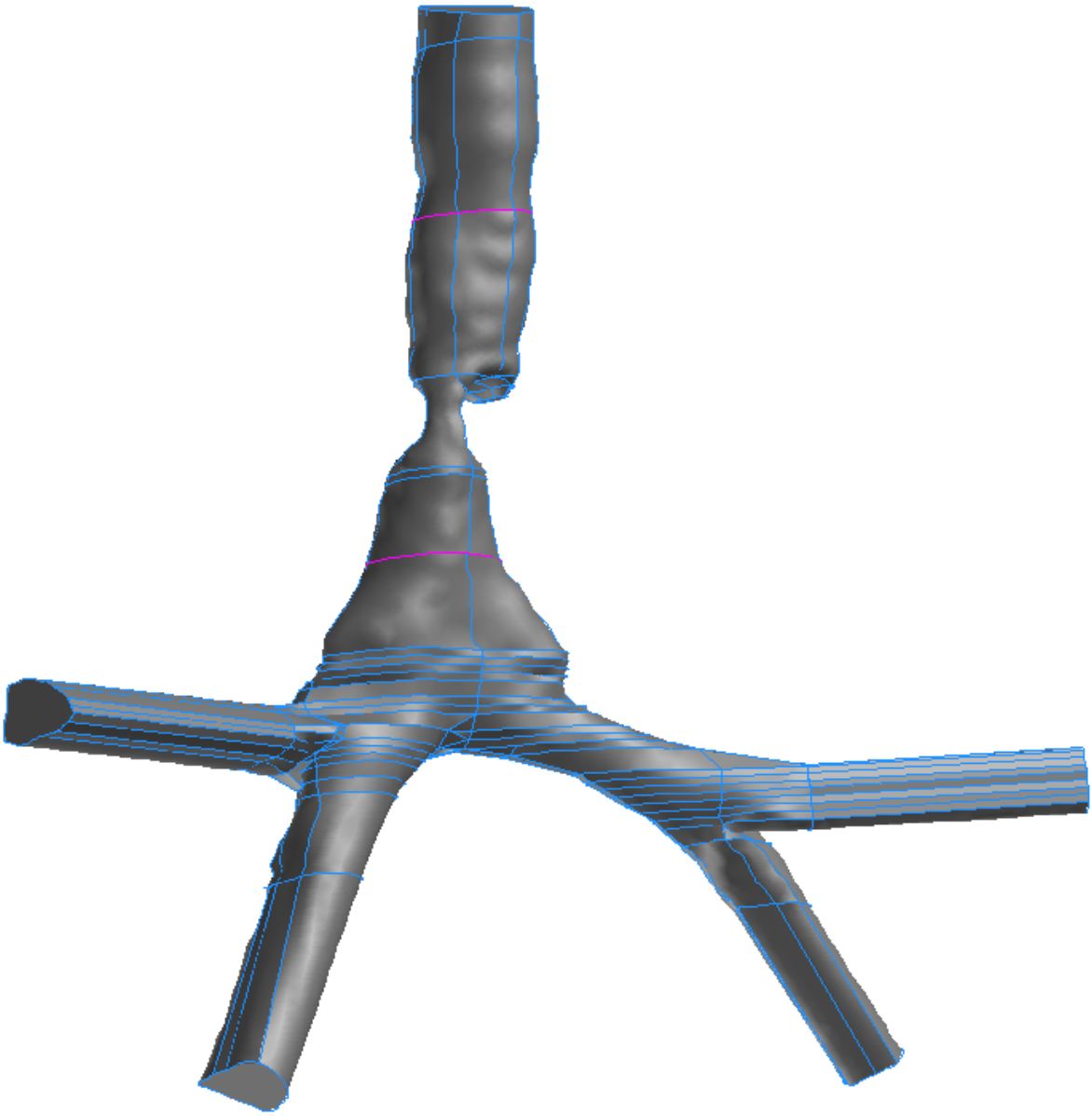

(b)

Fig. 3.4 The reconstructed models from slice images: (a) Human nasal cavity, (b) Realistic double bifurcation airway

In this chapter, we present a method for segmenting and reconstructing human airway in 3D from the data set of CT images. The main difficulty encountered with surface generation was accommodating bifurcating geometries. Ultimately, it was found that a branching geometry could be most reliably reconstructed in three parts: the two child branches and the parent branch were constructed separately and then joined afterwards. It is very important for this study as we pursue the realistic geometry. The 3D geometric model can provide a comprehensive view of the airway, thus helping to achieve more accurate CFD simulations and experimental studies of air/particle behaviours.

Chapter 4: Numerical Simulation

4.1 Mesh generation and Grid sensitivity studies

In general, in CFD simulations of human airway aerodynamics, high-velocity gradients have to be resolved near the airway wall due to the presence of viscous boundary layers in which velocity varies from zero (on the wall) to high values toward vessel centre. The use of boundary layers of thin elements near the wall allows to increase accuracy and to obtain better convergence of the CFD solver. Since we are interested in quantities such as wall-shear stress, which are computed by spatial differentiation of the near-wall velocity field, the generation of boundary layers of proper thickness constitutes an important issue. At the beginning, we proposed meshing of airway with hexahedral elements, which resulted in the generation of boundary elements well layered along surface. Unfortunately, for geometries involving more than one bifurcation, the task of generating meshes for models making use of hexahedral elements becomes complex. Moreover, hexahedral elements make it more difficult to locally refine mesh regions on the basis of geometric features or CFD solution residuals. For these reasons, we here preferred to make use of 10-noded quadratic tetrahedral elements (inherently more stable than 4-noded linear tetrahedral elements) for volume meshing. In order to achieve easy meshing and element-size specification as required to near-wall accuracy, we decided to adopt 18-noded quadratic wedges for boundary layer generation.

The technique described for geometric analysis allowed us to create boundary layers with radius-adaptive thickness. It is in fact possible to demonstrate that the direction defined by a surface mesh vertex and its pole approximates surface normal. In

particular, by definition, direction of vector maximizes the distance from neighbours. Therefore, boundary layer thickness could be specified as a fraction of vessel size. This way boundary layer thickness was higher in larger vessel branches and lower in smaller ones. In order to obtain surface elements with adequate aspect ratio and grading for subsequent warping, surface mesh quality has to be improved, either using decimation or edge swapping techniques or surface remeshing. Geometric analysis was then performed and geodesic distance to central paths mapped onto the surface. Before warping the surface mesh, in order to obtain 18-noded quadratic wedges, we applied a modified Butterfly subdivision scheme to surface triangles to generate 6-noded quadratic triangles. As formerly mentioned, inner volume was finally meshed with 10-noded tetrahedral elements by means of an advancing front approach. It is important to point out that the adaptive boundary layer generation procedure is independent from the particular surface remeshing or tetrahedral volume meshing techniques employed.

Grid sensitivity study was carried out to ensure that the results are insensitive to the size of grid. Four different grid sizes with 31 104, 79 820, 159 872 and 320 980 nodes were studied at the maximum inspiratory peak flow rate under resting condition. At this stage, only the peak velocity during inspiration was used to ensure that the results at the highest Reynolds number were independent of the grid size.

A uniformly distributed velocity profile was imposed at the inlet of the parent tube with an average value of 1562.5 mm s−1 corresponding to Reynolds number of 1570 based on parent airway diameter (16 mm). The axial velocity profiles were taken from at different cross sections in the parent airway and daughter airways. There are 15 cross-sectional stations in the parent and daughter airways. Stations P1, P2, P3 and P4 are located in parent airway. P1 and P2 are at 1 local diameter and 3 local diameters

from the inflow/outflow boundary in parent airway. P3 and P4 are located at 12 local diameters and 1 local diameter from the carina in parent airway. L1, L2, L3, L4, L5, L6 and L7 are located in left daughter airway at every 12 local diameter from the carinal ridge and L8 is located at 12 diameter from the inflow/outflow boundary. R1 and R2 are located at every 12 diameter from the carinal ridge in right daughter airway and R3 at 12 diameter from the inflow/outflow boundary. The axial velocities were obtained from two planes to the model. Plane R–L (right–left) is the same plane as the bifurcation from right to left hand sides of the model. Anterior to posterior (A–P) is the plane normal to the bifurcation plane from anterior to posterior of the model.

The results at P1 and L3 of four different grid sizes were compared. At station P1, one diameter from the inflow boundary in the parent tube, the velocity profiles both in the bifurcation and normal plane to the bifurcation for all grid sizes yielded the similar results at the centre of the pipe. But in the region near the walls the velocity profiles in each grid model were noticeably different. This region being within the boundary layer thickness is most influenced by the grid size.

Comparing between four grid sizes, the velocity profiles near the wall for the grids 3 and 4 with 159 872 and 320 980 nodes, respectively were identical. Velocity profiles in the boundary layer region obtained from these two cases were smoother than those found with coarser grids 1 and 2 with 31 104 and 79 920 nodes, respectively. The boundary layer regions observed from the grid sizes of 320 980 and 159 872 were well defined and distinct than those observed from the grids 1 and 2. This indicates that the higher number of grid cells within the boundary layer region can capture the flow field in more detail than those for the coarser grid size cases. The difference observed in velocity profiles near the wall between the coarse grid case and the fine grid become

more noticeable as the flow develops downstream through station P2 and P3. However, the velocity profiles for the grids 3 and 4 were still similar when the flow developed downstream. It is suggested that the flow-field results obtained from the grid size of 320 980 and 159 872 node points were grid independent. A similar difference is observed in the velocity profiles in the two daughter airways near the walls between coarse grid and fine grid. The velocity profiles at the core of the flow were also different in both bifurcation plane and normal plane to the bifurcation. Particularly, at the inner walls of the bifurcation in both daughter airways, the axial velocity profiles in bifurcation were significantly different. The skewed velocity profiles were found towards the inner wall of the bifurcation (outer wall of the bend) for all grid sizes investigated. The skewed or distorted axial velocity profiles in both daughter airways were due to the secondary motions. The axial profiles were found to be less distorted for coarser grid (models 1 and 2) than for the finer grid (models 3 and 4). This can be due to fact that the higher grid resolution is able to resolve more detail of the secondary vortices than the coarser grid resolution or to capture the accurate physical feature of the flow field. Thus, the axial velocity profiles observed in the finer grid were more distorted than the coarse grid cases.

Due to high computing power and computing time requirements, the optimum grid size is always sought. For the present study results from the grid 3 with 159 872 nodes were assumed to be grid independent and was chosen for further simulations. Although the velocity profiles obtained from all grid sizes seem to be different yet the difference in the results obtained from the grids 3 and 4 was only up to 1–2%. It was clearly seen that the change from grid sizes of 159 872–320 980 nodes yielded similar

results that can capture the flow field in more detail when compared with the results from coarser grids.

4.2 Gas phase modeling

Several turbulence modeling techniques are used to handle the gas phase turbulence in this thesis: k-ε models that are in the framework of Reynolds averaged Navier-Stokes (RANS) model and a RNG-based LES model.

4.2.1 General conservation equations for gas phase

CFD is fundamentally based on the governing equations of fluid dynamics. They represent mathematical statements of the conservation laws of physics. These laws have been derived from the fact that certain measures must be conserved in a particular volume, which is called control volume. The gas phase conservation equations of a scalar Φ can be cast in a general form:

$$\frac{\partial(\rho_g \phi)}{\partial t} + \frac{\partial(\rho_g u_i^g)}{\partial x_j} = \frac{\partial}{\partial x_j}\left(\Gamma \frac{\partial \phi}{\partial x_j}\right) + q_\phi \qquad (4.1)$$

(1) (2) (3) (4)

where t is time, ρ_g denotes the gas density, u_i^g represents gas velocity, Γ is the diffusivity of the scalar, q_ϕ is a general source term. The term (1) in Equation (3.1) is the local acceleration term and term (2) is the advection term. The term (3) on the right hand side is the diffusion term and term (4) is the source term.

This equation is usually used as the starting point for computational procedures in either the finite difference or finite volume methods. Algebraic expressions of this equation for the various transport properties are formulated and hereafter solved. By

setting the transport property ϕ equal to 1, u_g, T, and selecting appropriate values for the diffusion coefficient Γ and source terms q_ϕ, one ban obtain the special forms presented in Table 4.1 for each of the partial differential equations for the conservation of mass, momentum and energy.

Table 4.1 The Governing Equations for Gas phase in Cartesian Coordinates

---

Conservation of mass ($\phi = 1$)

$$\frac{\partial \rho_g}{\partial t} + \frac{\partial \left(\rho_g u_j^g \right)}{x_j} = 0 \tag{4.2}$$

For incompressible flow

$$\frac{\partial \left(\rho_g u_j^g \right)}{x_j} = 0$$

Conservation of Momentum ($\phi = u_i^g$)

$$\frac{\partial \left(\rho_g u_i^g \right)}{\partial t} + \frac{\partial \left(\rho_g u_j^g u_i^g \right)}{\partial x_j} = \frac{\partial}{\partial x_j} \left(\mu_g \frac{\partial u_i^g}{\partial x_j} \right) - \frac{\partial p_g}{\partial x_i} \tag{4.3}$$

Energy Equation ($\phi = T$)

$$\frac{\partial \left(\rho_g T \right)}{\partial t} + \frac{\partial \left(\rho_g u_j^g T \right)}{\partial x_j} = \frac{\partial}{\partial x_j} \left(\frac{\mu_g}{\mathrm{Pr}} \frac{\partial T}{\partial x_j} \right) \tag{4.4}$$

4.2.2 Turbulence models

Many engineering applications require computational procedure that can supply adequate information about the time-averaged properties of the flow (such as mean velocities, mean pressures, mean stresses etc.), but which avoid the need to predict all the effects associated with each and every eddy in the flow. Therefore, by adopting a suitable time-averaging operation on the momentum equations, one is able to discard all details concerning the state of the flow contained in the instantaneous fluctuations. Reynolds first introduced the notation of splitting the instantaneous flow variables into their mean and fluctuating components:

$$\phi(x_i,t) = \bar{\phi}(x_i) + \phi'(x_i,t) \tag{4.5}$$

Note that the overbar in Equation (4.5) denotes the time-averaged qualities. For an incompressible fluid, this process that is performed on the continuity Equation (4.2) and the conservation form of momentum Equations (4.3) produces the time-averaged governing equations or more popularly known as the Reynolds-Averaged Navier-Stokes (RANS) equations:

$$\frac{\partial\left(\rho_g \bar{u}_j^g\right)}{x_j} = 0 \tag{4.6}$$

$$\frac{\partial\left(\rho_g \bar{u}_i^g\right)}{\partial t} + \frac{\partial\left(\rho_g \bar{u}_j^g \bar{u}_i^g\right)}{\partial x_j} = \frac{\partial}{\partial x_j}\left(\mu_g \frac{\partial \bar{u}_i^g}{\partial x_j}\right) - \frac{\partial \bar{p}_g}{\partial x_i} - \frac{\partial\left(\rho_g \overline{u_i' u_j'}\right)}{x_j} + \frac{\partial \bar{\tau}_{ij}}{\partial x_j} \tag{4.7}$$

where $\bar{u}_i^g$ and $u'_{i,g}$ are gas phase mean velocity and gas phase fluctuating velocity, respectively. The $\bar{\tau}_{ij}$ are the mean viscous stress tensor components:

$$\bar{\tau}_{ij} = \mu_g \left(\frac{\partial \bar{u}_i^g}{\partial x_j} + \frac{\partial \bar{u}_j^g}{\partial x_i} \right) \tag{4.8}$$

The time-averaged equations can be solved if the unknown Reynolds stresses, $\rho_g \overline{u_i' u_j'}$ in Equation (4.7) can be related to the mean flow quantities. It was proposed by Boussinesq (1868) that the Reynolds stresses could be linked to the mean rates of deformation:

$$\rho_g \overline{u_i' u_j'} = \mu_t \left(\frac{\partial \bar{u}_i^g}{\partial x_j} + \frac{\partial \bar{u}_j^g}{\partial x_i} \right) - \frac{2}{3} \rho_g \sigma_{ij} k_g \tag{4.9}$$

where μ_t is the eddy viscosity or turbulent viscosity.

Standard k-ε model

Since the complexity of turbulence in most engineering flow problems precludes the use of any simple formulae, it is possible to develop similar transport equations to accommodate the turbulent quantity k_g and other turbulent quantities such as the rate of dissipation of turbulent energy ε_g. Here, k_g be defined and expressed in Cartesian tensor notation as

$$k_h = \frac{1}{2} \overline{u'_i \, u'_i} \tag{4.10}$$

and ε_g

$$\varepsilon_g = \frac{\mu_t}{\rho_g} \overline{\left(\frac{\partial u'_i}{\partial x_j} \right) \left(\frac{\partial u'_i}{\partial x_j} \right)} \tag{4.11}$$

From the local values of k_g and ε_g, a local turbulent viscosity μ_t can be evaluated as:

$$\mu_t = \frac{C_\mu \rho_g k_g^2}{\varepsilon_g} \tag{4.12}$$

By substituting the Reynolds stress expressions in Equation (4.9) into the governing Equation (4.6) and (4.7), and removing the overbar that is indicating the time-averaged quantities, one obtains the following equations:

$$\frac{\partial(\rho_g u_j^g)}{x_j} = 0 \tag{4.13}$$

$$\frac{\partial(\rho_g u_i^g)}{\partial t} + \frac{\partial}{\partial x_j}\left(\rho_g u_i^g u_j^g - (\mu_t + \mu_g)\left(\frac{\partial u_i^g}{\partial x_j} + \frac{\partial u_j^g}{\partial x_i}\right)\right) = -\frac{\partial p_g}{\partial x_i} \tag{4.14}$$

The additional differential transport equations that is required for the Standard k-ε model, which for the case of a constant fluid property and expressed in non-conservation form are:

$$\frac{\partial(\rho_g k_g)}{\partial t} + \frac{\partial(\rho_g u_j^g k_g)}{\partial x_j} = \frac{\partial}{\partial x_j}\left((\mu_g + \frac{\mu_t}{\sigma_k})\frac{\partial k_g}{\partial x_j}\right) - \rho\overline{u_i' u_j'}\frac{\partial u_i^g}{\partial x_j} - \rho_g \varepsilon_g \tag{4.15}$$

here, the rate of production of turbulent kinetic energy $P_k = -\rho\overline{u_i' u_j'}\frac{\partial \overline{u}_i}{\partial x_j}$ can be modelled by:

$$-\rho\overline{u_i' u_j'}\frac{\partial u_i^g}{\partial x_j} \approx \mu_t\left(\frac{\partial u_i^g}{\partial x_j} + \frac{\partial u_j^g}{\partial x_i}\right)\frac{\partial u_i^g}{\partial x_j} \tag{4.16}$$

and

$$\frac{\partial(\rho_g \varepsilon_g)}{\partial t}+\frac{\partial(\rho_g u_j^g \varepsilon_g)}{\partial x_j}=\frac{\partial}{\partial x_j}\left((\mu_g+\frac{\mu_t}{\sigma_\varepsilon})\frac{\partial \varepsilon_g}{\partial x_j}\right)-C_{1\varepsilon}\frac{\varepsilon_g}{k_g}P_k-\rho_g C_{2\varepsilon}\frac{\varepsilon_g^2}{k_g} \tag{4.17}$$

The equations contain five adjustable constants C_μ, σ_k, σ_ε, $C_{1\varepsilon}$ and $C_{2\varepsilon}$. These constants have been arrived at by comprehensive data fitting for a wide range of turbulent flows (Launder and Spalding, 1974):

$$C_\mu = 0.09, \qquad \sigma_k = 1.0, \qquad \sigma_\varepsilon = 1.3, \qquad C_{1\varepsilon} = 1.44, \qquad C_{2\varepsilon} = 1.92.$$

Yakhot et al. (1984) developed a k-ε model based on the Re-Normalization Group (RNG) theory. The transport equations for k and ε are given as following:

$$\frac{\partial(\rho_g k_g)}{\partial t}+\frac{\partial(\rho_g u_j^g k_g)}{\partial x_j}=\frac{\partial}{\partial x_j}\left(\sigma_k \mu_{eff}\frac{\partial k_g}{\partial x_j}\right)-\rho_g \overline{u_i' u_j'}\frac{\partial u_i^g}{\partial x_j}-\rho_g \varepsilon_g \tag{4.18}$$

$$\frac{\partial(\rho_g \varepsilon_g)}{\partial t}+\frac{\partial(\rho_g u_j^g \varepsilon_g)}{\partial x_j}=\frac{\partial}{\partial x_j}\left(\sigma_\varepsilon \mu_{eff}\frac{\partial \varepsilon_g}{\partial x_j}\right)-C_{1\varepsilon}\frac{\varepsilon_g}{k_g}P_k-\rho_g C_{2\varepsilon}\frac{\varepsilon_g^2}{k_g}-R \tag{4.19}$$

One of difference between the standard and RNG turbulence models is the turbulent viscosity. The scale elimination procedure in RNG theory results in a differential equation for turbulent viscosity μ_{eff} :

$$d\left(\frac{\rho_g^2 k_g}{\sqrt{\varepsilon_g \mu_g}}\right)=1.72\frac{\hat{v}}{\sqrt{\hat{v}^3-1+C_v}}d\hat{v} \tag{4.20}$$

where $\hat{v}=\mu_{eff}/\mu_g$ and C_v=100.

Another difference between the standard and RNG k-ε models is the presence of an additional strain rate term R in the ε-equation (4.19) for the RNG model. The term is modeled as:

$$R = \frac{C_\mu \eta^3 \left(1 - \eta/\eta_o\right)}{1 + \beta \eta^3} \frac{\varepsilon_g^2}{k_g} \tag{4.21}$$

Here, β and η_o are constants with values of 0.015 and 4.38. The significance of the inclusion of this term is its responsiveness towards the effects of rapid rate strain and streamlines curvature, which cannot be properly represented by the standard k-ε model. According to the RNG theory, the constants in the turbulent transport equations are given by σ_k = 0.718, σ_ε = 0.718, $C_{\varepsilon 1}$ = 1.42 and $C_{\varepsilon 2}$ = 1.68 respectively (Yakhot et al., 1984).

Realizable k-ε model

The realizable k-ε model proposed by Shih et al. (1995) was intended to address deficiencies experienced in the standard and RNG k-ε models. The term "realizable" means that the model satisfies certain mathematical constraints on the normal stresses, consistent with the physics of turbulent flows. The k-equation is the same as that in the standard k-ε models except for model constants. The development involved the formulation of a new eddy-viscosity formula involving the variable C_μ in the turbulent viscosity relationship (Equation 4.12)) and a new model for the ε-equation based on the dynamic equation of the mean-square vorticity fluctuation. The following are the k and ε transport equations for the realizable k-ε model:

$$\frac{\partial(\rho_g k_g)}{\partial t}+\frac{\partial(\rho_g u_j^g k_g)}{\partial x_j}=\frac{\partial}{\partial x_j}\left((\mu_g+\frac{\mu_t}{\sigma_k})\frac{\partial k_g}{\partial x_j}\right)-\rho\overline{u_i'u_j'}\frac{\partial u_i^g}{\partial x_j}-\rho_g\varepsilon_g \qquad (4.22)$$

$$\frac{\partial(\rho_g \varepsilon_g)}{\partial t}+\frac{\partial(\rho_g u_j^g \varepsilon_g)}{\partial x_j}=\frac{\partial}{\partial x_j}\left((\mu_g+\frac{\mu_t}{\sigma_k})\frac{\partial \varepsilon_g}{\partial x_j}\right)+\rho_g C_1 S\varepsilon_g-\rho_g C_2\frac{\varepsilon_g^2}{k_g+\sqrt{\frac{\mu_g\varepsilon_g}{\rho_g}}} \qquad (4.23)$$

where S is the mean strain rate $S=\sqrt{2S_{ij}S_{ij}}$. The variable C_1 can be expressed as:

$$\mathrm{C_1}=\max\left[0.43,\frac{\eta}{\eta+5}\right] \text{ and } \qquad \eta=\frac{\kappa_g}{\varepsilon_g}\left(2\mathrm{S_{ij}^2}\right)^{1/2}$$

(4.24)

The variable C_μ, no longer a constant, is computed from:

$$\mathrm{C_\mu}=\frac{1}{\mathrm{A_0}+\mathrm{A_s}\dfrac{k_g \mathrm{U^*}}{\varepsilon_g}};\qquad \mathrm{U^*}\equiv\sqrt{\mathrm{S_{ij}^2}+\tilde{\Omega}_{ij}^2};\qquad \tilde{\Omega}_{ij}=\Omega_{ij}-2\varepsilon_{ijk}\omega_k;\qquad \Omega_{ij}=\overline{\Omega}_{ij}-\varepsilon_{ijk}\omega_k$$

(4.25)

while the model constant A_0 and A_s are determined by:

$$\mathrm{A_0}=4.04;\qquad \mathrm{A_S}=\sqrt{6}\cos\varphi;\qquad \varphi=\frac{1}{3}\cos^{-1}\left(\sqrt{6}\mathrm{W}\right);\qquad \mathrm{W}=\frac{\mathrm{S_{ij}S_{jk}S_{ki}}}{\tilde{\mathrm{S}}^3};\qquad \tilde{\mathrm{S}}=\sqrt{\mathrm{S_{ij}^2}}$$

(4.26)

Other constants in the turbulent transport equations are given to be C_2 = 1.9, σ_κ = 1.0 and σ_ε = 1.2 respectively.

The exact transport equation for the Reynolds stresses $-\overline{u_i'u_j'}$ is shown as below

$$\frac{\partial}{\partial x_k}\left(u_k\overline{u_i'u_j'}\right)=-\left(\overline{u_i'u_k'}\frac{\partial u_j}{\partial x_k}+\overline{u_j'u_k'}\frac{\partial u_i}{\partial x_k}\right)-\frac{\partial}{\partial x_k}\left[\overline{u_i'u_j'u_k'}+\overline{\frac{p}{\rho}\left(\delta_{jk}u_i'+\delta_{ik}u_j'\right)}\right]$$

(i) (ii) (iii)

$$\frac{\partial}{\partial x_k}\left[\upsilon\frac{\partial}{\partial x_k}\left(\overline{u_i'u_j'}\right)\right]+\overline{\frac{p}{\rho}\left(\frac{\partial u_i'}{\partial x_j}+\frac{\partial u_j'}{\partial x_i}\right)}-2\upsilon\overline{\frac{\partial u_i}{\partial x_k}\frac{\partial u_j}{\partial x_k}}$$

(4.27)

(iv) (v) (vi)

The stress convection term (i), the stress production term (ii) and the molecular diffusion term (iv) require no modeling.

A simplified scalar turbulent diffusivity is used to model the turbulent diffusive term (Lien and Leschziner, 1994)

$$-\frac{\partial}{\partial x_k}\left[\overline{u_i'u_j'u_k'}+\overline{\frac{p}{\rho}\left(\delta_{jk}u_i'+\delta_{ik}u_j'\right)}\right]=\frac{\partial}{\partial x_k}\left(\frac{\upsilon_t}{\sigma_k}\frac{\partial\overline{u_i'u_j'}}{\partial x_k}\right)$$

(4.28)

where σ_k is with value of 0.82. υ_t is the turbulent kinematic viscosity defined as $\upsilon_t=C_\mu\frac{k^2}{\varepsilon}$. Where, the turbulence kinetic energy k is obtained by $k=\frac{1}{2}\overline{u_i'u_j'}$ through the flow domain except for the boundary conditions.

The pressure-strain term (v) in equation 1 is decomposed into three parts: a slow return to isotropy term $\Phi_{ij,1}$, a rapid return to isotropy term $\Phi_{ij,2}$ and the pressure-strain wall-echo term $\Phi_{ij,\omega}$. The slow return to isotropy term is modeled as $\Phi_{ij,1}=-C_1\rho\frac{\varepsilon}{k}\left(\overline{u_i'u_j'}-\frac{2}{3}\delta_{ij}k\right)$. Where, C_1 = 1.8. The rapid pressure-strain term is modeled as $\Phi_{ij,2}=-C_2\left[\left(P_{ij}-C_{ij}\right)-\frac{2}{3}\delta_{ij}\left(P-C\right)\right]$. Where C_2 = 0.6, P_{ij} and C_{ij} are the

stress production term and the convection term. $P = \frac{1}{2}P_{kk}$, $C = \frac{1}{2}C_{kk}$. The pressure-strain wall-echo term $\Phi_{ij,\omega}$ redistributes the normal stresses near the wall by damping the normal stresses perpendicular to the wall, while enhancing the stresses parallel to the wall. It is modeled as :

$$\Phi_{ij,\omega} = C_1' \frac{\varepsilon}{k}\left(\overline{u_k' u_m'} n_k n_m \delta_{ij} - \frac{3}{2}\overline{u_i' u_k'} n_j n_k - \frac{3}{2}\overline{u_j' u_k'} n_i n_k\right)\frac{k^{2/3}}{C_l \varepsilon d}$$

$$+ C_2'\left(\phi_{km,2} n_k n_m \delta_{ij} - \frac{3}{2}\phi_{ik,2} n_j n_k - \frac{3}{2}\phi_{jk,2} n_i n_k\right)\frac{k^{2/3}}{C_l \varepsilon d} \qquad (4.29)$$

where $C_1' = 0.5$, $C_2' = 0.3$. n_k is the x_k component of the unit normal to the wall, d is the normal distance to the wall. $C_l = C_\mu^{3/4} / K$, where . K is the von Karman constant with the value of 0.4178.

The dissipation tensor (vi) in equation 1 is modeled by $-2\upsilon\overline{\frac{\partial u_i}{\partial x_k}\frac{\partial u_j}{\partial x_k}} = \frac{2}{3}\delta_{ij}\varepsilon$. The scalar dissipation rate, ε , is calculated by a transport equation as following:

$$\frac{\partial}{\partial x_i}(\varepsilon u_i) = \frac{\partial}{\partial x_j}\left[\left(\upsilon + \frac{\upsilon_t}{\sigma_\varepsilon}\right)\frac{\partial \varepsilon}{\partial x_j}\right] + C_{\varepsilon 1}\frac{P_{ii}\varepsilon}{2k\rho} - C_{\varepsilon 2}\frac{\varepsilon^2}{k} \qquad (4.30)$$

where $\sigma_\varepsilon = 1.0$, $C_{\varepsilon 1} = 1.44$, $C_{\varepsilon 2} = 1.92$.

Reynolds Stress Model (RSM)

In this study, a second order RSM turbulence model is used and the transport equation for the Reynolds stresses $-\overline{u_i' u_j'}$ is given by:

$$\frac{\partial}{\partial x_k}\left(u_k \overline{u_i' u_j'}\right) = -\left(\overline{u_i' u_k'}\frac{\partial u_j}{\partial x_k} + \overline{u_j' u_k'}\frac{\partial u_i}{\partial x_k}\right) - \frac{\partial}{\partial x_k}\left[\overline{u_i' u_j' u_k'} + \overline{\frac{p}{\rho}\left(\delta_{jk} u_i' + \delta_{ik} u_j'\right)}\right]$$

(i) (ii) (iii)

$$+\frac{\partial}{\partial x_k}\left[\upsilon\frac{\partial}{\partial x_k}\left(\overline{u_i' u_j'}\right)\right]+\overline{\frac{p}{\rho}\left(\frac{\partial u_i'}{\partial x_j}+\frac{\partial u_j'}{\partial x_i}\right)}-2\upsilon\overline{\frac{\partial u_i}{\partial x_k}\frac{\partial u_j}{\partial x_k}} \tag{4.31}$$

(iv) (v) (vi)

The terms indicated in Eq. (4.31) that require no modeling are: (i) convection term, (ii) production and (iv) the molecular diffusion term.

For term (iii), a simplified scalar turbulent diffusivity is used to model the turbulent diffusive term (Lien and Leschziner, 1994):

$$-\frac{\partial}{\partial x_k}\left[\overline{u_i' u_j' u_k'}+\overline{\frac{p}{\rho}\left(\delta_{jk}u_i'+\delta_{ik}u_j'\right)}\right]=\frac{\partial}{\partial x_k}\left(\frac{\upsilon_t}{\sigma_k}\frac{\partial\overline{u_i' u_j'}}{\partial x_k}\right) \tag{4.32}$$

where σ_k is with value of 0.82. υ_t is the turbulent kinematic viscosity defined as $\upsilon_t = C_\mu \frac{k^2}{\varepsilon}$. The turbulence kinetic energy k is obtained by $k=\frac{1}{2}\overline{u_i' u_j'}$ through the flow domain except for the boundary conditions.

The pressure-strain term (v) in Eq. (4.31) can be decomposed into three parts: a slow return to isotropy term $\Phi_{ij,1}$, a rapid return to isotropy term $\Phi_{ij,2}$ and the pressure-strain wall-echo term $\Phi_{ij,\omega}$. The slow return to isotropy term is modeled as

$$\Phi_{ij,1}=-C_1\rho\frac{\varepsilon}{k}\left(\overline{u_i' u_j'}-\frac{2}{3}\delta_{ij}k\right) \tag{4.33}$$

where $C_1 = 1.8$. The rapid pressure-strain term is modeled as

$$\Phi_{ij,2} = -C_2\left[\left(P_{ij} - C_{ij}\right) - \frac{2}{3}\delta_{ij}\left(P - C\right)\right] \tag{4.34}$$

where C_2 = 0.6 and P_{ij} and C_{ij} are respectively the stress production and convection terms: $P = \frac{1}{2}P_{kk}$ and $C = \frac{1}{2}C_{kk}$. The pressure-strain wall-echo term $\Phi_{ij,\omega}$ redistributes the normal stresses near the wall by damping the normal stresses perpendicular to the wall while enhancing the stresses parallel to the wall. It is modeled as:

$$\begin{aligned}\Phi_{ij,\omega} = {} & C_1^{'}\frac{\varepsilon}{k}\left(\overline{u_k^{'}u_m^{'}}n_k n_m\delta_{ij} - \frac{3}{2}\overline{u_i^{'}u_k^{'}}n_j n_k - \frac{3}{2}\overline{u_j^{'}u_k^{'}}n_i n_k\right)\frac{k^{2/3}}{C_l \varepsilon d} \\ & + C_2^{'}\left(\phi_{km,2}n_k n_m\delta_{ij} - \frac{3}{2}\phi_{ik,2}n_j n_k - \frac{3}{2}\phi_{jk,2}n_i n_k\right)\frac{k^{2/3}}{C_l \varepsilon d}\end{aligned} \tag{4.35}$$

where the constants of $C_1^{'}$ and $C_2^{'}$ have values of 0.5 and 0.3 respectively. The variables n_k is the x_k component of the unit normal to the wall, d is the normal distance to the wall and $C_l = C_\mu^{3/4}/K$ where K is the von Karman constant with a value of 0.4178.

The dissipation tensor (vi) in Eq. (4.31) is modeled by

$$-2\upsilon\overline{\frac{\partial u_i}{\partial x_k}\frac{\partial u_j}{\partial x_k}} = \frac{2}{3}\delta_{ij}\varepsilon \tag{4.36}$$

The scalar dissipation rate ε is calculated according through a transport equation:

$$\frac{\partial}{\partial x_i}(\varepsilon u_i) = \frac{\partial}{\partial x_j}\left[\left(\upsilon + \frac{\upsilon_t}{\sigma_\varepsilon}\right)\frac{\partial \varepsilon}{\partial x_j}\right] + C_{\varepsilon 1}\frac{P_{ii}\varepsilon}{2k\rho} - C_{\varepsilon 2}\frac{\varepsilon^2}{k} \tag{4.37}$$

where $\sigma_\varepsilon = 1.0$, $C_{\varepsilon 1} = 1.44$ and $C_{\varepsilon 2} = 1.92$.

4.3 Particle phase modeling - Eulerian-Lagrangian model

A Lagrangian-formulated particle equation of motion is solved using FLUENT. The trajectory of a discrete particle phase is determined by integrating the force balance on the particle. This force balance equates the particle inertia with the forces acting on the particle. Appropriate forces such as the drag and gravitational forces have been incorporated into the equation of motion. The equation can be written as

$$\frac{\partial u_i^p}{\partial t} = F_D\left(u_i^g - u_i^p\right) + g\left(\rho_p - \rho_g\right) \tag{4.38}$$

where $F_D\left(u_i^g - u_i^p\right)$ is the drag force per unit particle mass, and F_D is given by

$$F_D = \frac{18\mu_g C_D \,\mathrm{Re}_p}{24\rho_p d_p^2} \tag{4.39}$$

where ρ_p denotes the density of particle material and dp is the particle diameter. u_i^p presents the particle velocity. Re_p is the relative Reynolds number defined as

$$\mathrm{Re}_p = \frac{\rho_g d_p \left|u_p - u_g\right|}{\mu_g} \tag{4.40}$$

The drag coefficient (C_D) is correlated as a function of the Re_p

$$C_D = \begin{cases} 0.44 & Re_p > 1000 \\ \dfrac{24}{Re_p}\left(1.0 + \dfrac{1}{6}Re_p^{0.66}\right) & Re_p < 1000 \end{cases} \quad (4.41)$$

The CFD code, FLUENT, handles the turbulent dispersion of particles by integrating the trajectory equations for individual particles, using the instantaneous fluid velocity, $u_i^g + u_i'(t)$, along the particle path during the integration process. Here, a stochastic method, discrete random walk or "eddy lifetime" model, is utilised where the fluctuating velocity components u_i' that prevail during the lifetime of the turbulent eddy are sampled by assuming that they obey a Gaussian probability distribution, so that $u_i' = \zeta\sqrt{\overline{u_i'^2}}$. Here ζ is a normally distributed random number, and the remaining right-hand side is the local root mean square (RMS) velocity fluctuations can be obtained (assuming isotropy) by $\sqrt{\overline{u_g'^2}} = \sqrt{2k_g/3}$. The interaction time between the particles and eddies is smaller of the eddy lifetime τ_e and the particle eddy crossing time t_{cross} . The characteristic lifetime of the eddy is calculated as:

$$\tau_e = -T_L \log(r) \quad (4.42)$$

where T_L is the fluid Lagrangian integral time, $T_L \approx 0.15 k_g/\varepsilon_g$. The variable r is a uniform random number between 0 and 1. The particle eddy crossing time is given by:

$$t_{cross} = -t_p \ln\left[1 - \left(\frac{Le}{t_p\left|u_i^g - u_i^p\right|}\right)\right] \quad (4.43)$$

where t_p is the particle relaxation time ($= \rho_p d_p^2/18\rho_g v_g$) , Le is the eddy length scale and $\left|u_i^g - u_i^p\right|$ is the magnitude of the relative velocity. The particle interacts with the

fluid eddy over the interaction time. When the eddy lifetime is reached, a new value of the instantaneous velocity is obtained by applying a new value of ζ. In the coupled approach, as the continuous phase flow pattern is NOT impacted by the discrete phase (and vice versa), an uncoupled approach or "one-way coupling" was used to predict the discrete phase patterns based on a fixed continuous phase flow field.

The governing transport equations are discretised using the finite volume approach. The QUICK scheme is used to approximate the convective terms while the second order accurate central difference scheme is adopted for the diffusion terms. The pressure-velocity coupling is realized through SIMPLE method.

Chapter 5: Experimental Methods and Measurements

5.1 Experimental technique

Particle Image Velocimetry (PIV) is a technique that allows for the instantaneous measurement of two components of fluid velocity within a plane defined by a laser sheet. PIV has very recently matured and proven to be a powerful tool for studying a wide range of fluid flows. In this section, a brief introduction to PIV system is present. We also discuss the quantities measured and derived from PIV data, and the error, uncertainty, and spatial and temporal resolution of the technique.

5.1.1 Introduction to PIV

Optical measurement techniques offer several advantages over physical probes. First, traditional mechanical measurement probes may distort the flow that they are measuring. Secondly, optical techniques offer the advantage that light may be used to probe regions in which one could not easily locate a physical probe, such as the small clearance regions inside the nasal cavity.

PIV is a technique that measures the instantaneous velocity field within an illuminated plane of the fluid field using light scattered from particles seeded into the fluid. The light scattered from these particles is collected and imaged using a camera at two separate times so that the displacement of the particles can be measured. Using a laser as a light source, it is possible to very accurately locate and shape this illuminated plane so that one can make measurements within a very thin measurement volume.

One of two methods is generally used to control this timing of image acquisition. The two images may be obtained using a continuous laser sheet and a regulated shutter

on the camera. Alternatively, the camera can gather scattered light over an extended period while the pulsing light source controls the precise timing of the particle images. Using a pulsed laser, it can be ensured that each of these image pairs may be obtained at an effectively instantaneous time and that the precise time separation between the two images of the pair is known. During the time between these two images, the particles within the fluid will move a distance that is proportional to the fluid velocity. After obtaining the images, the local fluid velocity, u, is found from $u = \delta/\Delta t$ where δ is the particle displacement and Δt is the time between the two images.

PIV systems use digital cameras and computers to perform the image acquisition and measurement the particle displacement. Successive image pairs of the particles within a laser plane are captured with a high-speed digital CCD (Charge-Coupled Device) camera. Using a pulsed laser, each of these image pairs is obtained at an effectively instantaneous time. As the precise time separation between the images pair is known, it is possible to calculate the local velocity at any sub-region of these acquired images by measuring the distance that particles have traveled between these images.

5.1.2 Important considerations in PIV

The performance of a PIV system is determined by the spatial resolution, the particle mage detection rate, and the accuracy and reliability of the velocity measurements. These system characteristics are affected by many factors, such as the type of flow seeding particles, image interrogation method, velocity gradients, and image recording media. Each of these issues will be discussed in the context of the PIV

system being used for this research: a single-exposure, double-frame PIV system employing the cross-correlation image processing.

Flow seeding particle

PIV measures the velocity of seeding particles suspended in the fluid rather than the velocity of the fluid itself, so it is imperative to understand how the velocity of the particles relates to the velocity of the fluid. The response of a seeding particle to fluid velocity fluctuations depends on the size, shape, and density of the particle, as well as the density and viscosity of the fluid.

The flow-tracking behavior of a seeding particle is governed by Bassett's equation, the equation of motion for sphere in a homogeneous viscous fluid. Non-dimensionalization shows that the solution to Bassett's equation is a function of two independent parameters, the density ratio and Stokes number. The Stokes number is the ratio of the viscous drag to the particle's inertia. As the Stokes number decreases, the amplitude ratio and phase change decline. The amplitude ratio and phase change indicate the particle's ability to track the amplitude and phase changes of the flow fluctuations. In general, the best seeding material has the same density as the flow. Theoretically, this will result in the same fluid and particle velocities regardless of particle diameter.

Image interrogation method

This part concentrates on interrogation nodes, the algorithms they use and the manner in which they may be applied. Almost invariably the first interrogation pass on raw PIV images is applied using a simple correlation technique. Correlation techniques are the most widespread in PIV and in cases where only single pass interrogation is used it is typically a correlation method.

Secondary and tertiary interrogation methods utilise first pass information to improve upon the data obtained in the first pass. This is achieved by the use of offset interrogation areas and a technique that unlike correlation identifies the location of the individual particle images within interrogation areas. This enables individual image pairs to be matched so allowing any variation in the particle displacement across the interrogation area to be measured. This ultimately reduces random errors compared to pure correlation techniques as well as increasing the range of spatial flow scales that can be extracted from PIV images.

The standard and most common methods for PIV interrogation are autocorrelation and cross-correlation. Autocorrelation is applied to a single image onto which two or more exposures are recorded. Applying autocorrelation produces correlation function with a characteristic central or self correlation peak which plus symmetrical displacement correlation peaks. Reversals in flow direction beyond 180 degrees cannot be measured unambiguously by autocorrelation.

Separate recording of the first and second exposure onto separate images removes the ambiguity in the direction of the flow and this is most commonly extracted using cross-correlation. The cross correlation function has no central correlation peak and has only a single displacement correlation peak.

Both autocorrelation and cross-correlation determine the local displacement of particles by estimating the sub-pixel position of the displacement correlation peak. The peak position is representative of the local average particle displacement.

The data yield can be considerable improved by using an offset between the base and the cross interrogation areas that is equal to the local particle displacement. Measurement noise is also reduced when the offset between base and cross is within 0.5

of a pixel of the real displacement. Offsets are generated for this technique using the standard cross-correlation technique followed by vector filtering and interpolation. The resulting vector maps at the interpolation node are then used by adaptive cross-correlation to achieve a higher data yield (fewer outliers) while also allowing the use of smaller interrogation areas to achieve higher spatial resolution.

The performance of cross-correlation interrogation to two single exposed PIV images can be increased in terms of data yield, accuracy and spatial resolution when the base and cross interrogation areas are offset from each other by a value that is close (within 0.5 pixels) to the actual displacement at that location of the image. The value of the correct offset will thus vary across the whole area of the image, apart from cases where the flow is of approximately of the same direction and magnitude.

Typical usage of adaptive cross-correlation would be as follows:

Step 1: Perform standard cross-correlation processing of a pair of PIV images using a large interrogation area (64*64) and little or no interrogation window overlap.

Step 2: Filter the resulting vector-map using global and local filtering, then apply interpolation to the missing sites.

Step 3: Using the resulting vector-map applies adaptive cross-correlation using a smaller interrogation window than in step 1 (32*32) and an overlap (possibly up to 50%).

Step 4: Steps 2 and 3 may be repeated possibly with a smaller interrogation area and smaller interrogation separation. The smallest interrogation window that may be used will depend on the particle concentration. A practical minimum of about 5 complete particle image pairs is required.

If a reduction in the interrogation area dimension is possible when using adaptive cross-correlation the variation in displacement/velocity across the interrogation area is reduced and a direct improvement in the final spatial resolution is achieved. Despite this there is still scope for a further improvement in spatial resolution by tracking individual particle images. The flow field varies continuously in its x, y and z component of velocity but it is randomly represented in a PIV image by the random locations of the particle images. The measured displacement/velocity from a point interrogation is therefore formed of the sum of a limited number of contributions format the randomly located particle image pairs.

The variation in velocity across an interrogation area is not discernable from the single value obtained from the position of the cross-correlation peak. Any variation in flow velocity within the interrogation area coupled with the random locations of particle image pairs results in a random component in the velocity measurement. The random component increases with the local variation in velocity across the interrogation area and inversely with the seeding concentration.

Reducing the interrogation diameter decreases the random component in the velocity measurement but only provides benefits while sufficient particles remain within the interrogation spot. The lower limit on the interrogation area is ultimately imposed by the particle concentration which is itself limited by particle size and the requirement for PIV that the particles images do not overlap.

In practice the interrogation diameter may be reduced to 16 pixels square and 8 pixels square when the seeding concentration is approaching the threshold of speckle. When adaptive correlation is used to this level the only means to achieving higher precision is to track individual particles. This method has been termed super resolution

PIV and is different to traditional particle tracking which is not preceded by correlation processing and for which reliable results are obtained only with the addition of pre-information about the nature of the flow.

5.2 Experimental set-up

In this section, the creations of components of experimental set-up, such as physical model and flow rigs, are described.

5.2.1 Pharynx model

Acrylic model

In order to build realistic pharynx physical model for experimental studies, a computer model is created from CT scan image files. The image files are converted into three-dimensional volume files and then save as a stereolithography (STL) file, which is a standard format for further processing. CAD model based on the STL geometry is developed using Solidworks package. Manufacturing based on the CAD model is done using a Computer Numerical Control (CNC) machine. Due to the difficulty of making a hollow flow passage, which includes a 90 degree bend, in an acrylic block, the following procedures were employed.

1. Split the computer model along the central sagittal plane into two halves,
2. Manufacture each half part using CNC machine in two acrylic blocks, as shown in Fig. 5.1(a)
3. Assemble the two blocks together using glue and screws, as shown in Fig. 5.1(b), and a flow passage in a transparent acrylic block is produced, as show in Fig. 5.1(c). The acrylic model is relatively durable and can withstand subsequent drilling and testing.

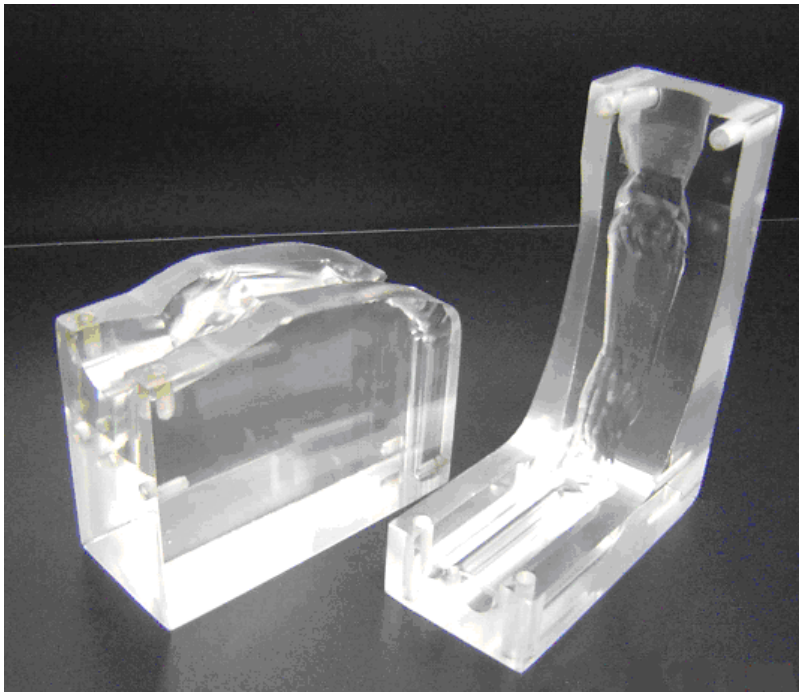

(a)

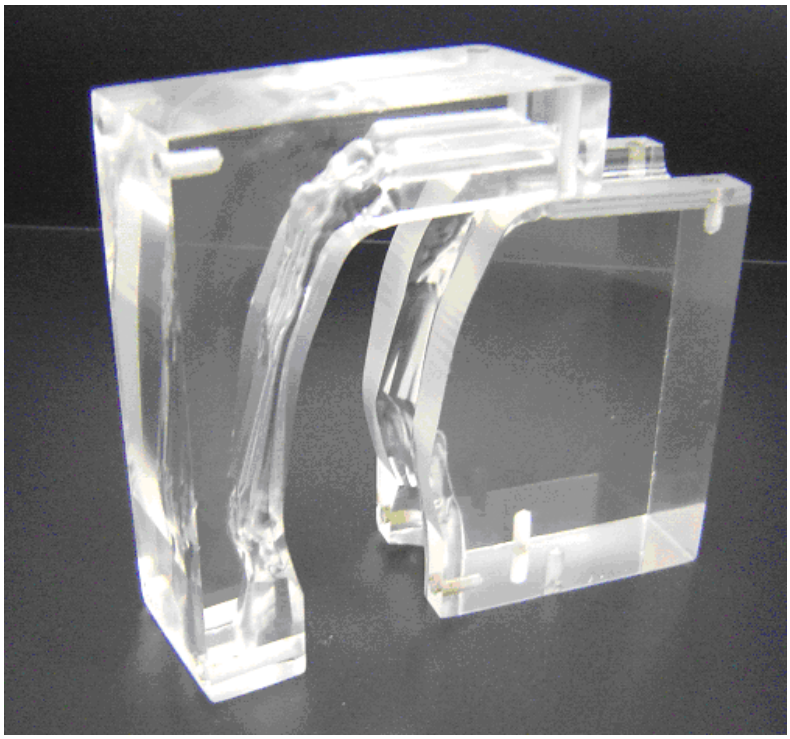

(b)

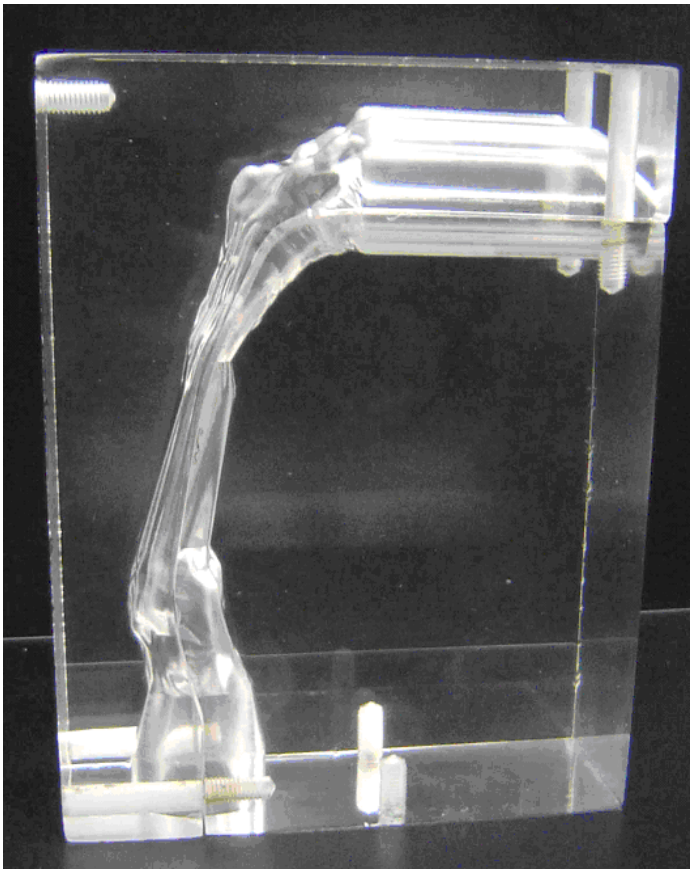

(c)

Fig. 5.1 The realistic pharynx physical (acrylic) model

Flow rig

The flow rig mainly comprised a physical model, a fluid tank, and a suction pump. As showed in Fig. 5.2, the model was supported on a flat plate, submerged into the tank, and connected to the pump. The pump was also connected to a transformer allowing control the flow rate. To eliminate the refraction of the laser sheet as it passes through the flow passage, the index of refraction of the working fluid was matched to the models. In this PIV measurement, we used a mixture of water and glycerol (20:80 in weight, $\upsilon = 51.3\times10^{-5}$ m^2/s at 25 °C).

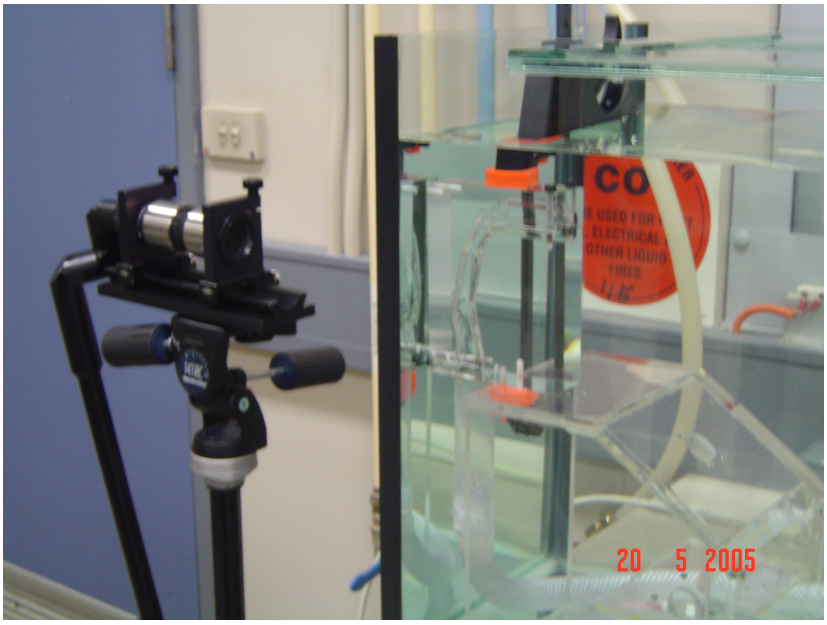

Fig. 5.2 The experimental set-up of pharynx physical model

5.2.2 Silicone model

Due to the complex geometry, the physical model human nasal cavity is made of silicone rather than acrylic using rapid prototyping techniques.

Rapid prototyping is a well-accepted method for quickly generating replicate prototypes from computer files. There are various rapid prototyping machines that use different materials to produce replicate parts. In essence, these machines are three-dimensional printers with a range of accuracy. The key to producing a model suitable for PIV is the recent availability of a rapid prototyping machine that produces the part in water-soluble consolidated cornstarch. The general procedure for building the replicate model is:

1. Create a solid computer model of the nasal cavity geometry,

2. Obtain a water-soluble negative of the nasal cavity using rapid prototyping techniques,

3. Encase the negative in transparent silicone,

4. Dissolve the negative to leave the replicate model.

Each step in the procedure is now described in detail.

Creation of the solid computer model

Since the heart of the method is rapid prototyping, the first step is to obtain an accurate solid geometrical computer model of the nasal cavity. In our application, the flow passage is the human nasal cavity and a computer rendition was obtained initially using computed tomography (CT). Slices of the three-dimensional CT image were taken at 83 positions from the entrance to the nasal cavity to slightly anterior to the nasopharynx. Images were taken at 1 to 5 mm intervals depending on the complexity of the anatomy and points on their perimeter were selected for storage.

The model was scaled to twice its human counterpart to improve flow measurements in some of the smaller airways. The solid computer model was then saved as a stereolithography (STL) file, which is a standard format compatible with rapid prototyping machines. The ultimate goal of forming a solid computer model from CT scan data is the creation of an STL file that describes the scaled replica of the flow passage. In biological applications, this is necessarily quite involved since the data must be translated from a voxel-based format. In more man-made applications, the shape of the flow passage may already be available in a computer-compatible format that facilitates its translation to STL format. Numerous software products, many of them available free in the public domain, can convert solid modelling data to and from STL format.

Rapid prototyping and prototype preparation

The STL file describes and therefore is the negative of the flow passage geometry. The key to obtaining the corresponding positive geometry is a rapid prototyping machine that produces water-soluble prototypes. It produces prototypes

from consolidated cornstarch that are brittle and porous. Typically, the prototypes are filled with wax or cyanoacrylate to increase their strength, rendering them insoluble. For this application, the prototype is ordered from Z Corporation without treatment so that the acquired part is water-soluble. In this state, the cornstarch prototype is delicate and must be handled carefully. The prototype is then painted with approximately five coats of water-soluble glue to seal the pores at the surface and improve strength. Care must be taken to apply only a thin layer of glue at a time to eliminate the possibility of the glue dissolving or warping the prototype.

Fig. 5.3 The prototype is suspended in a Plexiglas box

Model casting procedure

The flow passage is made of clear silicone because (a) it can be poured around the prototype and (b) it is transparent to the wavelength and intensity of laser light used

for PIV. As shown in Fig. 5.3, the prototype is suspended in a Plexiglas box. The box should have flat sides to minimize optical distortion during the PIV recording stage. The distance from the prototype to the edge of the box should be thin enough that the scattered light is not overly attenuated, but not so thin that the pressure in the flow passage will damage or distend the model. Typical spacing is about 2 cm in our application.

Care must be taken when mixing the silicone and curing agent to insure homogeneous properties while minimizing air entrainment. When thoroughly mixed, the silicone and curing agent are exposed to a vacuum to remove air bubbles and dissolved air, as showed in Fig.5.4. Excessive exposure to vacuum may also remove the curing agent thereby slowing the curing process. The silicone is then carefully poured into the Plexiglas box through a funnel and tubing to minimize air entrainment. Figure 5.5 presents the process of model casting. After the silicone has cured, the cornstarch prototype is removed by first submerging the model in water. The water will soften the cornstarch near the entrance and exit tubes. The more interior portions can be removed by flowing water through a flexible tube and manually applying this flow to remaining sections of the prototype. If the prototype was not thoroughly coated with glue, silicone will leak into the cornstarch. The consequence of this leakage is twofold. First, the silicone that seeps into the cornstarch will harden making the removal of the cornstarch a tedious process. Second, the silicone may displace some air in the cornstarch. This displaced air may be trapped in the model in the form of small air bubbles as the silicone hardens. After the prototype has been dissolved, a replica of the flow passage is imbedded in the clear silicone.

Fig. 5.4 The mixed silicone and curing agent are exposed to a vacuum to remove air bubbles and dissolved air

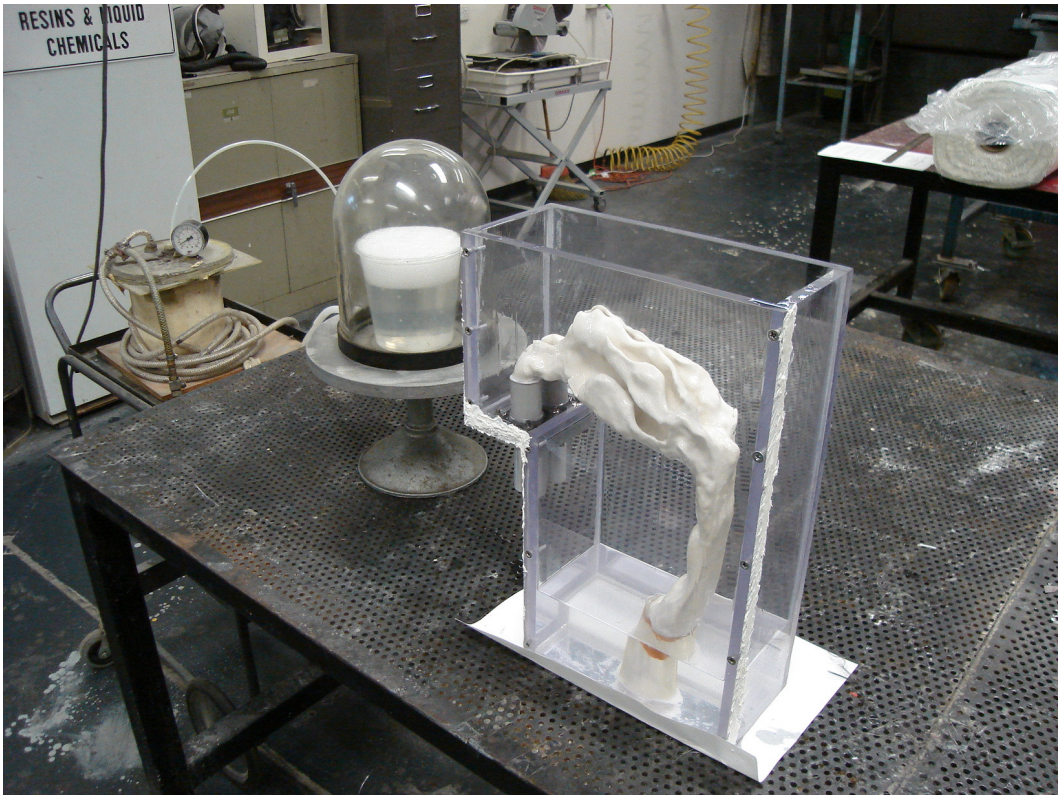

Fig. 5.5 Model casting is on process

5.2.3 PIV set-up

Figure 5.6 is a schematic diagram of the PIV apparatus. The single-phase fluid flow field within the airway was measured using 2D particle image velocimetry (PIV). The ILA 2D PIV system consists of a 1.3Megapixel *(*1280 × 1024 pixels*)* 12-bit digital CCD camera with 200 ns shortest frame straddling time which was synchronised with a New Wave 120 mJ double-cavity Nd:YAG laser. The laser beam was expanded by a cylindrical lens to form a 2mm thick plane vertical light sheet that was directed through the airway. The laser head was supported on a horizontal traverser, allowed the measurement plane to be moved by a repeatable and quantifiable amount. Measurements were taken in 3mm slices in sagittal planes from the left side to the right side. The field of view of the CCD camera was 165 × 132mm^2 using 1280 × 1028 pixels of CCD array. The smallest resolvable length scale of the PIV set-up, which is the real length of each pixel, equals 128.9μm. The seeding particles used were TSI silver-coated hollow glass beads with mean diameter of 14μm and relative density of 1.65 to water, which were small enough to follow the flow faithfully and large enough to reflect sufficient light to be detectable.

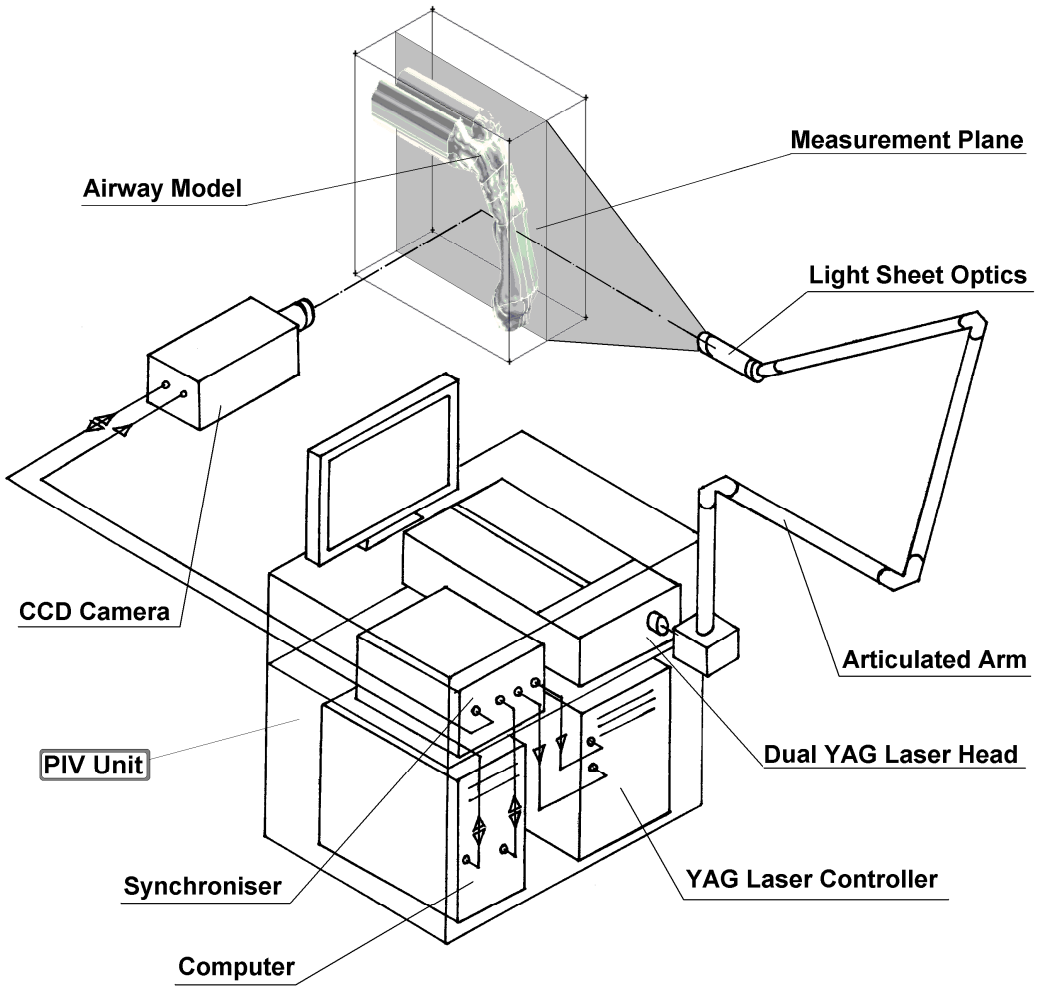

Fig. 5.6 Schematic diagram of the PIV apparatus

In summary, this chapter mainly introduces PIV technique, which employed in this experimental study. Also, the procedures of creation airway physical model are described detailed. The measurement results will be present and discussed in the next chapter.

Chapter 6: Results and Discussion

6.1 Nasopharynx and pharynx airway

This section presents a numerical and experimental study of airflows in an anatomically accurate geometry of human nasopharynx and pharynx airway, which has been generated by Computed Tomography (CT) scanner. As the standard k-ε model has demonstrated to perform rather poorly in predicting the EX flows (Stapleton et al., 2000), a second order Reynolds Stress model (RSM) is used for the numerical simulation. To gain the confidence of the RSM predictions, a 1:1 experimental model based on the geometry of numerical model, is built and measured by using the Particle Image Velocimetry (PIV) technique. The comparison between the numerical results and experimental data has been made, and a reasonable agreement is achieved. The combination of numerical and experimental results will lead to a confidence in performance of RSM model and better understanding of the airflow behaviors, wall shear stress distribution, and further the particle deposition patterns in human airway.

For the numerical simulation, two inlet velocities, 1m/s that can be found in light exercise and 10 m/s that can be found in heavy exercise and sneezing, are used. The air temperature is assumed to be 25 °C and the air kinemetic viscosity is 1.565×10^{-5} m^2/s. Since a water/glycerol mixture was used as the working fluid in the experimental study, the Reynolds number (Re) must match the real air breathing conditions to achieve dynamic similarity. The dimensionless parameter, the Reynolds number is often used to determine the flow regime by comparing the ratio of the inertial forces to the viscous forces and is given as: $\mathrm{Re} = \frac{UL}{\upsilon}$, where v = kinematic viscosity, U =

velocity and L = a characteristic length. In experimental study, the kinematic viscosity of the mixture of water and glycerol is 51.3×10^{-5} m^2/s. To ensure the Reynolds number is the same as the airflow at 1m/s, the inlet velocity of the mixture fluid was set to be 3.3 m/s.

6.1.1 Validation

The CFD results have been compared with our experimental data. Figure 6.1 presents the global velocity maps at the center-plane of airway. The flow field measure by PIV is shown on the left side and the corresponding CFD prediction on the right. The velocity plots indicate that the basic structure of the flow field is modeled well with the measurements in both shape and magnitude. The major separation region near the outlet is well captured. The significant flow development occurs just after 90^o nasopharynx turn. The CFD velocity profile also show a boundary layer on the posterior pharynx wall. This feature is not present in the experimental result. This may be due to the fact that PIV measurements are particularly noisy in the region, which is near the solid surfaces. Figure 6.2 shows the axial velocity profiles at three different locations at the center-plane of airway. d* is dimensionless arc length, and u* is velocity normalized by inlet velocity ($u^*=u/u_{in}$), There are some differences between the two results but overall the distribution and magnitudes of the mean velocities are very similar. With the quantitative comparison of PIV and CFD result, the good agreements instill confidence that the present CFD model is sufficiently accurate to analyze airflow in the airway.

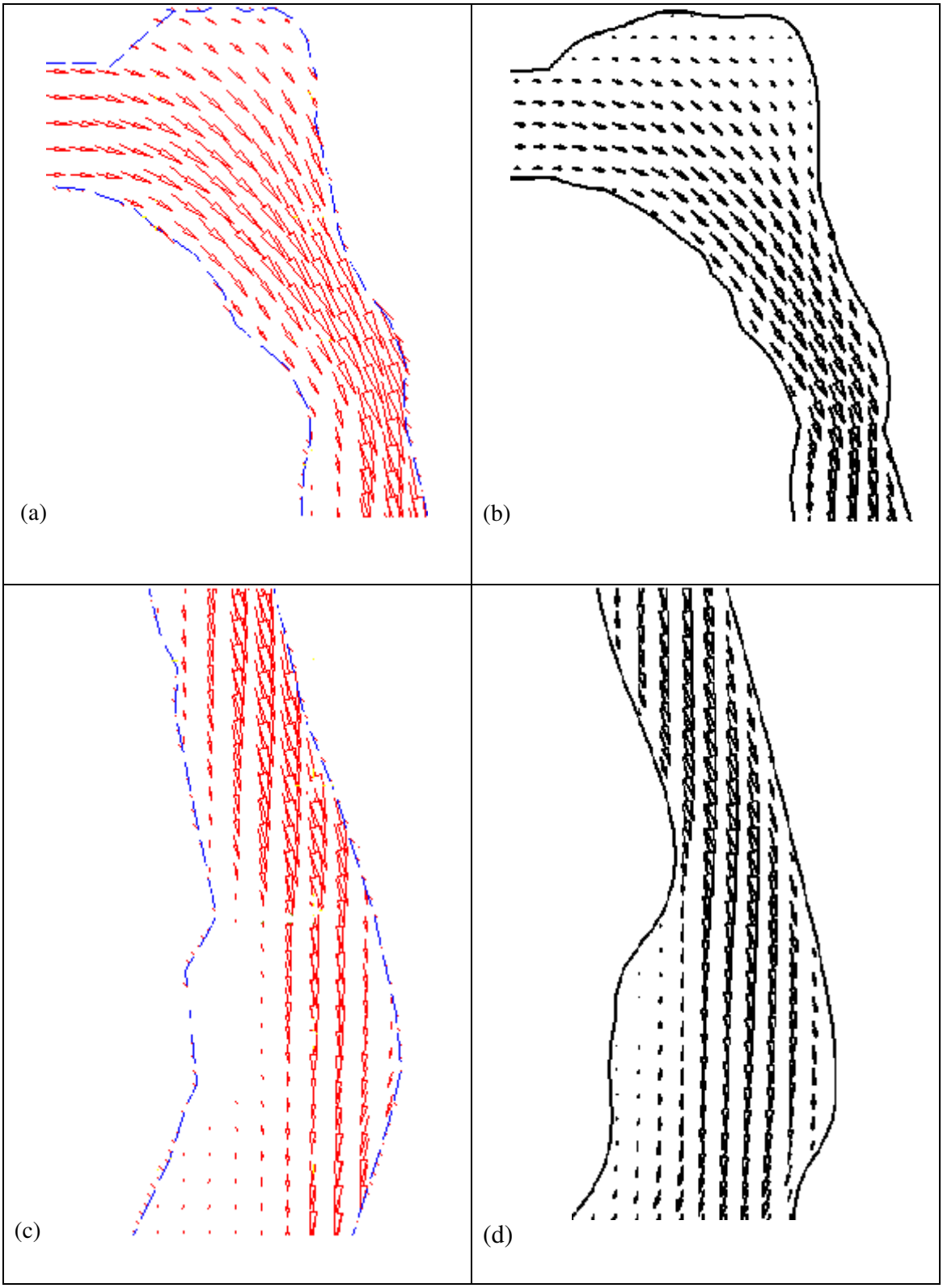

Fig. 6.1 Comparison of flow patterns at mid plane obtained by PIV measurement (a and c) and CFD prediction (b and d).

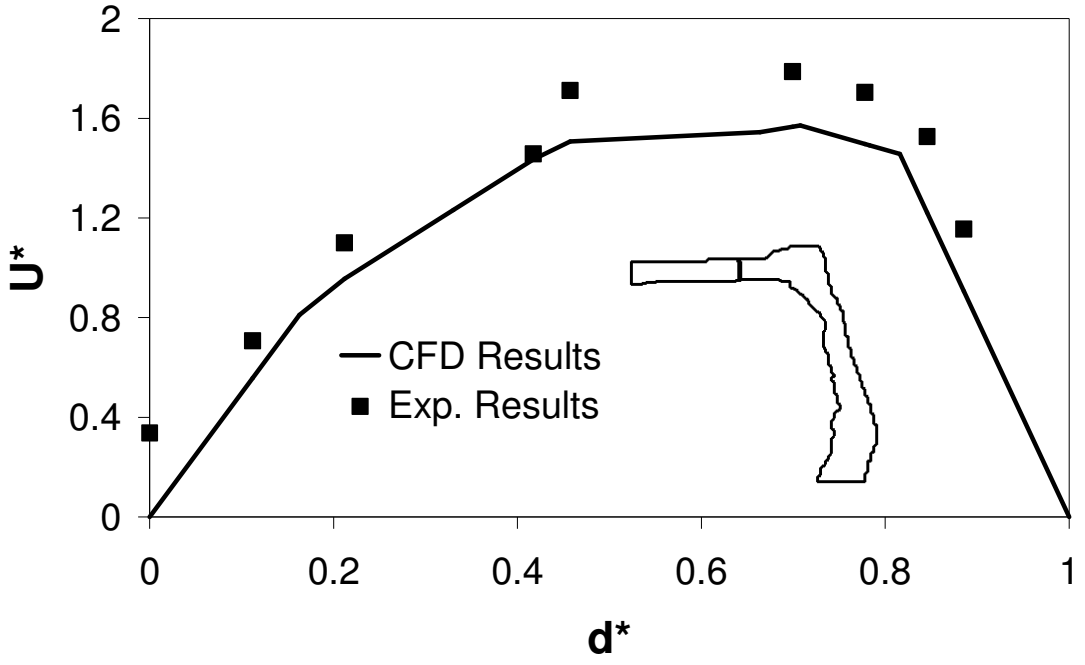
2
1.6
1.2
0.8
0.4
0
U*
CFD Results
Exp. Results
0
0.2
0.4
0.6
0.8
1
d*

(a)

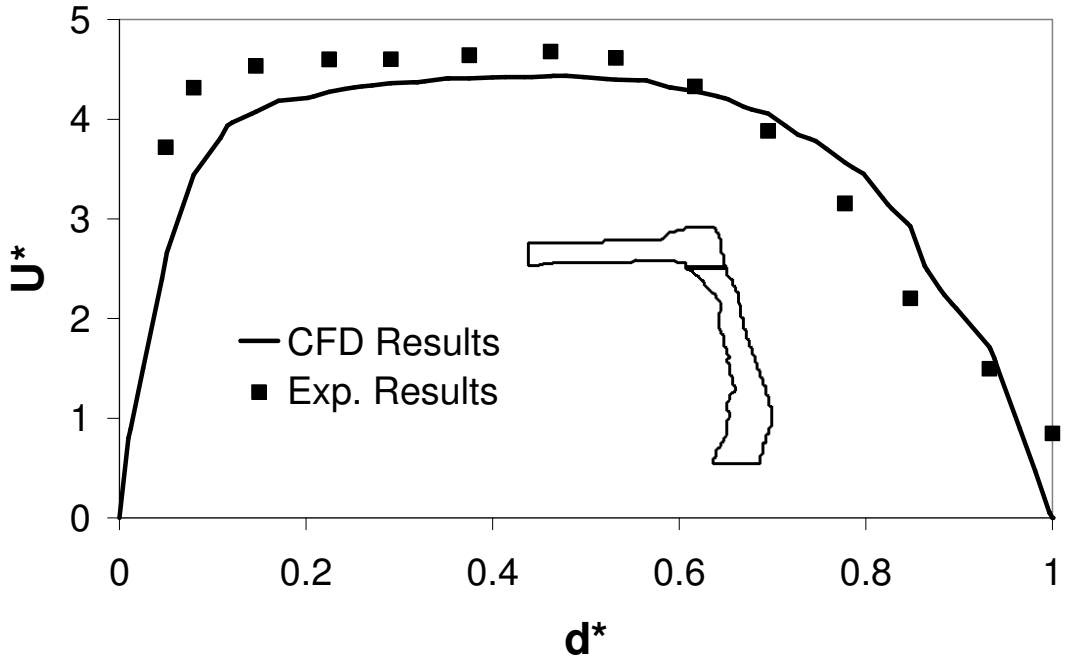
5
4
3
2
1
0
U*
CFD Results
Exp. Results
0
0.2
0.4
0.6
0.8
1
d*

(b)

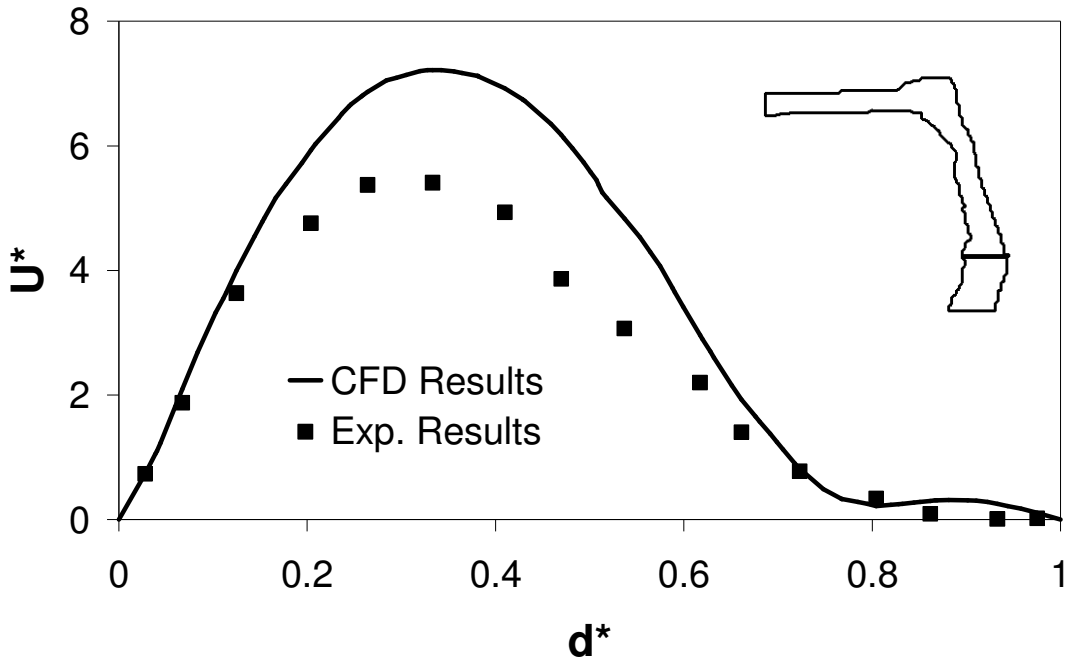

(c)

Fig. 6.2 Comparison of measured and predicted velocity vectors along three different lines. d* is dimensionless length, $u^*=u/u_{in}$.

6.1.2 Airflow patterns in human nasopharynx and pharynx airway

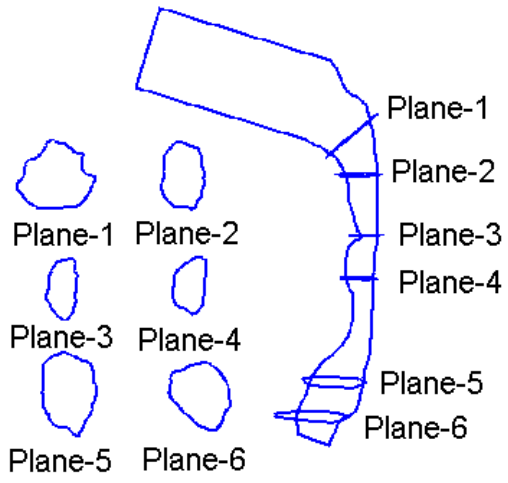

(a)

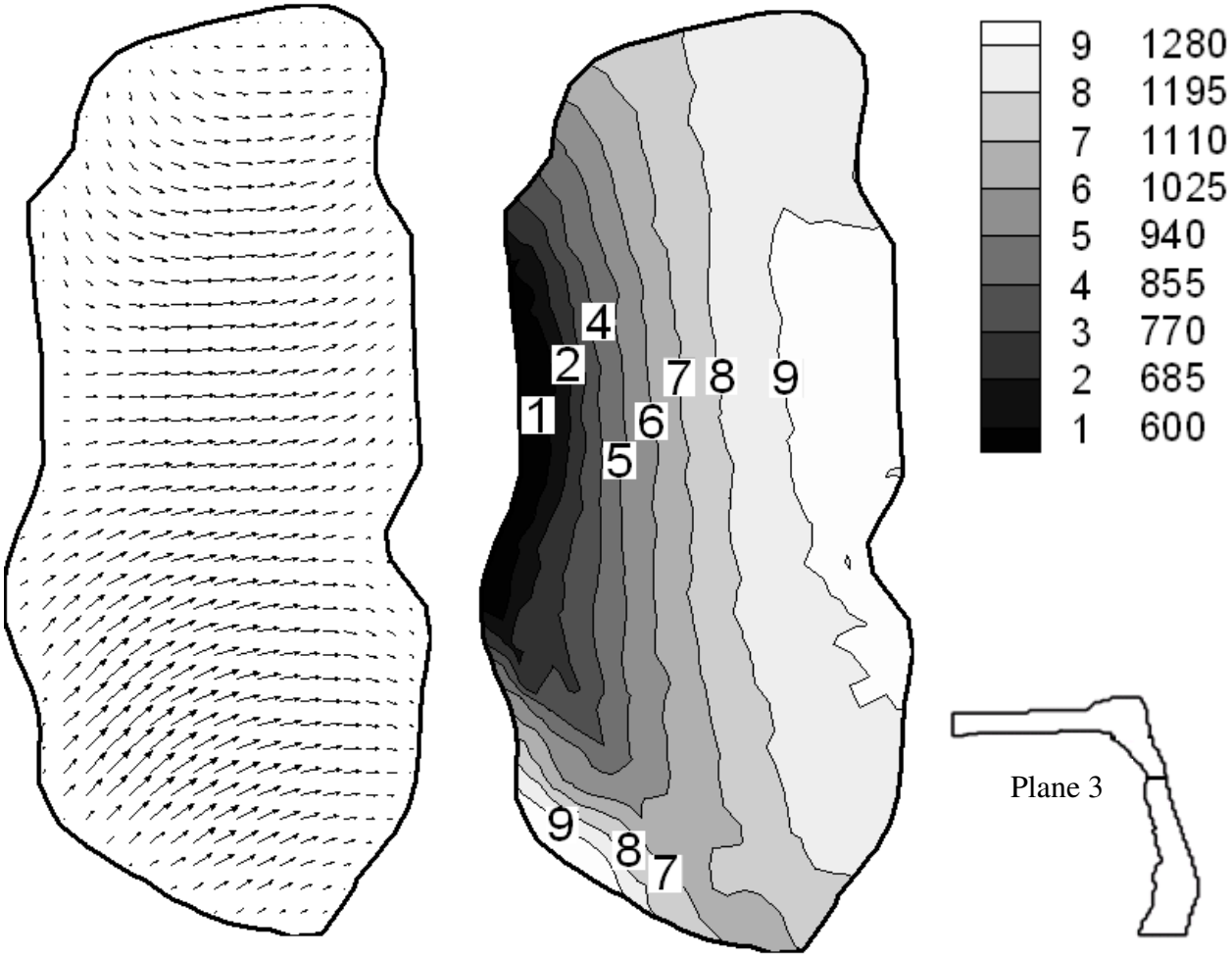
9 1280
8 1195
7 1110
6 1025
5 940
4 855
3 770
2 685
1 600
4
2
1
6
5
7 8 9
9 8 7
Plane 3

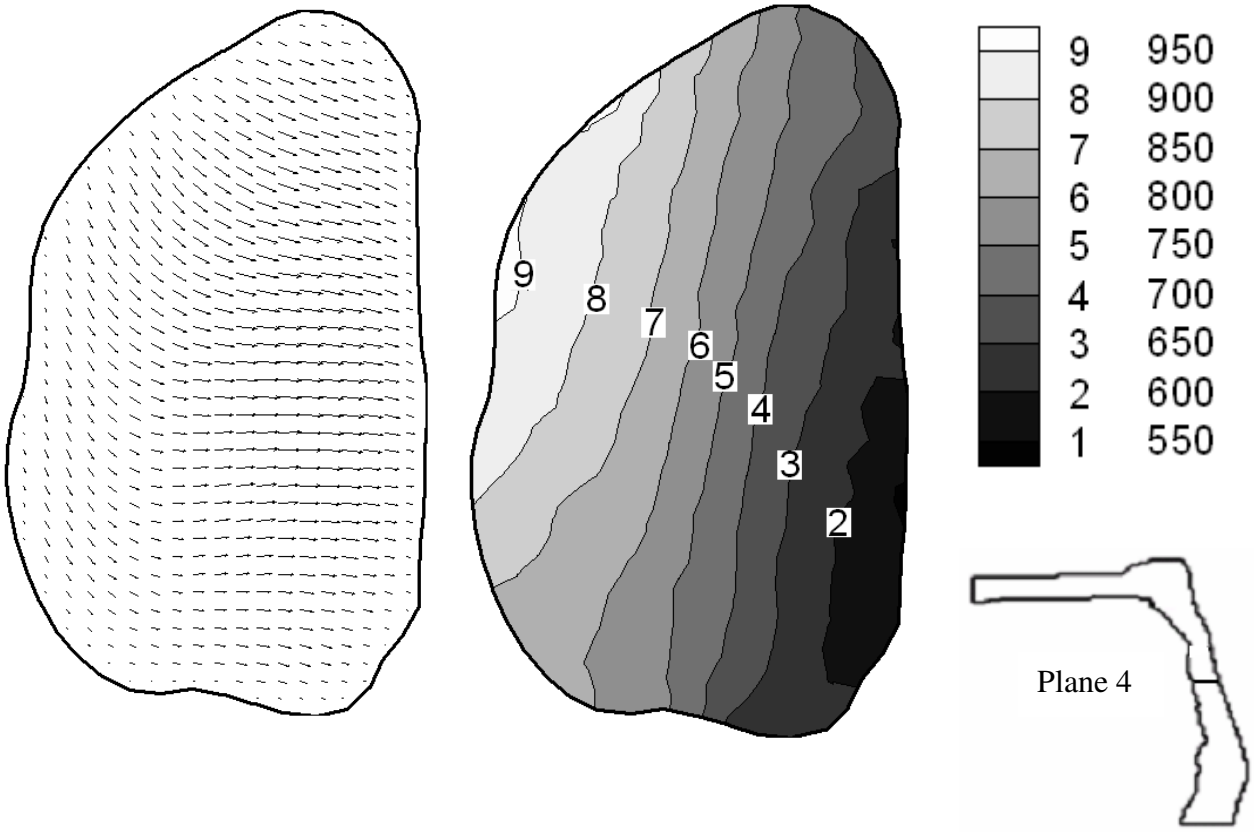

(b)

Fig. 6.3 Predicted secondary velocity vectors and pressure contour at plane 3 and plane 4.

The mean centerline-velocity fields in the 90^{o} nasopharynx bend, pharynx model under normal tidal aspiratory condition at low inhalation activity (1 m/s) are shown in Fig. 6.3. Different cross-sectional views of the airflows around the pharynx regions indicated by planes 3 – 6 in Fig. 6.3 represent the axial velocity contours as well as the secondary flow velocity vectors. The main characteristics of the depicted axial flow fields can be described by the following two distinct observations: (a) the velocity profiles became skewed in the curved portion of the pharynx due to centrifugal force effects and (b) flow separation occurred with abrupt geometrical changes – the variation cross-sectional area in the pharynx region after the soft palate. Because of the

centrifugally induced pressure gradient, the secondary motion of the fluid persisted when the airflow turned the bend from the nose to the pharynx. The intensity of the secondary flows was strong as demonstrated in two curved regions (Planes 3 and 4) and the curved region (Planes 5 and 6).

Figure 6.4 illustrates the centerline-velocity profiles in the throat for the cases of low inhalation (1 m/s) and high inhalation (10 m/s) activities that are within the range of normal breathing condition. Albeit the differences in the velocity magnitudes, the trends of the velocity profiles recorded for the two activities were rather similar with the highest velocities achieved at Planes 3 and 4 of the pharynx region. These results demonstrated the independence of the velocity profiles on the inlet velocities; scaling of the velocities may be permissible for different range of inlet velocities. The maximum velocities recorded for either the two inhalation activities were almost 5 times higher than the inlet velocities indicating an acceleration of the airflow as it passed through the constricted areas of the pharynx region.

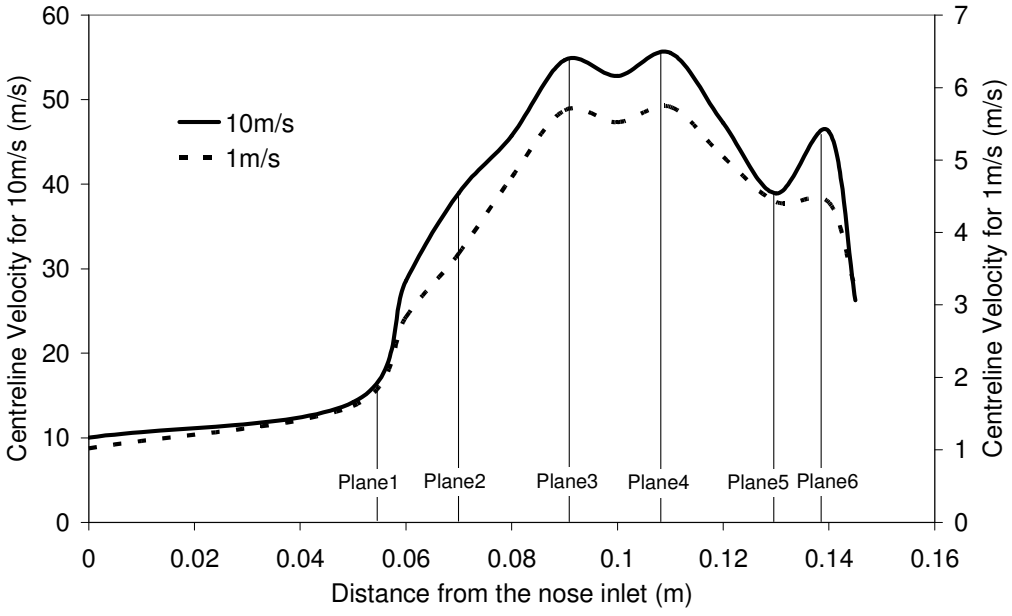

Fig. 6.4 Centerline velocity profile for inlet velocity at 1m/s and 10m/s

6.1.3 Turbulent kinetic energy

The variation of cross-sectional area-averaged turbulence kinetic energy as a function of the axial distance from the nose inlet is shown in Fig. 6.5. Substantial turbulence kinetic energy is generated with maximum values of 0.25 m^2/s^2 and 10 m^2/s^2 located activities at planes 3 and 4 of the pharynx region. Regardless of either low or high inhalation activity, the turbulence kinetic energy increased dramatically after leaving Plane 1, around the 90^o nasopharynx bend. It decreased from the maximum values as the flow of air traveled past the pharynx and increased again between Planes 5 and 6. Thereafter, the results showed a significant drop of the turbulent kinetic energy as it continued downstream towards the trachea. The turbulence kinetic energy profiles were observed to be rather similar to those of the velocity profiles in Fig. 6.4.

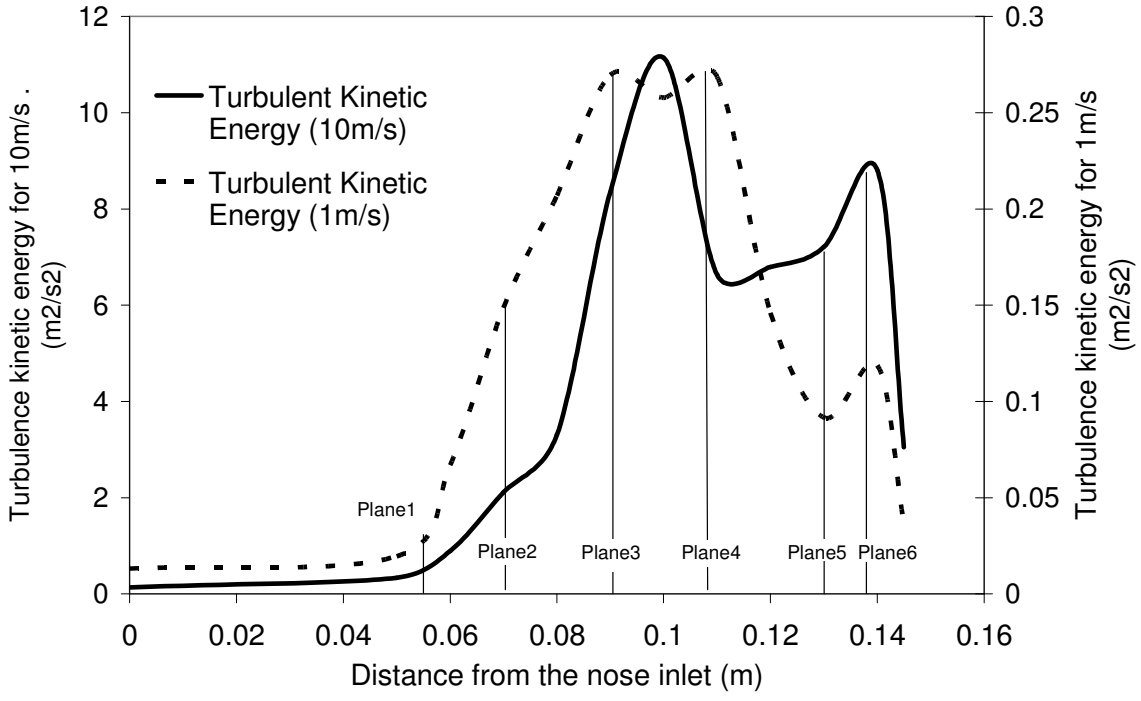

Fig. 6.5 Centerline turbulence kinetic energy profile for inlet velocity at 1m/s and 10m/s

6.1.4 Wall shear stress

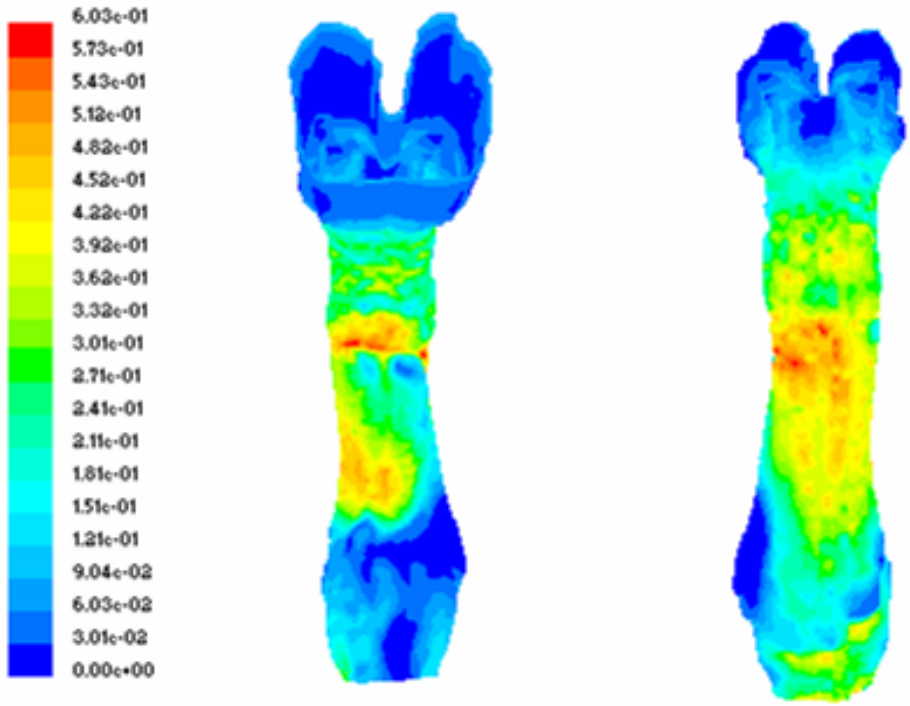

Fig. 6.6 Contours of wall shear stress: front view from inlet (Left), back view (Right)

The spatial Wall Shear Stress (WSS) values are shown in filled contours in Fig. 6.6 for the front and back view of the airway. These contours show only the WSS magnitude and not its spatial direction. WWS is determined from velocity gradients. Any non-zero value of the WSS denotes a non-uniform aerodynamic environment. The results indicate that high curvature affects the velocity distribution in planes 3-6 as seen from results above giving rise to high WSS values. Beyond these locations, low WSS values persist especially near the 90^{o} nasopharynx bend. The shear stress profiles calculated around the circumference wall of planes 3 and 4 are shown in Figs. 6.7 and 6.8 respectively. The circumferential direction is clockwise looking from the throat towards the flow inlet. As observed, there are substantial circumferential variations of the wall shear stress with the presence of peaks and valleys.

At plane 3, the WSS demonstrated a sharp peak at 10 Pa for an inlet velocity of 10 m/s while a maximum value of 0.5 Pa was achieved for an inlet velocity of 1 m/s. The predictions indicated that the maximum WSS occurred at the same location of a circumferential angle of 180^{o} regardless of any breathing situations. At the circumferential angle of 90^{o}, the WSS also revealed high stress levels but marginally lower from those experienced at the angle of 180^{o}. Similar maximum magnitudes and behaviors were also observed at plane 4 in Fig. 6.8 at the circumferential angles of 90^{o} and 180^{o} albeit the absence of a marked dip of the WSS profiles between the angles of 90^{o} and 180^{o} as portrayed in plane 3.

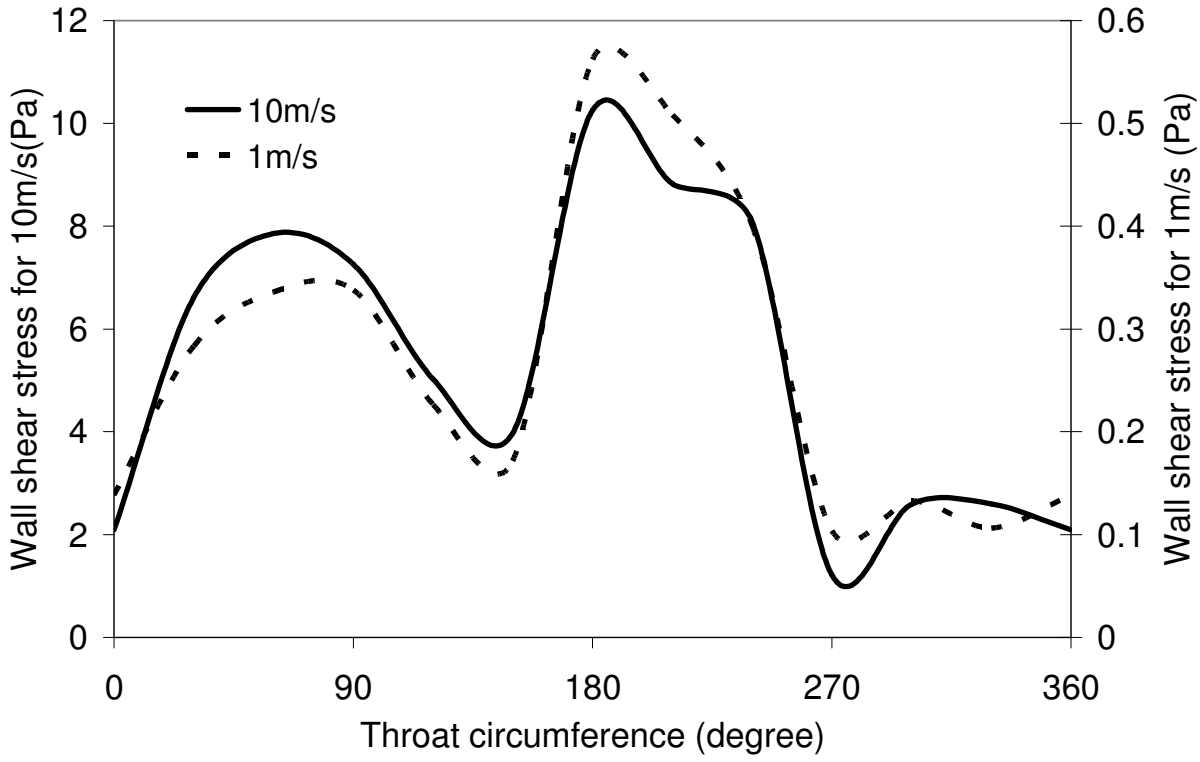

Fig. 6.7 Wall shear stress in Plane 3 for inlet velocity at 1m/s and 10m/s

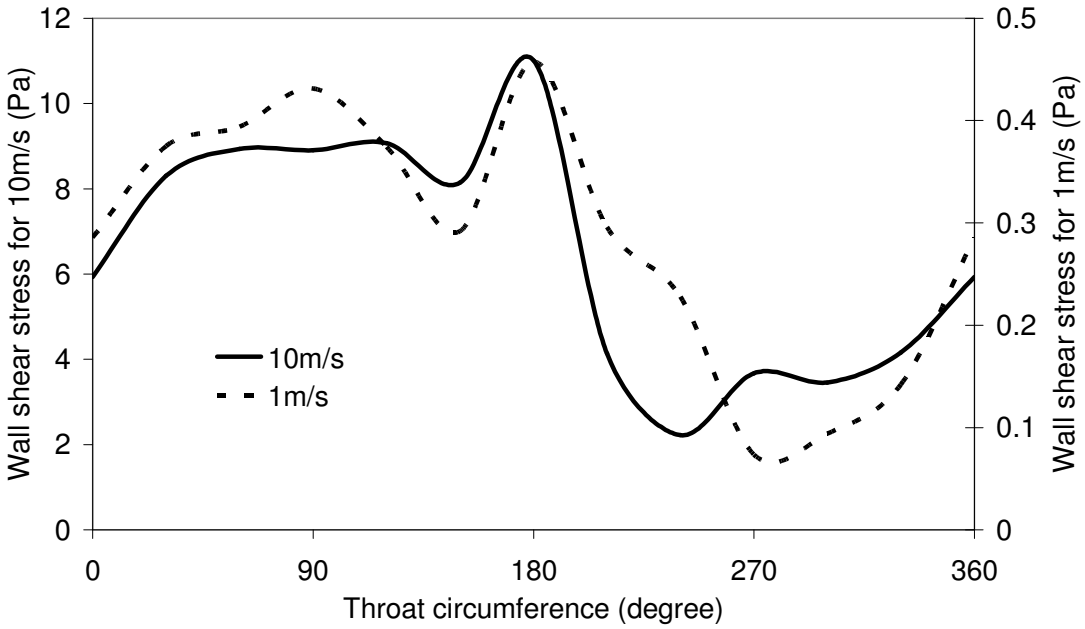

Fig. 6.8 Wall shear stress in Plane 4 for inlet velocity at 1m/s and 10m/s

The axially distributed average and maximum WSS profiles from the nose inlet to the trachea are presented in Fig. 6.9. The average values of the WSS have been obtained by spatially averaging the predicted circumferential surface stresses at incremental locations along the throat airway geometry. Here again, the WSS profiles were observed to be rather similar to the respective velocity and turbulence kinetic energy profiles in Figs. 6.4 and 6.5. The dominantly high WSS concurred with the highest velocity and turbulent kinetic energy as the air passed through these constricted planes 3 and 4 region, and planes 5 and 6 region before flowing into the larynx. The distribution of these localized high WSS presents a strong case where they can cause surface lesions to the soft tissues surrounding the pharynx thereby exposing unwanted layers of sensitive and tender areas to possible infections. Thus, there is strong evidence that the erosion of these layers in the pharynx regions has possible correlation with head and neck cancer especially through heavy smoking. Malignant cells may develop through local inflammation of these regions. Frequent localizations of these surface

lesions may continue to exacerbate the problem by the possibility of reaching a severe carcinomas state if they are left untreated.

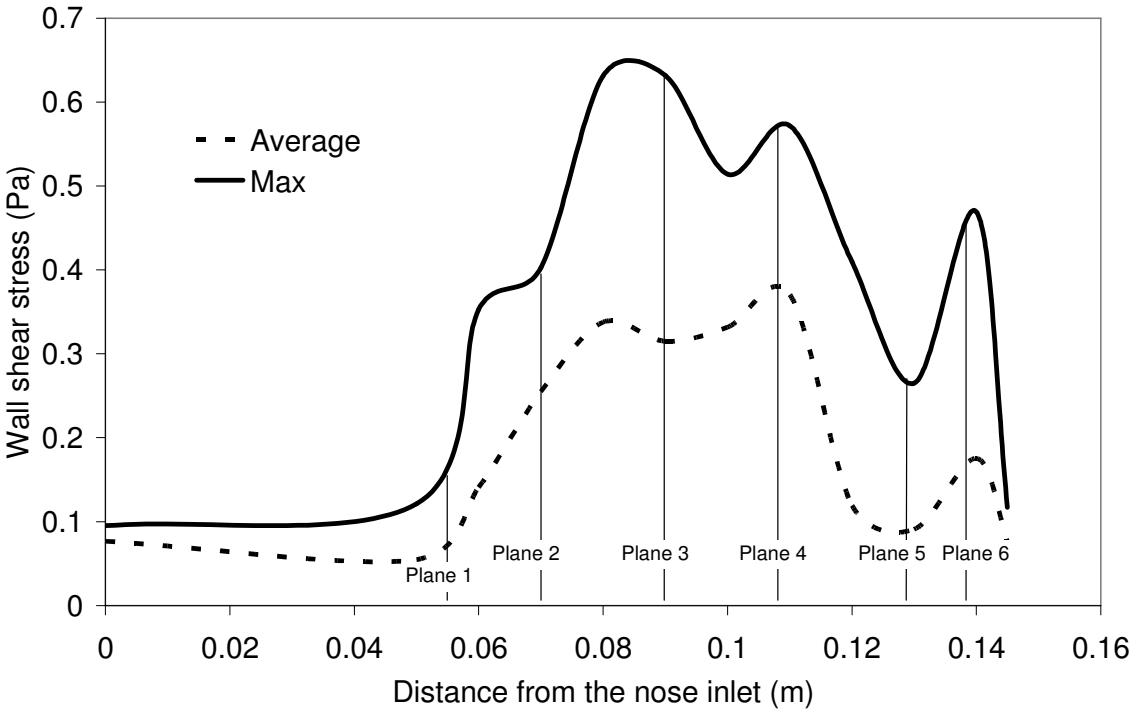

(a)

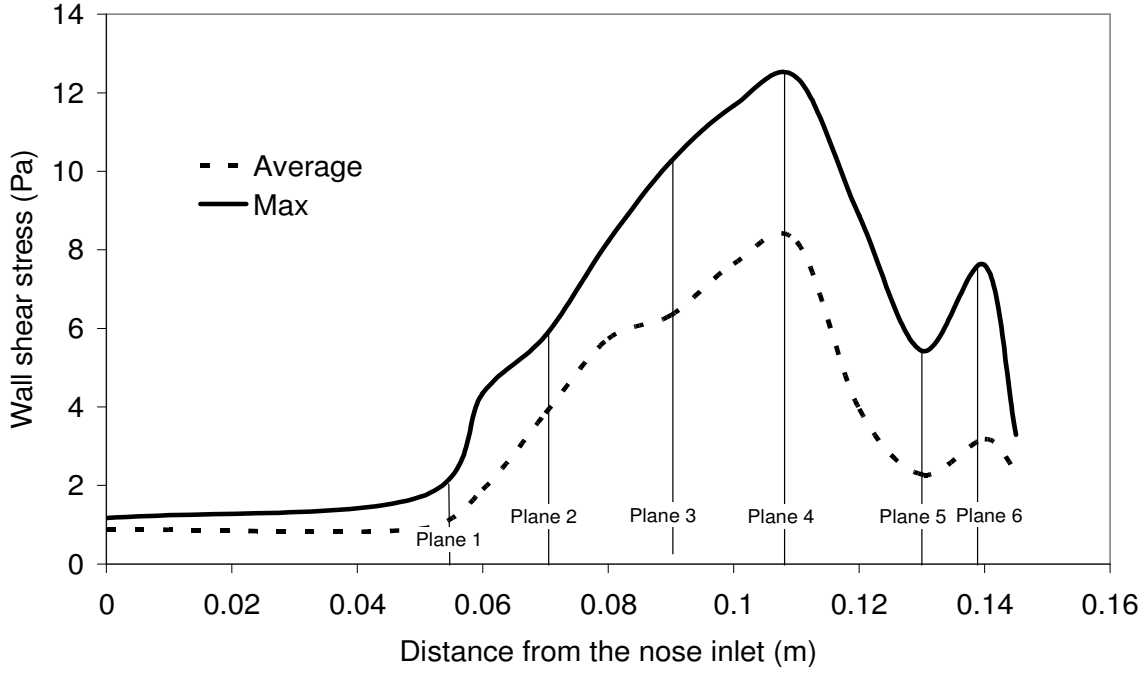

(b)

Fig. 6.9 Centerline wall shear stress profile for inlet velocity at (a) 1m/s and (b) 10m/s

6.1.5 Conclusion

The RSM turbulence model has shown to better capture the characteristics of strong secondary flow, anisotropy of shear stresses and curved streamline within the complex geometrical structure of realistic nasopharynx and pharynx airway generated by CT scan images. The flow patterns and velocity vectors obtained by Particle Image Velocimetry (PIV) was used to validate the RSM results. The results demonstrate that the RSM is capable of capturing the characteristics of complex flow patterns in human airway.

The topography of velocity, turbulent kinetic energy and WSS in the airway was predicted by RSM under normal breathing conditions. The RSM model revealed a substantial difference in both of the magnitude and spatial distribution of the velocity, turbulent kinetic energy and WSS values everywhere within the airway. This study particularly showed the existence of high WSS values that also concurred with high velocities and turbulent kinetic energy levels in the pharynx region. The presence of high WSS in the pharynx region are anatomic locations predisposed for possible lesion development. These lesions on the layers of soft tissues surrounding the pharynx region expose the surfaces to possible infection and inflammation especially for cases of heavy smoking, which can probably lead to the risk of contracting cancer because of the formation of malignant tumors. Results indicated that the dominant high WSS values can reach a maximum of 0.5 Pa and 10 Pa for low and high inhalation activities at the pharynx.

6.2 A realistic human nasal cavity

The nasal cavity was subjected to constant air flow rates of 20–40 L/min. The internal walls were modelled using an "enhanced wall treatment" function to consider the no-slip condition on the air flow. The particles adopted the properties of spherical water droplets, as most drug formulations are diluted with water. Initial particle conditions are assumed by analytical methods due to a lack of experimental data. The conditions for the release of particles into the constant flow rate differed for the parameter under investigation and are elucidated upon, within the relevant sections. The internal walls of the nasal cavity were set to a "trap" condition, meaning that particles touching a wall, deposit at that location.

A preliminary model was created with a mesh cell count of 82,000. This coarse mesh underwent enhancement techniques to address quality criteria such as cell skewness, y+ wall boundary conditions and cell-to-cell volume change. Three further models were created, each retaining the same geometry but differing in their mesh sizes (286,000 cells, 586,000 cells, and 822,000 cells) for computation to check for grid independency through convergence of results. Figure 6.10 shows the resolution of the original coarse mesh (82,000 cells) and compares it with the enhanced models. An additional frontal view (looking into subject's face) of a coronal section, close to the beginning of the turbinate region is included.

It is known that the accuracy of results increase for finer mesh, however at higher computational costs. A grid independence test, allows for the optimum mesh grid size to be determined. The Navier-Stokes equations for the gas phase were solved at 20 L/min and a velocity profile near the constricting nasal valve area was undertaken for each model and compared. Figure 6.11 shows the velocity profile converge at a

mesh resolution of 586,000 cells and a further increase to 822,000 cells shows no further improvement. Therefore the nasal cavity model with 586,000 cells is used for further analysis.

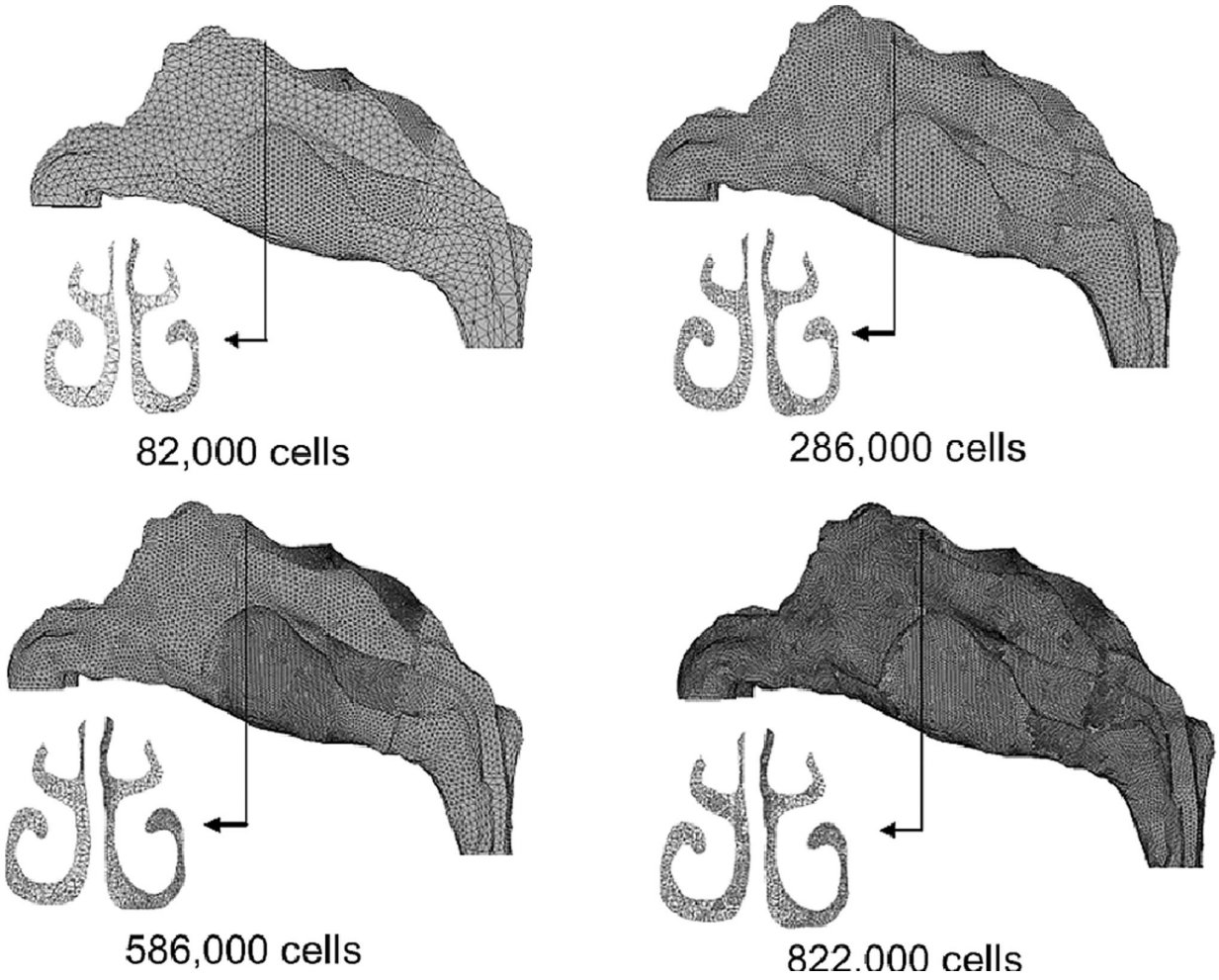

Fig. 6.10 Nasal cavity models of different mesh resolutions, 82,000, 286,000, 586,000 and 822,000 cells.

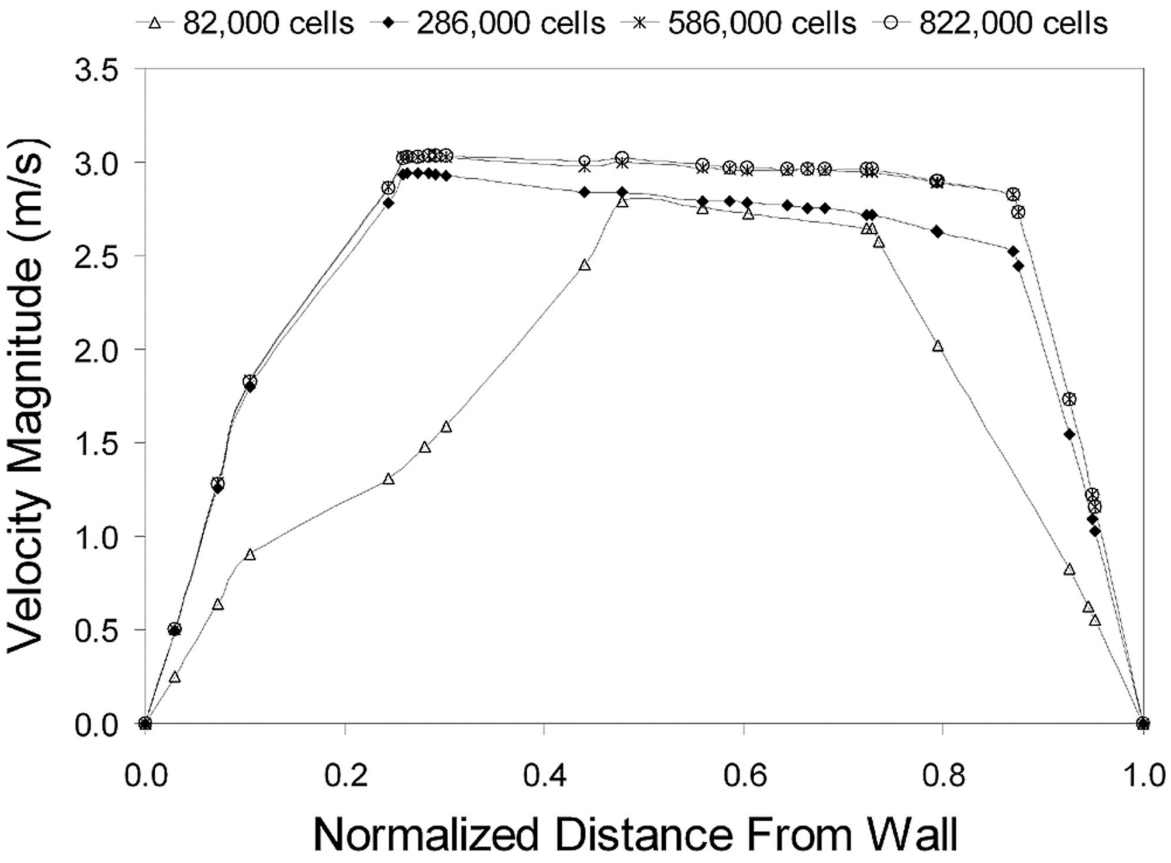

Fig. 6.11 Velocity profiles of a coronal section near the nasal valve region for the four different nasal cavity models. The profile is taken along the line shown on the coronal section.

6.2.1 Validation using a Hybrid Method

Monodispersed particles in the range of 1 μm to 30 μm were initially tested at gas flow rates, 20 L/min and 40 L/min. Two tracking methods, DRW tracking and mean flow tracking were applied. The results found were qualitatively similar to that found in Zhang et al. (2004). The DRW tracking grossly overestimates particle deposition for $I < 10{,}000$ and underestimates deposition for $I > 20{,}000$, while the mean flow tracking overestimates particle deposition for $I < 8{,}000$ and underestimates deposition for $I > 10{,}000$. It is suggested that a hybrid tracking method be used where the DRW tracking is used for larger particles where $I > 10{,}000$ and a mean flow tracking be used for $I < 10{,}000$, equivalent to $dp \approx 5.5$ μm for a flow rate of 20 L/min.

Thus further analysis of deposition of particles will focus on particles in the range of 10–50 μm. This ideal model is sufficient for the study of nasal spray particles given that its mean particle sizes are in the range of 50–70 μm (Cheng et al. 2001).

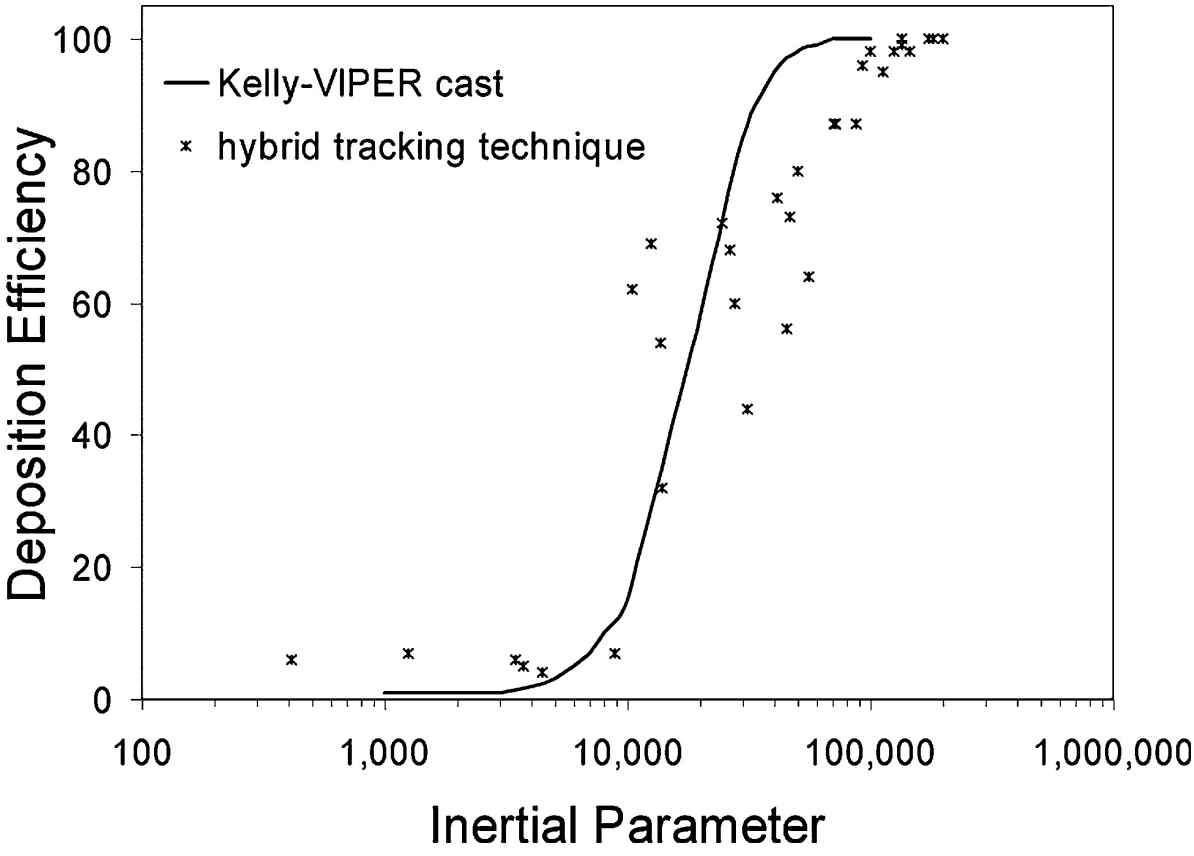

Fig. 6.12 Deposition efficiency for monodisperse particles released passively from the nostril inlet subjected to airflow rates of 20 L/min, 30 L/min and 40 L/min using a hybrid tracking technique.

The results were compared against Kelly et al. (2004) experimental results (Fig. 6.12). The numerical hybrid tracking simulation overestimated deposition for $I >$ 10,000 and underpredicted deposition for $I <$ 10,000. One reason for the discrepancy is the intersubject variability between the nasal cavity models that Kelly et al. (2004) obtained (53-year-old, non-smoking Caucasian male, 73 kg mass, 173 cm height) as opposed to the model used in the present study. Differences in the comparison of particle deposition efficiencies with the inertial parameter is discussed by Haußermann

et al. (2002), such as the limitation of the inertial parameter not taking into account the changes in airway geometry. This constant air flow rate is a measure of the average impactability of the particle over the entire domain, as it doesn't factor in the changes in velocity which is significant when the geometry under consideration is highly convoluted, narrow and complex. Furthermore, nasal cavity replicate casts with wider airways as in Swift's (1991) case might cause less deposition due to secondary flow (Haußermann et al. 2002). This provides some reasoning for variations in data for deposition efficiency versus inertial parameter charts. In addition Haußermann et al.'s (2002) study showed that a lower flow rate (i.e., 10 L/min) had lower deposition efficiencies than a higher flow rate (i.e., 20 L/min) for the same inertial parameter.

6.2.2 Air Flow Analysis

A lot of literature has covered air flow patterns within the nasal cavity, Zwartz and Guilmette (2001), and Horschler et al. (2003), to name a few, thus a comprehensive discussion will not be undertaken in the present study. The total air flow rate through both nostrils was 20 L/min which produced an inlet velocity u_{in} = 2.1 m/s. The flow increases at the nasal valve where the cross-sectional area is smallest and reaches a maximum area averaged velocity of 2.28 m/s (Fig. 6.13a, b, c). Entering the atrium, the velocity decreases as the nasal cavity opens up. The flow remains along the middle and lower regions of the nasal cavity and close to the septum walls rather than diverging out towards the outer meatus. A region of recirculation appears in the expanding region of the cavity near the top (olfactory region). At the nasal pharynx the velocity increases once more where a decrease in area exists.

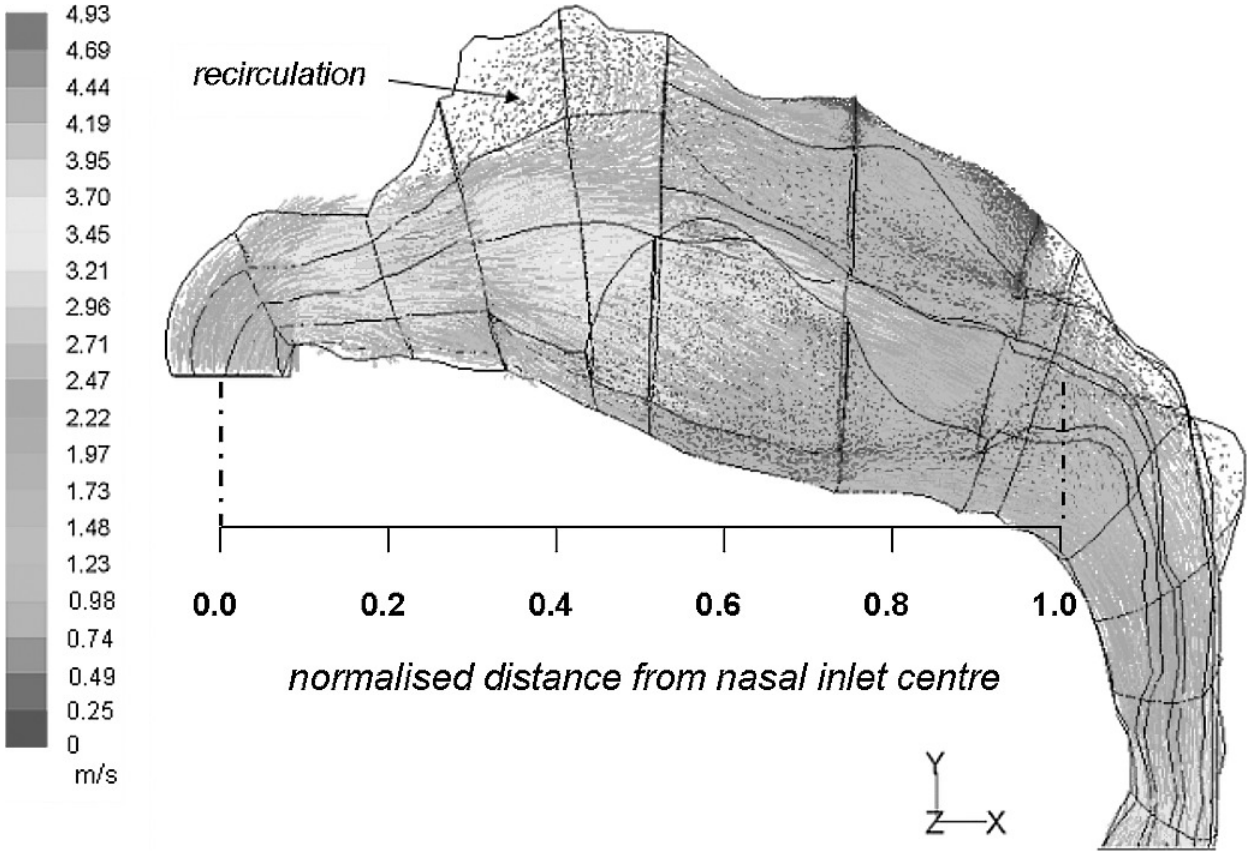
4.93
4.69
4.44
4.19
3.95
3.70
3.45
3.21
2.96
2.71
2.47
2.22
1.97
1.73
1.48
1.23
0.98
0.74
0.49
0.25
0
m/s
recirculation
0.0
0.2
0.4
0.6
0.8
1.0
normalised distance from nasal inlet centre
Y
Z
X

(a)

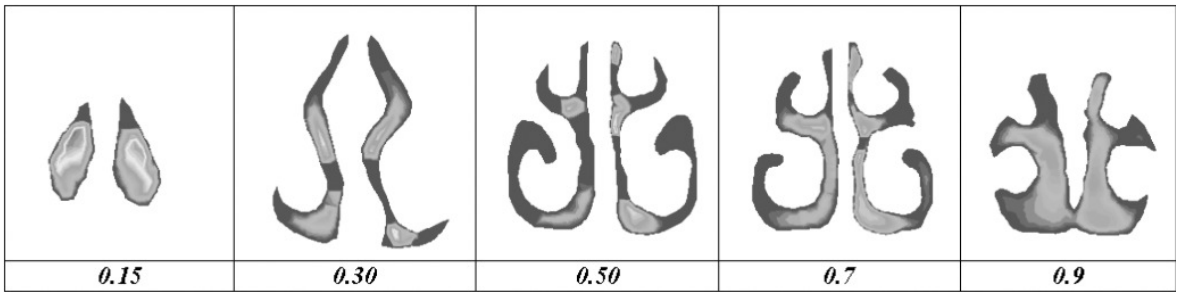
0.15
0.30
0.50
0.7
0.9

(b)

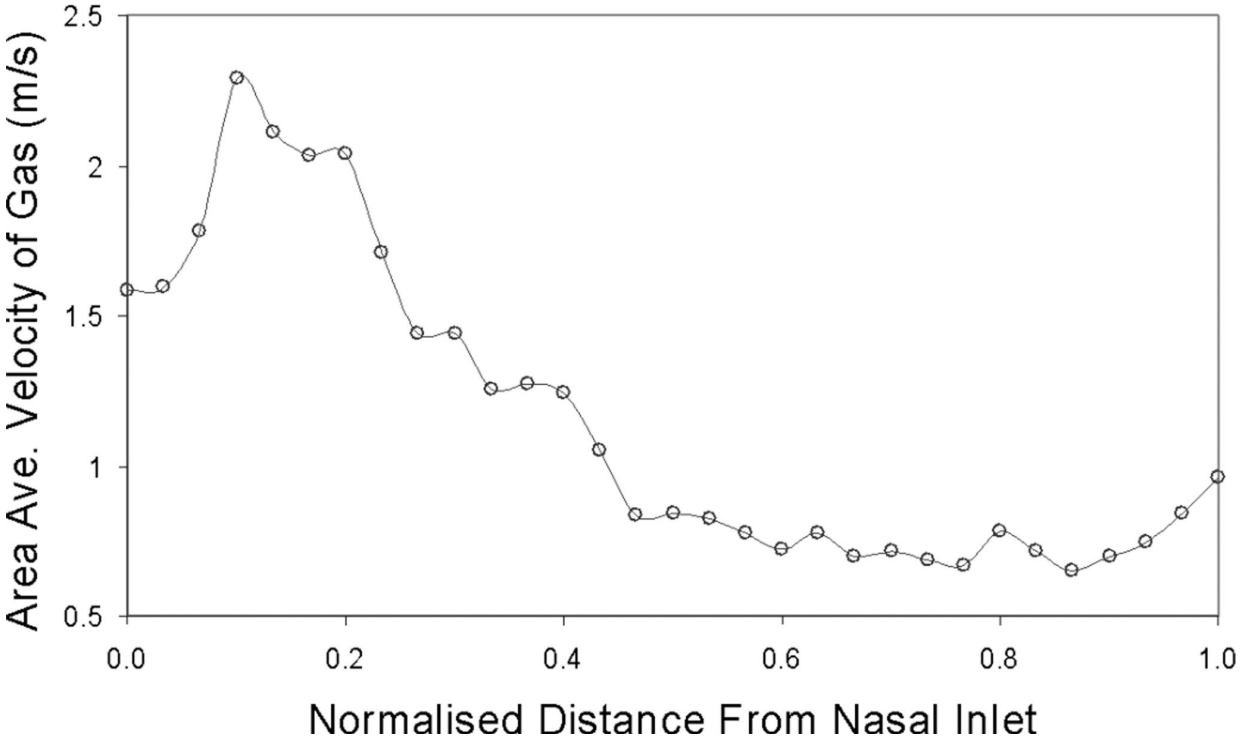

(c)

Fig. 6.13 (a) A velocity vector field in the horizontal plane for inlet flowrate of 20 L/min. A region of recirculation is found near the roof of the nasal cavity. The normalised distance spans from the average center of the two nostril openings in the x-axis, to the nasopharynx where the two cavities have joined completely. (b) Velocity contours at different cross-sections through the cavity. The cross-sections correspond to the normalised distance from the nasal inlet. (c) Area averaged velocity profile inside the nasal passage. Maximum averaged area occurs around 0.10–0.15, near the nasal valve region. An increase in the velocity occurs at the nasopharynx region where the cross-sectional area decreases.

6.2.3 Initial Particle Velocity

The initial particle velocity can be controlled in many ways such as changing the nozzle diameter and the actuation echanism. Monodispersed particles were released uniformly in a normal direction to the inlet surface of each nostril and the average deposition within the left and right nasal cavity was recorded. Injected particle velocities were calculated based on mass conservation, assumed nasal spray geometries and our own preliminary experimental work on nasal spray nozzles, which found velocities ranging between 10 m/s to 20 m/s for 200 kpa to 500 kpa pressure actuations,

respectively. Quantitatively, the results obtained by using a uniform surface injection, normal to the nostril inlets, will differ from a real nasal spray application that possesses an injection from a very small diameter. However it does provide a basis for the impactability of specific particles at different injection velocities on a qualitative level. The injected particles have an increase in their kinetic energy, resulting in a higher initial momentum for the intended trajectory. However this energy is degenerated by the drag force acted on by the gas phase. The amount of influence the gas has on the particle is dependent on the particle Stokes number. Crowe et al. (1998) presents a relationship for the particle-gas velocity ratio as a function of the Stokes number:

$$u^* = \frac{u_p}{u_g} \approx \frac{1}{1+S_t} \tag{6-2}$$

where

$$S_t = \frac{\rho_p d_p^2}{18\mu_g}\frac{U}{D} = \tau\frac{U}{D} \tag{6-3}$$

which suggests that for small Stokes numbers (i.e., St → 0), the particle velocity approaches the gas phase velocity quickly. Large Stokes numbers (i.e., St → ∞) suggests that *u** approaches zero. This means that the particle velocity is unaffected by the gas. It is expected that the dynamic change in the particle velocity will occur within the anterior section of the nasal cavity given the order of magnitudes of the particles. The anterior third of the nasal cavity is divided into three zones and particle low visualization and deposition patterns within this region are observed with results displayed in Fig. 6.14b and Fig 6.15a, b, and c.

The front three zones are shown in Fig. 6.14a, where they conform to that of a 90 degree bend. Zone1 is similar to a vertical column; Zone2 is where the particles

begin to change its velocity with the gas phase whilst Zone3 will indicate those particles that were able to follow the gas phase. Figure 6.14b shows the total particle deposition in the first two zones of the nasal cavity at different particle injection velocities. A small influence on the impactability of a 10 μm particle is observed when there is an increase in the initial particle velocity and is seen by the slight increase in deposition. The low Stokes number brings about a rapid decrease in velocity and the particle assumes the gas phase velocity before the change in direction of the flow. The influence of $u*$ amplifies as the particle size increases, where a large proportion of particles deposit more readily in the two frontal zones.

About 70% of 15 μm particles are able to follow the curved streamlines when $u* = 1$ as particle impactablility is dominated by the Stokes number. However significant deposition increases when $u* > 4$. The Stokes number, a ratio of the particle's relaxation time to the flow characteristic time, indicates how long it takes for the particle to adjust to the gas phase conditions. For a fixed distance (nostril opening to the top of the vestibule), an increase in $u*$ will decrease the time taken to cover this distance. This leads to a shorter time and distance for the particle to adapt to the gas phase conditions and presents a higher impactability than that calculated by the Stokes number alone. The influence of the injected particle velocity is still felt as the gas phase begins to curve. As particle size increases, so does the relaxation time that the particle needs to adapt to flow changes. As a result significant deposition increases occur at lower $u*$ values for larger Stokes numbers. The larger particles exhibit much higher Stokes numbers which prevents the particles from following the curved streamlines. It is observed that 50 μm particles entrained in the flow ($u* = 1$) is an example of this.

Therefore an injected 50 μm particle (u^* = 10) exhibiting a greater amount of initial momentum will only exacerbate the linear projectile motion of the particle. Thus it is evident that there are two forces acting against each other during the initial injection of the particles. The initial momentum force that is counteracted by the drag force which is inversely proportional to the particle Stokes number. Figure 6.15a, b, c displays the deposition sites for the two extreme cases, dp = 10 μm and dp = 50 μm and a mid-range particle, dp = 15 μm subjected to u^* = 1 and u^* = 10. 50 μm particles impact at the top of the vestibule at u^* = 10, and at u^* = 1, only a small proportion begin to curve albeit for a short distance before impaction. In contrast 10 μm particles are barely affected by the increase in injection velocity with local deposition sites being concentrated near the nasal valve region and septum walls which is a qualitatively similar to Zwartz and Guilmette (2001). The difference in deposition occurs at the entrance region where entrained particles released near the wall deposit readily through fluctuations in the flow whereas particles at higher velocities overcome this region. The particle flow for u^* = 10 enable the particles to travel further linearly which is evident in the particles adapting to the flow changes at a later stage than particles at u^* = 1. This later adaptation to the flow causes the particles to assume those streamlines closer to the ceiling of the nasal cavity compared with particles at u^* = 1. Beyond the first two zones of the nasal cavity deposition sites are similar, locally. Deposition of 15 μm particles at u^* = 1 are mainly concentrated within the vestibule, nasal valve regions and along the septum walls. Differences appear between the left-side and right-side of the cavity which is due to anatomical variations. The concentration of particles within the middle passage of the nasal cavity is lighter than that shown in 10 μm particles as the larger

particles have a higher concentration within the anterior section of the nasal cavity. When $u*$ is increased to 10 the particle is no longer just governed by its Stokes number, but also by the driving force of the initial injected velocity that adds initial momentum to the particle. This increase in momentum is dissipated by the difference in velocities of the gas and particle phase. The particles travel further linearly, in the normal direction to the nostril inlet with 88% impacting at the top of the vestibule. Only 12% of particles are able to adjust to the curvature in time and these particles remain in the upper regions of the nasal cavity throughout the flow.

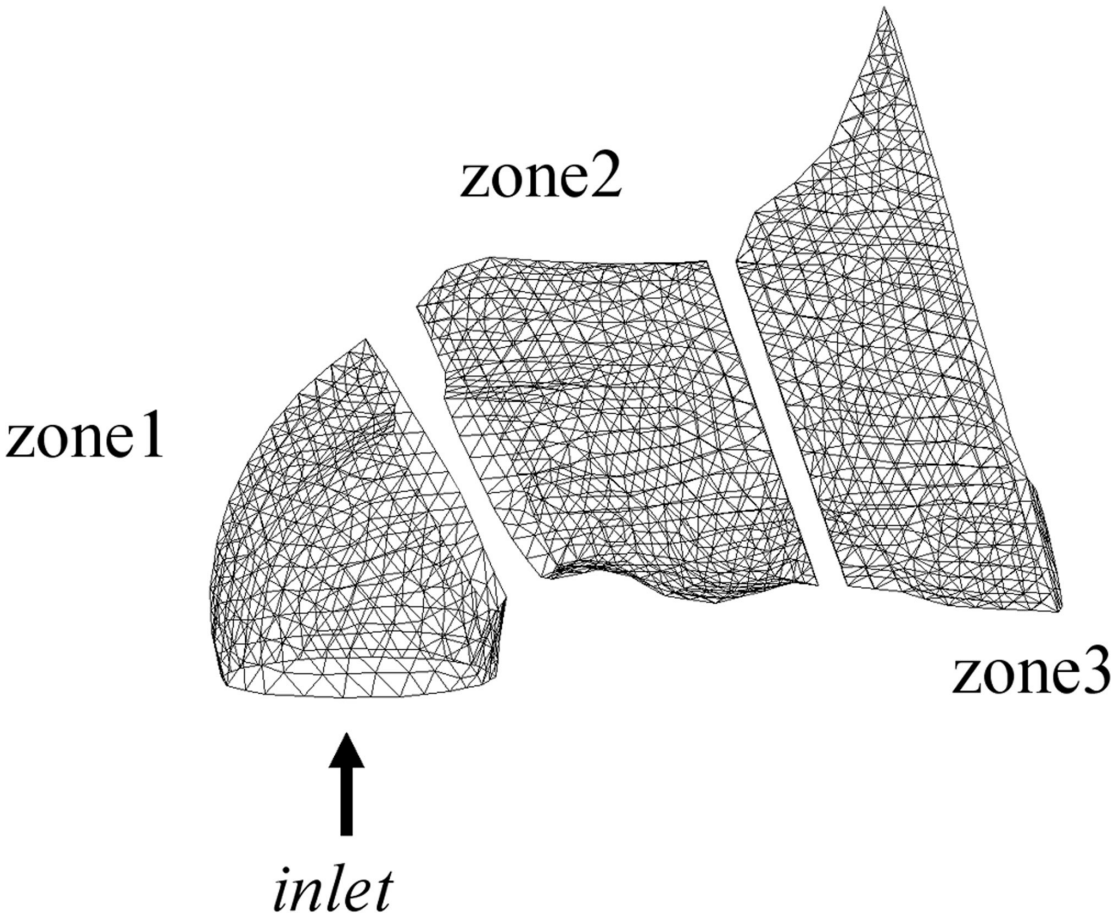

(a)

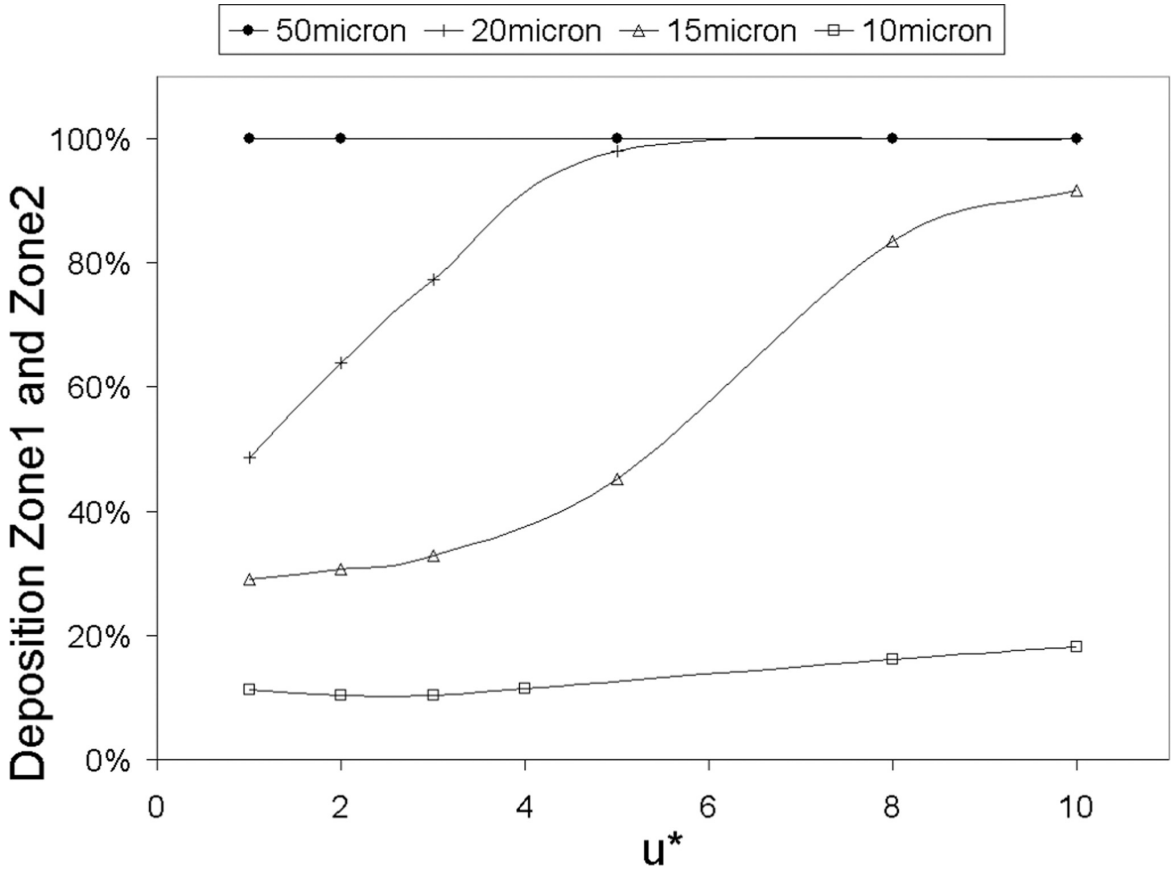

(b)

Fig. 6.14 (a) The anterior third of the nasal cavity that has been split into three zones for investigation. Zone 1 consists of the nostril inlet surface, zone 2 includes the nasal valve region and zone 3 is the beginning of the main nasal airway-the turbinate region. (b) Total deposition in zone 1 and zone 2 of the nasal cavity for different particle injection velocity. Particles were uniformly released from the nostril inlet surface, in the normal direction at different injected particle velocities, u*. Where $u* = u\ pi\ /ug$.

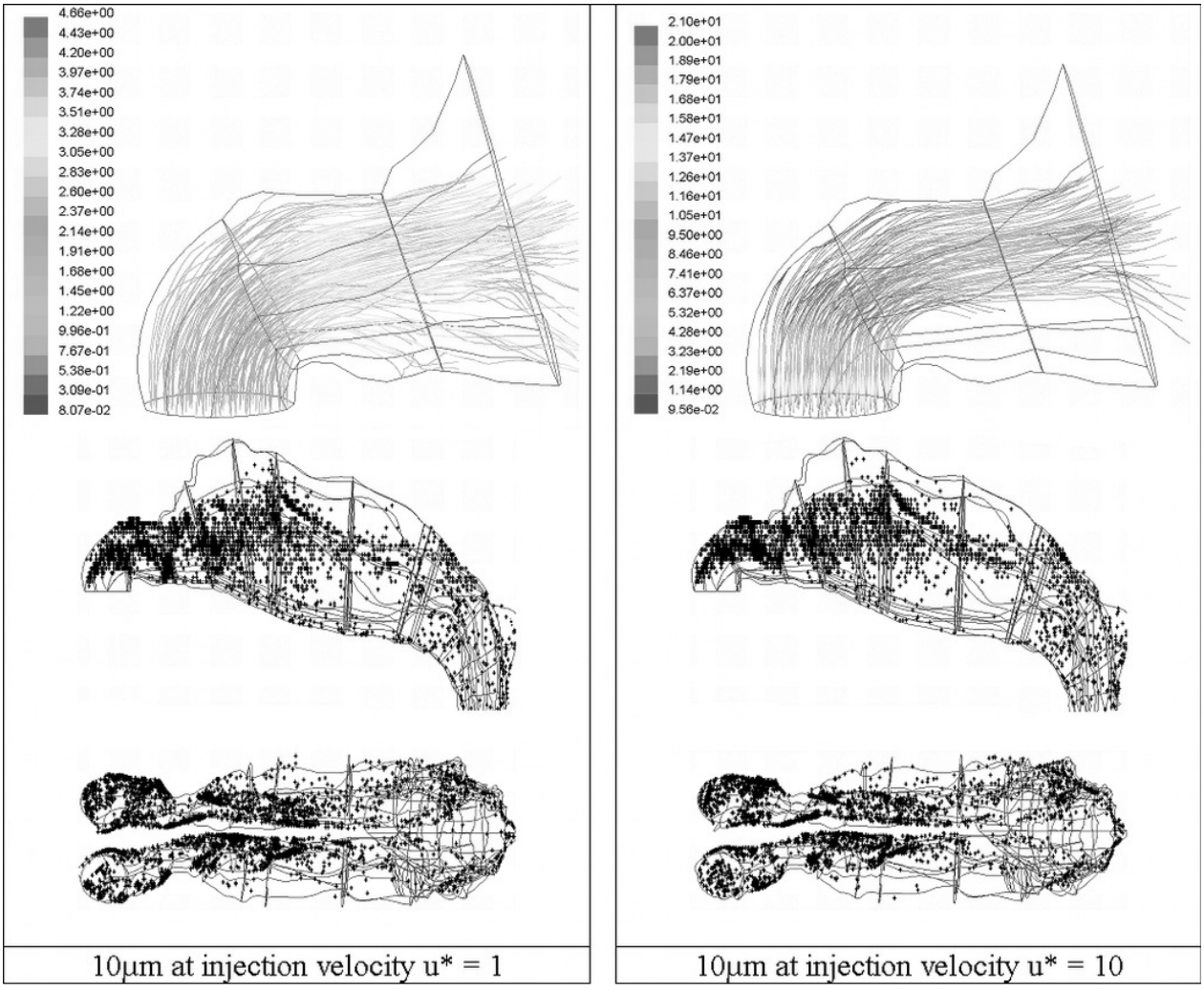
4.66e+00
4.43e+00
4.20e+00
3.97e+00
3.74e+00
3.51e+00
3.28e+00
3.05e+00
2.83e+00
2.60e+00
2.37e+00
2.14e+00
1.91e+00
1.68e+00
1.45e+00
1.22e+00
9.96e-01
7.67e-01
5.38e-01
3.09e-01
8.07e-02
10μm at injection velocity u* = 1
2.10e+01
2.00e+01
1.89e+01
1.79e+01
1.68e+01
1.58e+01
1.47e+01
1.37e+01
1.26e+01
1.16e+01
1.05e+01
9.50e+00
8.46e+00
7.41e+00
6.37e+00
5.32e+00
4.28e+00
3.23e+00
2.19e+00
1.14e+00
9.56e-02
10μm at injection velocity u* = 10

(a)

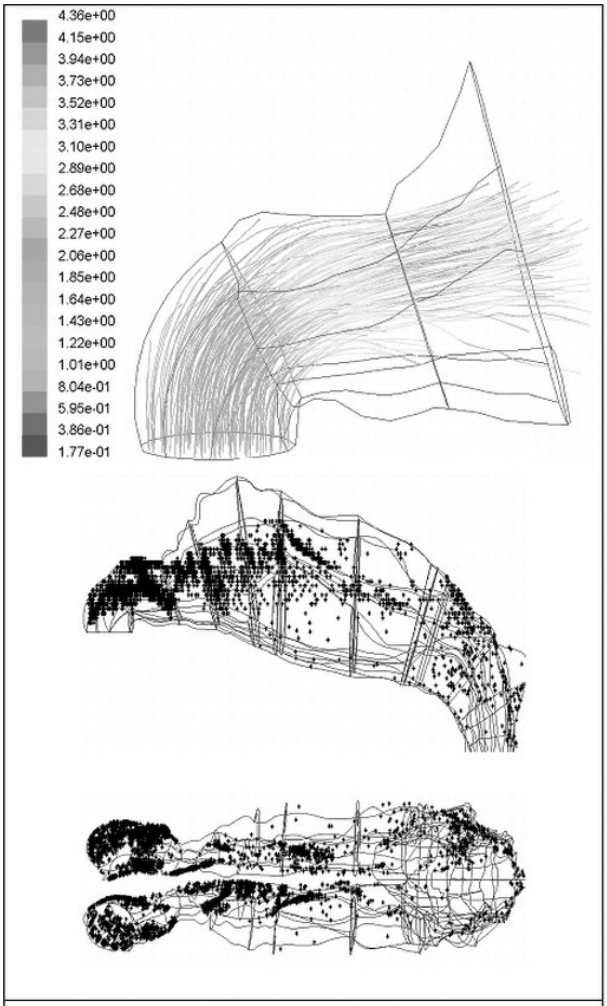

15μm at injection velocity u* = 1

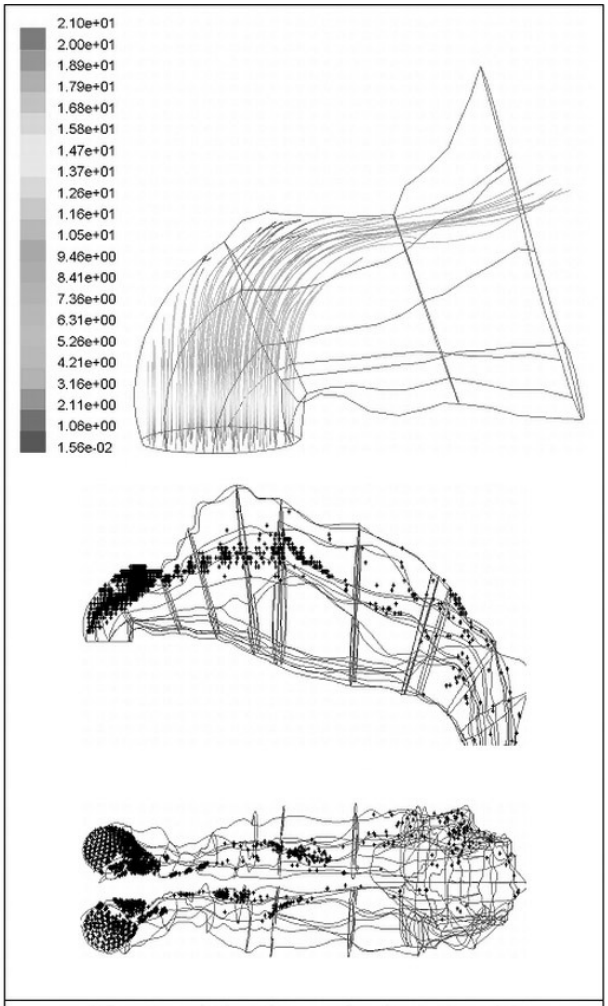

15μm at injection velocity u* = 10

(b)

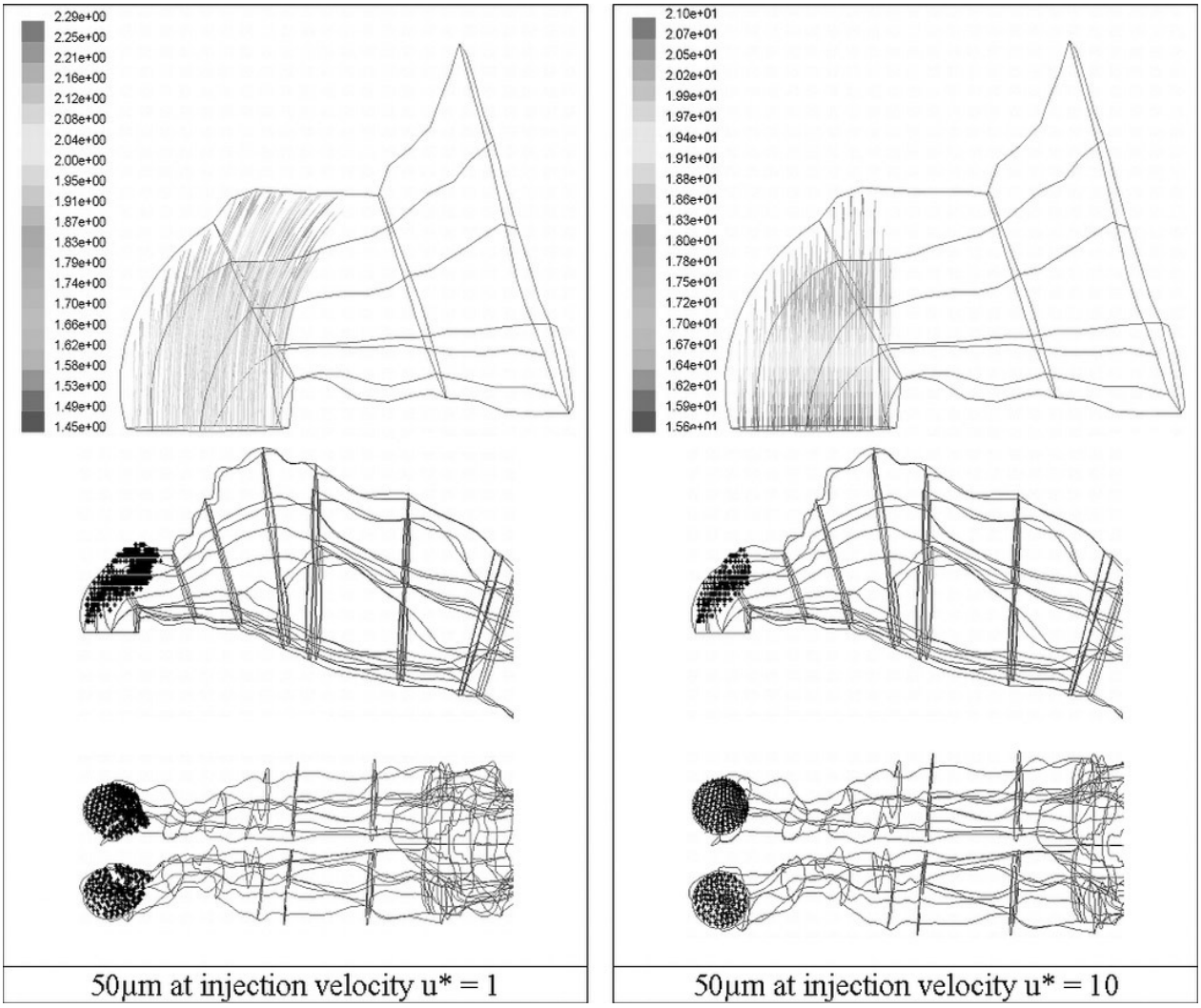

(c)

Fig. 6.15 (a) Deposition patterns for 10 μm particles released uniformly from the inlet surface normal to the nostril openings at $u^* = 1$ and $u^* = 10$. (b) Deposition patterns for 15 μm particles released uniformly from the inlet surface normal to the nostril openings at $u^* = 1$ and $u^* = 10$. (c) Deposition patterns for 50 μm particles released uniformly from the inlet surface normal to the nostril openings at $u^* = 1$ and $u^* = 10$.

6.3 Porous media

Given a brief overview of the research related to this study, it can be seen that no research has been carried out to consider the effect of the nasal hair on particle deposition. It was assumed by Hahn et. al. (1993) that the inclusions would not contribute to the difference in the particle deposition efficiency. But in nature, the main function of the nasal hair is to act as a filter for very small and very large particles (Mygind and Dahl, 1998). However the geometrical construction of nasal hair throughout the vestibule would be hypothetical as the distribution of nasal hairs varies from person to person. Another drawback is that it is time consuming and hence not feasible to simulate. Nevertheless, there is an alternate, simple, way of simulating the nasal hair, namely considering them a filtration medium.

Velocity variations and deposition of a series of mono-disperse aerosol injections in air for the nasal cavity and pharynx were numerically analysed at inspiration conditions. At normal breathing condition the volume fluxes were found to be 12 l/min with the Reynold's number based on the hydraulic diameter at the nostril. From the findings of the experimental study for the velocity distributions of 12 l/min, laminar flow was assumed. In analysing the results, it was deemed to be appropriate to present both qualitative and quantitative results through comprehensive parametric simulation conditions.

The geometry as shown in Fig. 6.16a was then discretized by the finite volume approach to obtain Fig. 6.16b. The mesh was refined from very coarse to fine until a better convergence was achieved. Figure 6.16c and d show the divided zones and sections of the model, which were used to predict the particle deposition and fluid-particle velocity.

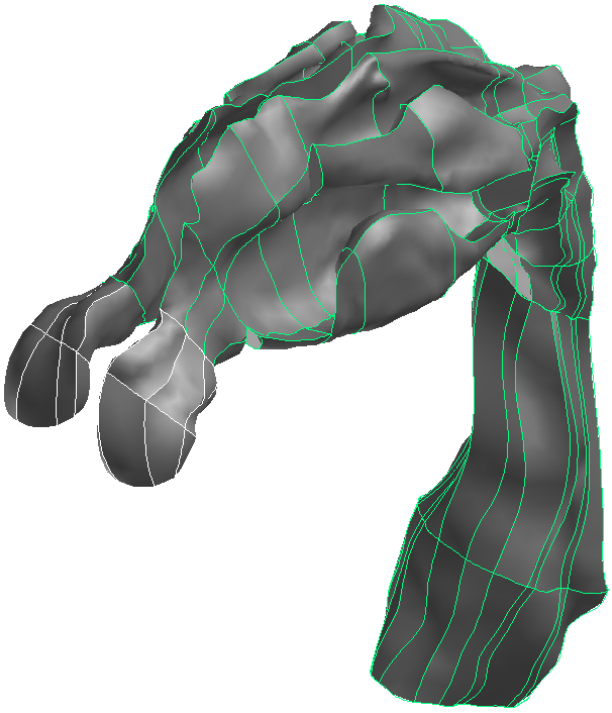

(a)

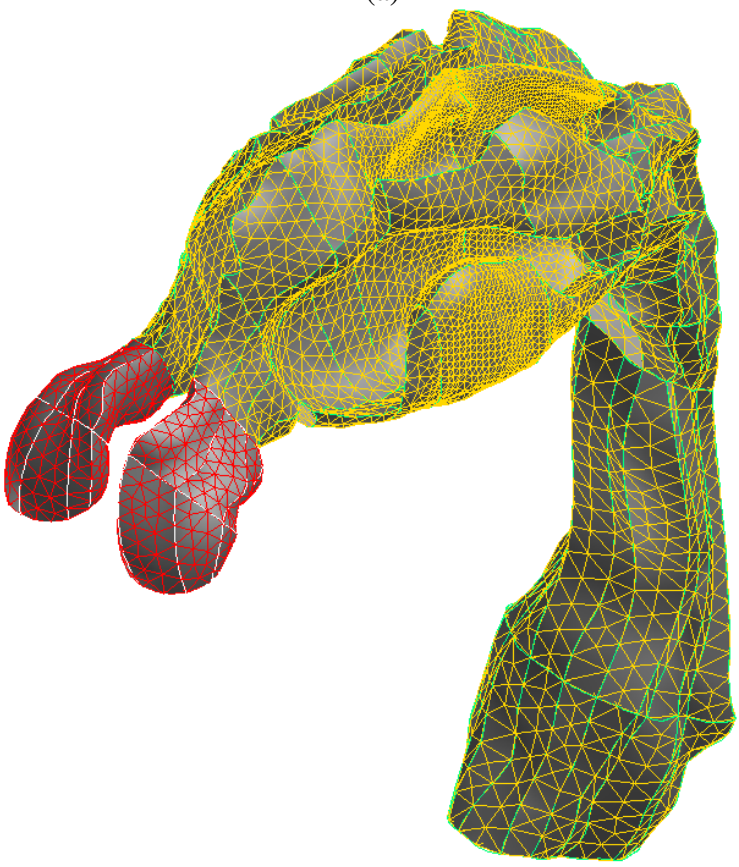

(b)

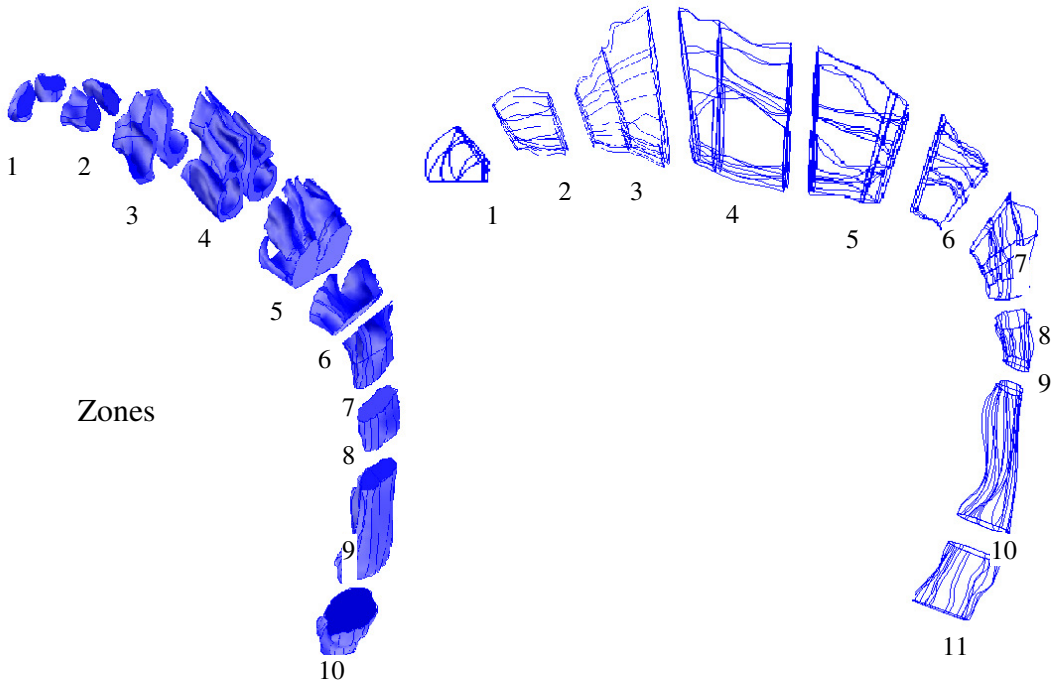

Fig. 6.16 (a) Geometry of the created nasal cavity and pharynx model, (b) Coarse mesh generated from the geometry, (c) Model split into 10 Zones, and (d) 11 Sections

6.3.1 Airflow patterns

Figure 6.17 shows a sample of the velocity vector of the x-y cross-sectional view of the nasal cavity and pharynx. Since this is a bifurcated model, the cross-section was taken along the mid-plane of the left nose and the mid-plane of the pharynx. Velocity distributions provide better visualisation of the direction of main stream and any recirculation caused by the secondary flow. In the case of laminar flow of 12 l/min for the non-porous region, the velocity vectors were found to have no recirculation zones. However, the incorporation of the porous model in the vestibule causes a recirculation on the superior turbinate region, thus causing a decrease in area averaged velocity at zone3 and zone4. This shows that the flow is more dominant in the top half

of the nasal cavity. A further decrease in porosity adds recirculation in the inferior turbinate as well as on the posterior region of the superior turbinate as shown in Fig. 6.17. These show that the flow is spread uniformly throughout the domain.

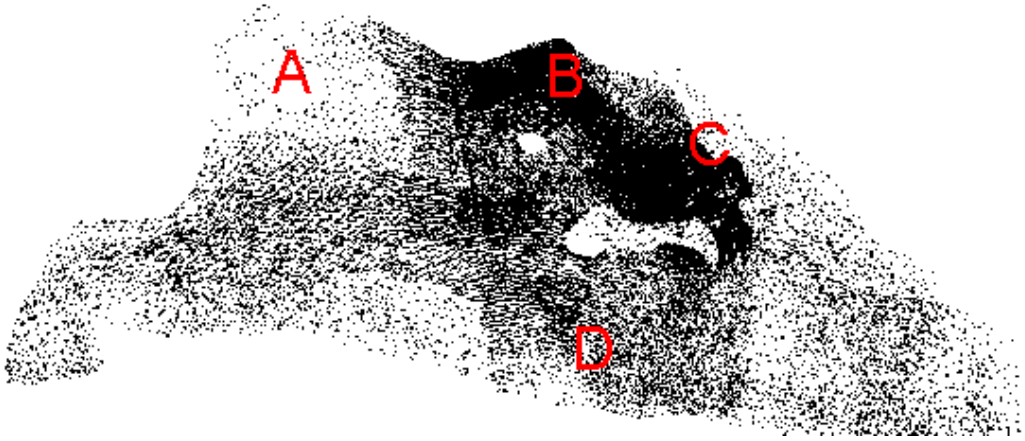

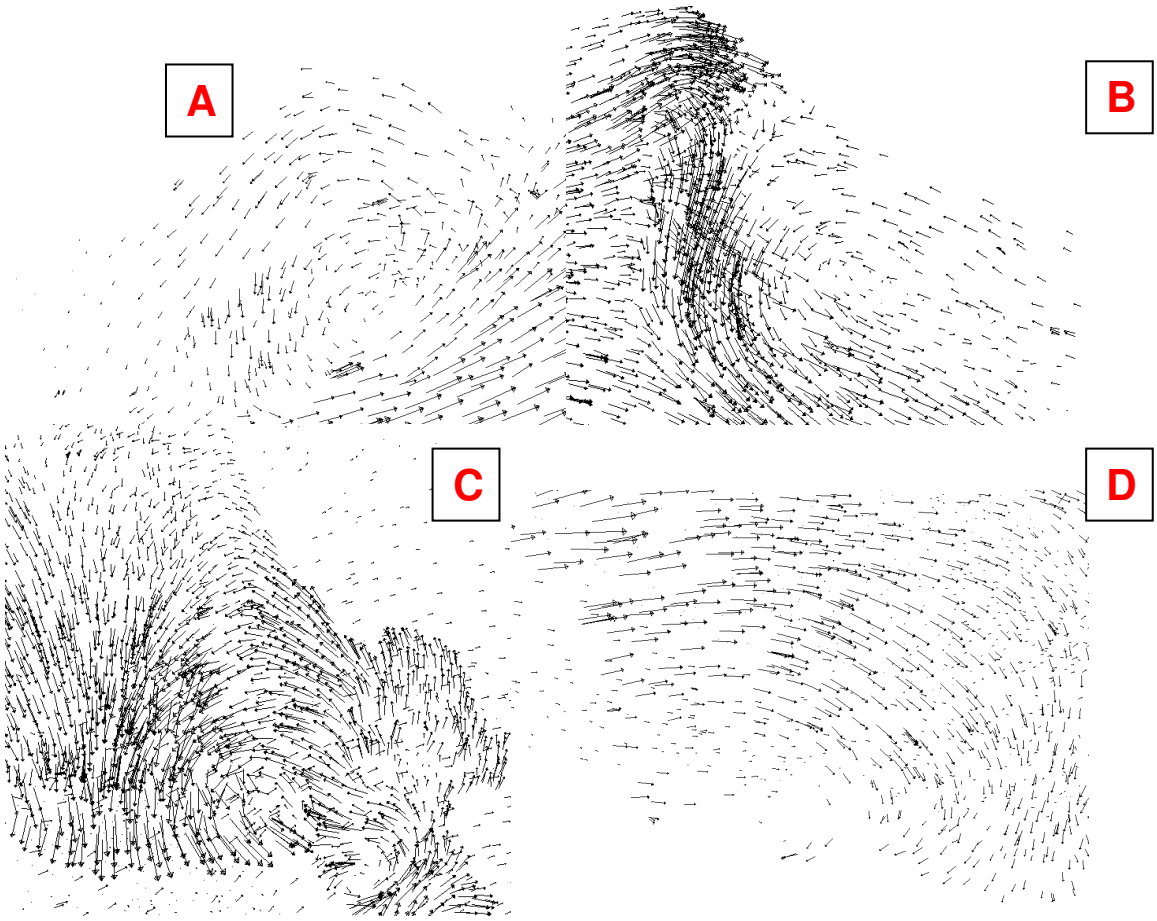

Fig. 6.17 Velocity vector plot for porosity of 0.6 showing recirculation zones in (A) olfactory, (B) superior turbinate anterior, (C) superior turbinate posterior, and (D) inferior turbinate regions

6.3.2 Particle Behaviours

At inspiration, particles injected at a velocity equal to the carrier gas (air) were investigated for their deposition along the domain to give a qualitative visualisation. This was then quantified to predict the velocity behaviour for varying particle sizes. Fig. 6.18a and b shows the particle deposition from the inlet of the left and right nostril through the nasal cavity and pharynx. The discrete phase particles were injected at each node from the surface and by tracking the individual particles it can be seen that particles closer to the boundary are more likely to deposit frequently than particles injected towards the centreline of the model. In vivo, it was observed that more particles were found along the centreline of the fluid flow and fewer particles were found in the vestibule region (Fig. 6.18a).

It can be seen from Fig. 6.18b that as the porosity is decreased, more particles are deposited in the anterior portion of the nasal cavity. Most of the particles were found to be deposited in the vestibule region. Particles in the turbinate region were strongly influenced by the recirculation zone; these cause the particles to deposit in the superior turbinate regions. Greater discussion is presented later in the particle deposition results.

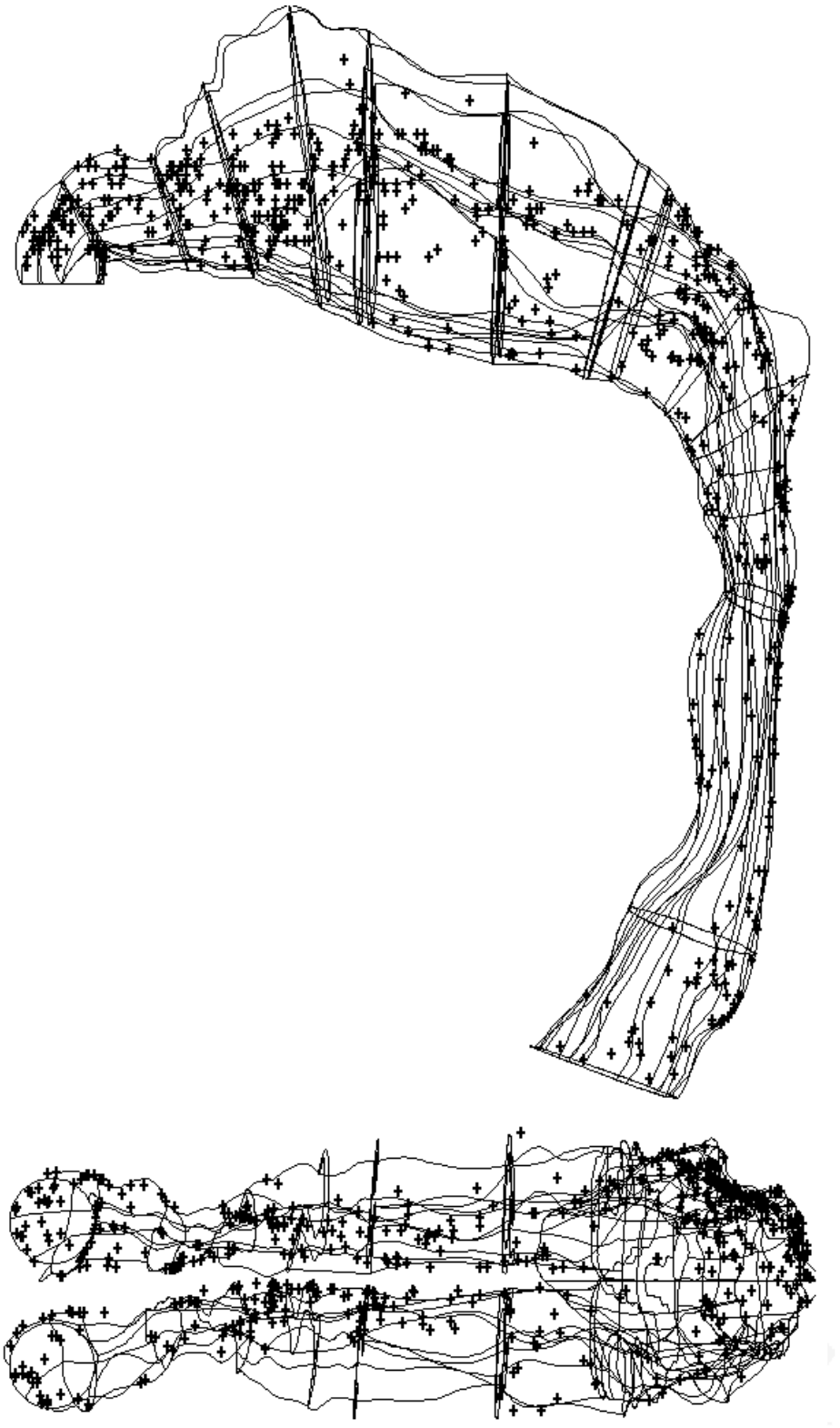

(a)

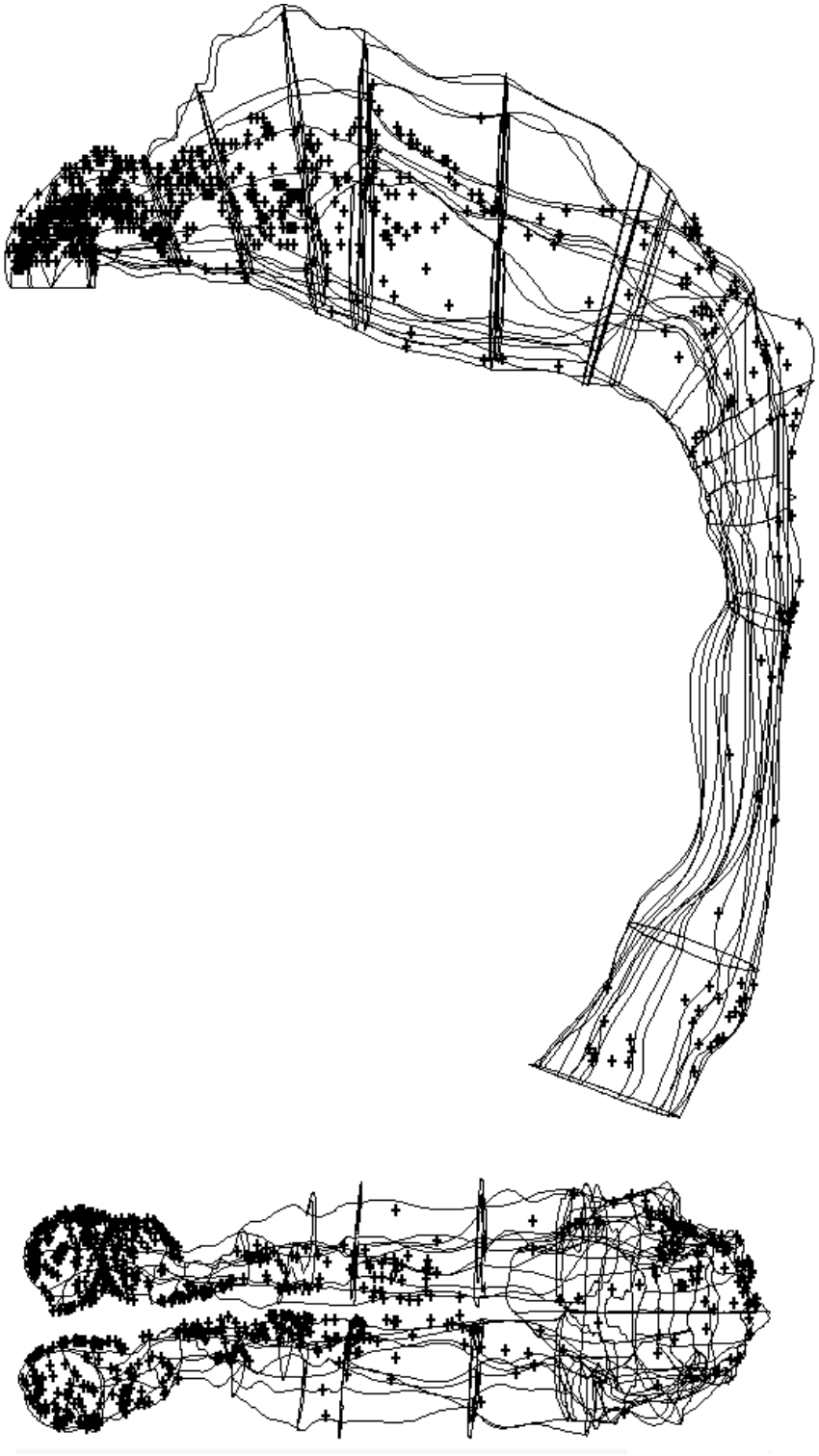

(b)

Fig. 6.18 Particle deposition of a laminar flow inside the domain for a particle diameter of 5µm: (a) non-porous, (b) porosity of 0.6

6.3.3 Velocity Patterns

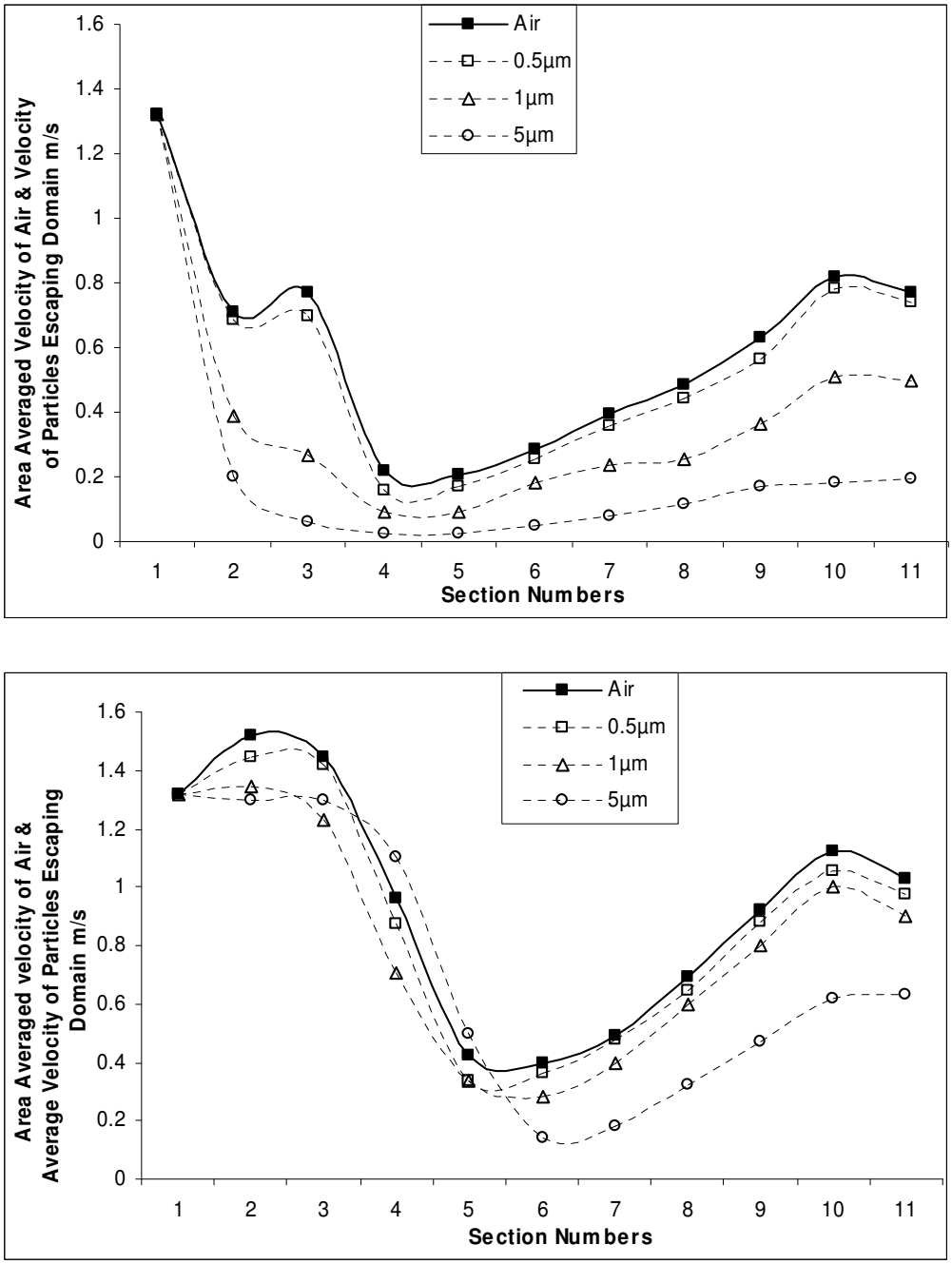

Fig. 6.19 Velocity profiles of carrier gas and particles for a laminar flow: (a) Non-porous; (b) 60% volume open that is porosity of 0.6

Representative results of the distribution of the air and particle velocity through the entire domain averaged by area are shown in Fig. 6.19. As shown in Fig. 6.16, the domain was split into 11 sections and the measured velocity was plotted. This study aims to present a comparative study of the particle and gas velocities and the impact of inertial and viscous loss of the various sized mono-disperse particles during their acceleration and deceleration. Though at inlet conditions air and particles travel at same velocity, the change in the velocity of the carrier gas causes a change in the particle velocity.

An important observation comes from the fact that the inclusion of porous regime in the vestibule region causes an increase in velocity from zone1 to zone2, wherein the velocity tend to decrease for non-porous flow. This change in area averaged air velocity is due to the impact of the momentum sink generated by the porous model. One of the questions answered through this analysis was that the change in the inlet velocity (within laminar flow) through a non-porous medium does not contribute to a change in velocity pattern given the bend between zone1 and zone2, but is only influenced by the addition of porous media. In all cases the velocity decreases as air enters zone3 and zone4. This was however due to two reasons, the volume expansion of the domain structure and the recirculation dominant on the olfactory region. The velocity increases as the domain volume contracts and attains maximum velocity in the pharynx at section 10, where, abrupt volume shrinkage occurs.

Particle velocity behaviour compared with fluid velocity is displayed in Fig. 6.19. With an increase in particle size, particles exhibit deviating trendlines when compared to the carrier gas flow (NOTE: I would replace the observation “deviating trendlines” with what this physically means, eg “varying velocity”). For both porous

and non-porous model the 0.5µm particles follow the exact path of the carrier gas. This shows that there is enough energy in the carrier gas to accelerate the particles and that the particles diffuse completely with the gas. But as the particle size was increased, the energy within the carrier gas becomes insufficient to lift the particles, thereby causing an inertial loss. That is, large particles have higher inertial momentum that increases with the cube of the diameter (volume for constant density) dominating an increase in the square of the diameter (A_p) corresponding to the drag force. Large particles does not reach the same maximum velocity as that of smaller particles, however once they are directed towards the wall they are deposited. Similarly, due to the fluid flow, smaller particles are directed towards the anterior region of the wall. However, the weaker fluid flow is able to redirect many of the smaller particles away from the wall and into the central domain.

At a few instances, it was found that the particle velocity surpassed the carrier gas velocity. This phenomenon was due to the density difference between the carrier gas and the particles. The carrier gas as it enters zone3 and zone4 expands rapidly to fill the domain due to its lower density. But for the particles, due to higher density, the inertial force is still dominant and therefore takes additional time to show a decrease in velocity. Again, as the gas velocity tends to increase from zone5 onwards, it accelerates the particles, however due to its low velocity, a high inertial loss becomes prominent and therefore there exists a high velocity difference.

6.3.4 Particle Deposition Efficiency

Particle deposition efficiency is a ratio of an amount of particle trapped in a specified region to the total amount entered into the model. Particle deposition efficiencies in an anatomically real nasal cavity and pharynx are shown in Fig. 6.20. As

shown in Fig. 6.16 the domain was divided into 10 zones and the deposition predicted for particles of 0.5µm to 10µm. These results obtained suggest that the deposition of particles in the range of 0.5µm to 10µm is more dependent upon the porous regime incorporated into the model. This is indirectly caused by the lower porosity leading to a lower hydraulic volume, in which the fluid flows. This volume restriction enforces a high momentum sink, thereby resulting in an increased physical velocity. This increase in velocity accelerates the particles, thereby causing the particles to deposit on to the walls.

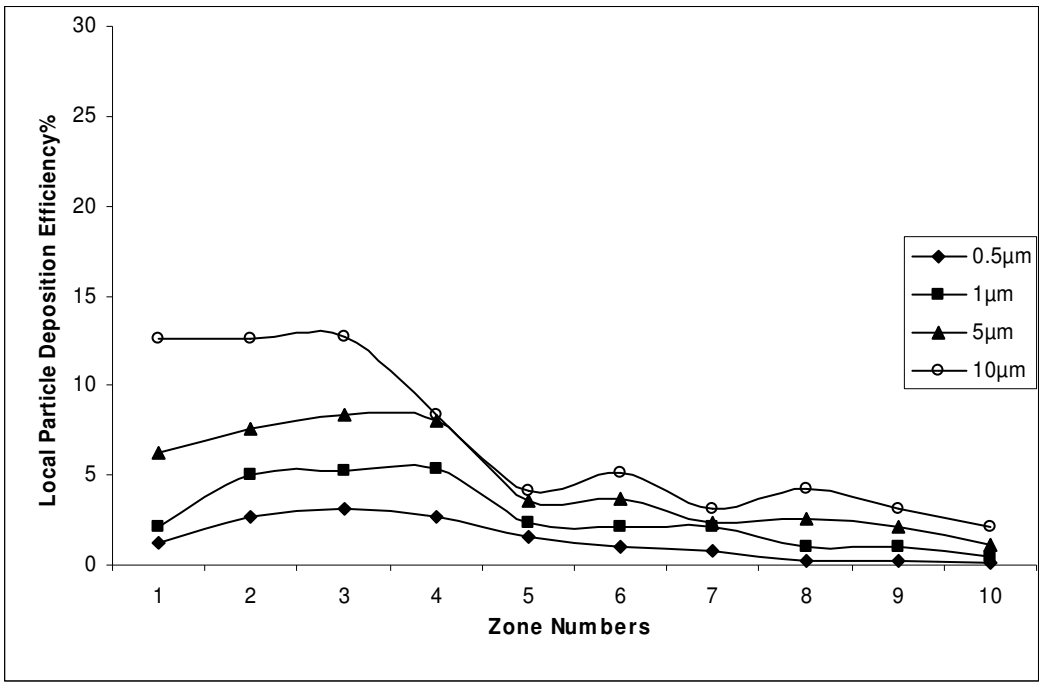

(a)

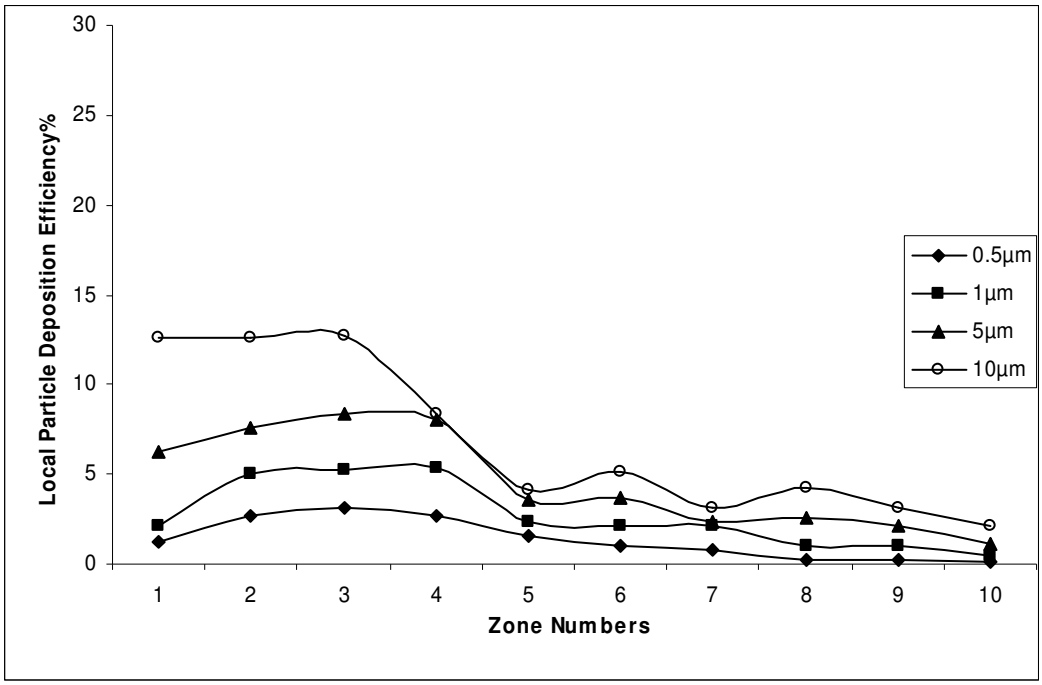
Local Particle Deposition Efficiency%
30
25
20
15
10
5
0
1
2
3
4
5
6
7
8
9
10
Zone Numbers
0.5µm
1µm
5µm
10µm

(b)

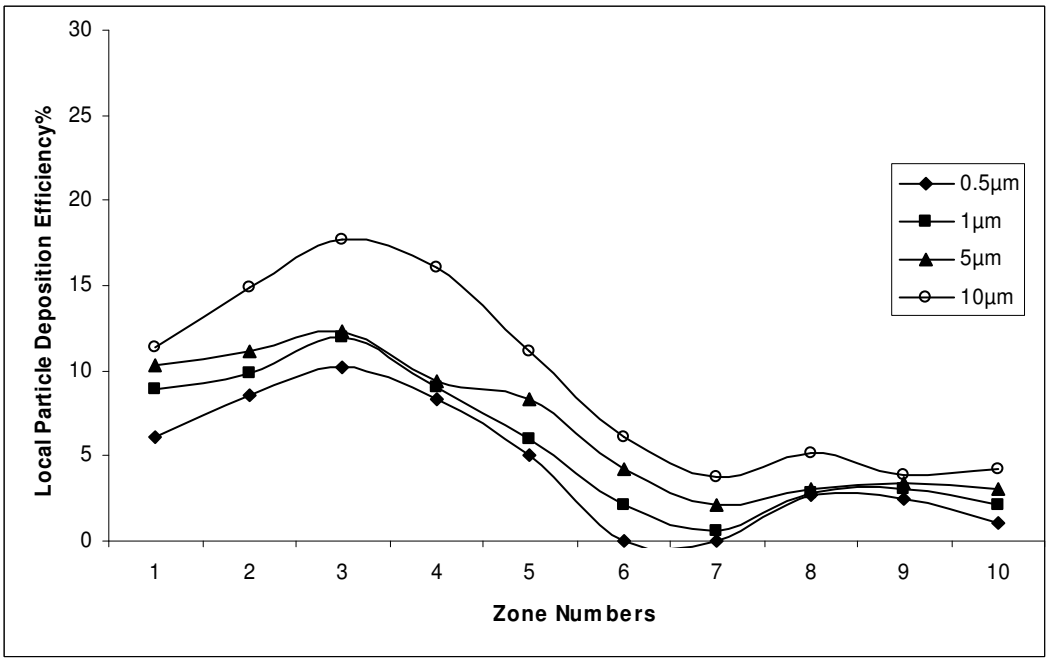
Local Particle Deposition Efficiency%
30
25
20
15
10
5
0
1
2
3
4
5
6
7
8
9
10
Zone Numbers
0.5µm
1µm
5µm
10µm

(c)

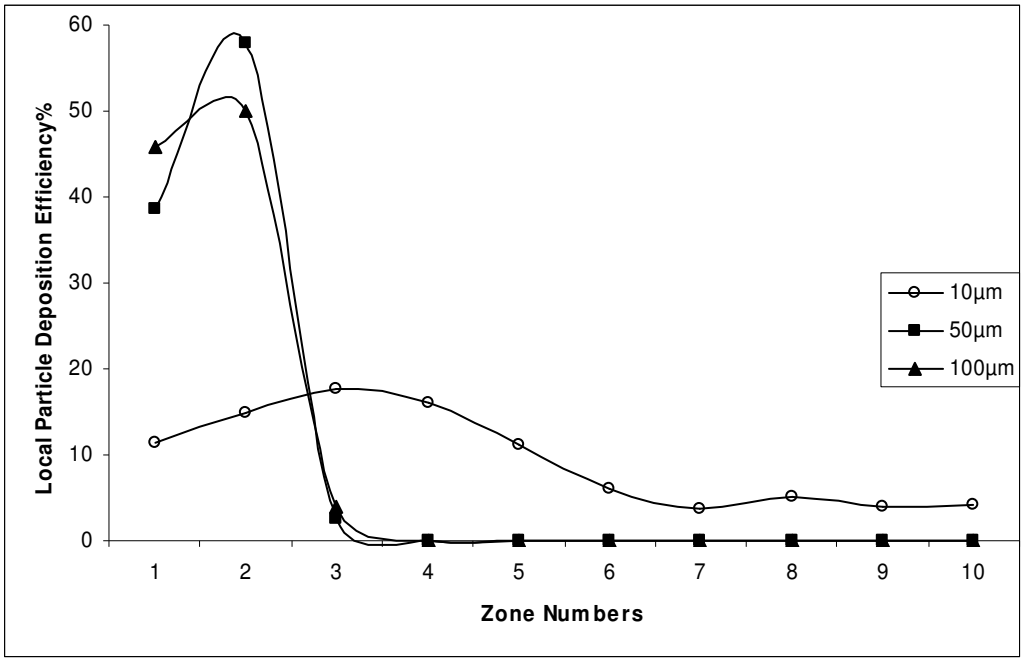

(d)

Fig. 6.20 Local particle deposition efficiency for a laminar flow a) Non-porous vestibule, b) porosity = 0.8, c) porosity = 0.6, d) porosity = 0.6 for particle size of 50 and 100µm

Since there is a bend between zone 1 and zone 2, it was investigated whether the increase in deposition under increased velocities was due to the presence of either the porous media or the geometric bend itself. It can be argued that increase of velocity without the implementation of the porous media would contribute to an increase in particle deposition at the bend. However, an increase in inlet air velocity does not contribute to an increase in particle deposition at the bend as was observed by keeping the flow within laminar parameters. Though the geometrical factors of the vestibule catalyse to the deposition, the presence of porous regime, which acts as a momentum sink, increases the volumetric velocity, thereby causing recirculation that in turn contributes to the increase in deposition. The highest local deposition efficiency was

found to be present at the porosity of 0.6 and was predicted to be around 20%. The highest total deposition of the entire domain was found to be 96% for the 0.6 porosity.

The most important observation for the deposition efficiency comes from the fact that the decrease in porosity favours a shift in deposition pattern towards the anterior region. This, however, is the effect of the difference of the inertial loss between the particles and the carrier gas. As the size of the particle increases, the deposition efficiency increases, however the increase in deposition efficiency is more pronounced only for the particle size of 10µm or more. In cases of particle size of less than 5µm, the deposition exhibits a similar trendline with little variation in the total deposition efficiency.

Simulations were also done for particles of 50 and 100µm, a sample of which is shown in Fig. 6.20d. The deposition of 50 microns and greater suggest that regardless of whether the medium is porous or non-porous the deposition was found to be prominent in the vestibule region of the nasal cavity. This occurrence was observed due to the fact that there was not enough acceleration of the particles and the gravitational force dominated over the inertial force. In any case this was found to be consistent with the experiments carried out by Cheng et al. (2001). The effect of secondary flow of the carrier gas on the particles could not be established, as all particles were deposited in zone1 and 2 and no particles were found in zone3 where recirculation occurs.

Though it was argued that the use of *k-ε* model for complex geometry such as nasal cavity is not appropriate and generates serious errors, a realisable k-ε model was run with a flow rate of 30 l/min (for human running condition) to observe the characteristics of particle deposition. Fig. 6.21 shows the local particle deposition for *k-ε* turbulence model. It can be observed that, as the porosity decreases, the deposition

increases as was found with laminar flow, but with high deposition efficiency. Increased particle deposition towards the anterior region, as a result of porosity decrease, was also observed in turbulence model. These results are preliminary and therefore no conclusive argument was drawn to establish the validity of k-ε for the turbulence model.

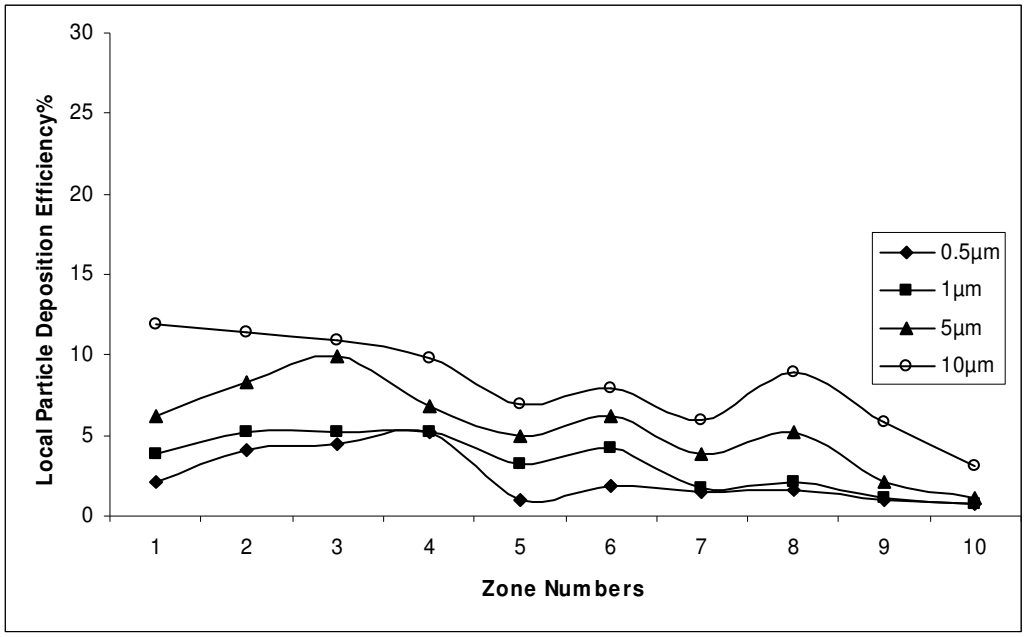

(a)

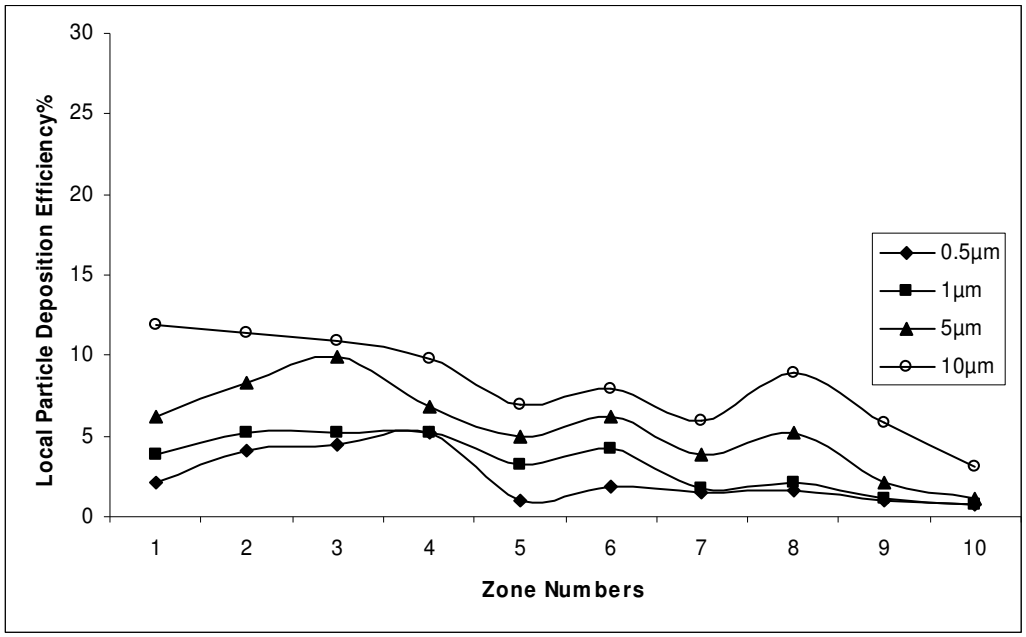

(b)

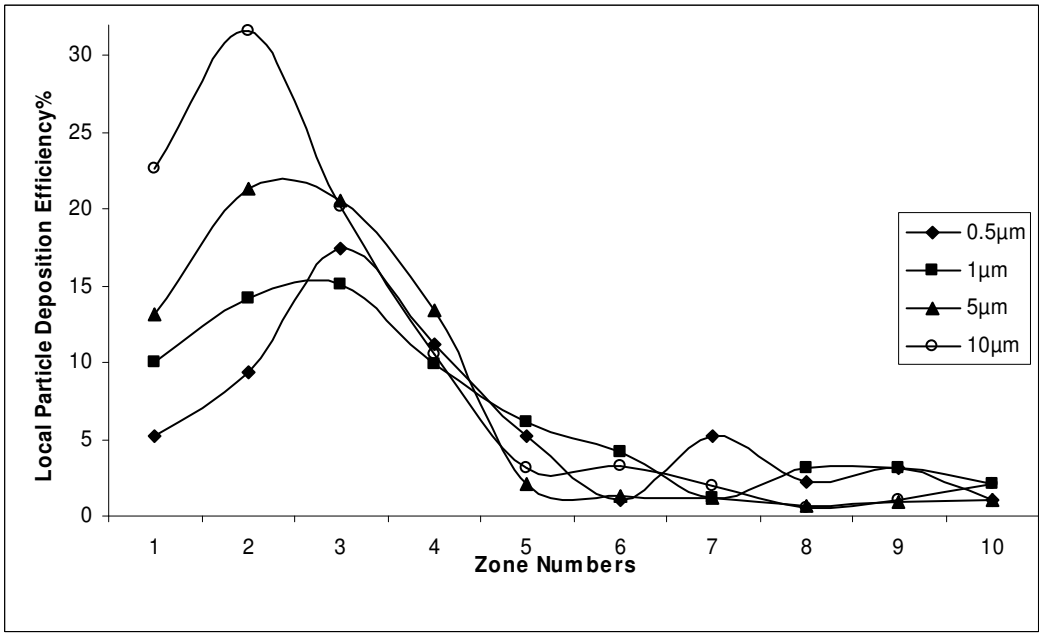

(c)

Fig. 6.21 Local particle deposition efficiency for a turbulent flow a) Non-porous vestibule, b) porosity = 0.8, c) porosity = 0.6

Total particle deposition as a function of porosity particle sizes is shown in Fig. 6.22. It can be seen that for particle diameter of 5µm or less the difference in total deposition efficiency is less significant. With decreasing porosity this difference becomes increasingly significant as the particle size increases beyond 10µm. Quantitatively, it increases by 60% between a non-porous domain and a domain having a porosity of 0.6.

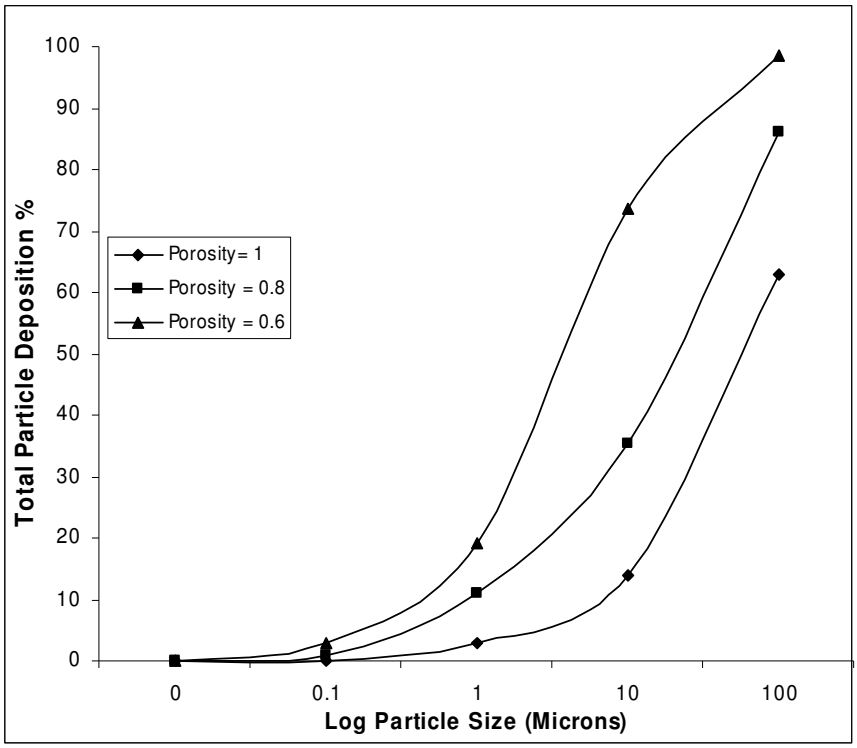

Fig. 6.22 Total deposition efficiency of the vestibule region (zone1+2)

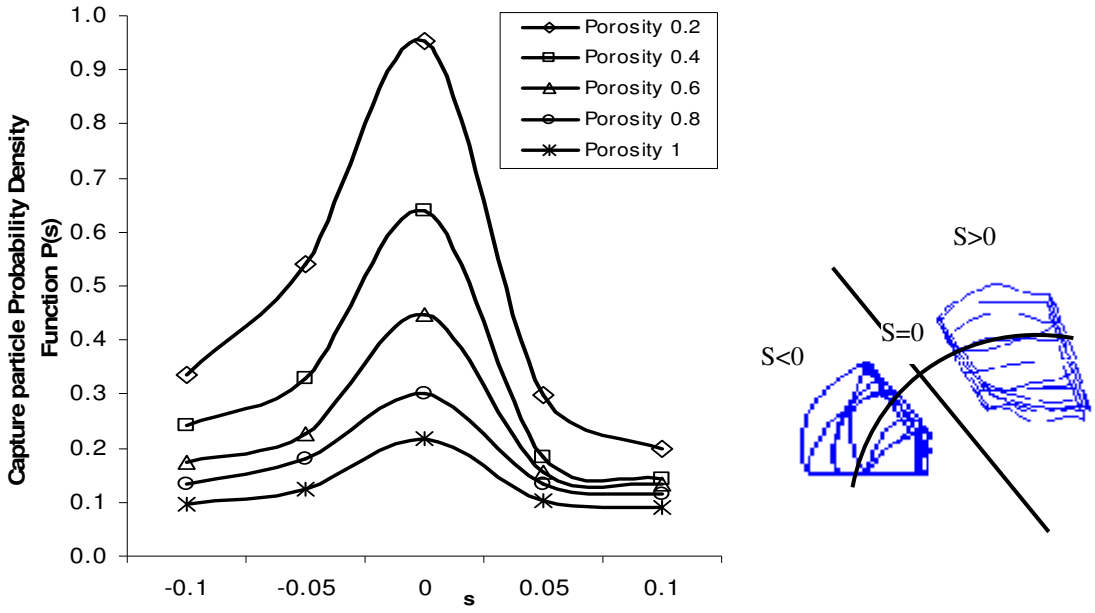

Fig. 6.23 Capture particle probability density function of porosity in vestibule region

The capture probability density function was also found within the porous vestibule region. This gives the probability to impact the wall at a given point dependent on the curvilinear co-ordinate, s, such that s = 0 at the bend. In Fig. 6.23, it is shown that the deposition occurs essentially close to the bend of the vestibule, the distribution of which is not symmetrical. The deposition is more pronounced for $s < 0$, that is the on the side of the vertical flow. The reason is that the inertial effect is more significant as particle trajectories are curved when $s < 0$. More precisely, flow streamlines are almost straight lines when they go to the exit channel ($s>0$) thereby inertia drives particles away from the wall causing less capture efficiency. Assuming that the particles accumulate at the point where the capture probability density function is higher, it is clear that the corresponding deposits should grow at that location ($s = 0$). This is experimentally substantiated by Frey (1999), in which he considered fluid-

particle flow inside a pore-hole enclosure. An extrapolation of the porosity shows that lower the porosity, the higher the probability density function is, at the bend. Therefore, inertial and viscous terms of the virtual pore-holes on the fluid strongly effects particle motion, which causes more particles to deposit in the bend structure, as well causing a deviation of symmetry. However, these predictions were plotted independent of the particle size. These results obtained suggest that the inclusion of the porous regime in the model has a significant effect on the deposition.

6.3.5 Conclusions

This CFD study examined the incorporation of a simple porous model to emulate the nasal hair growth by assuming virtual pore holes inside the vestibule region. Given the complexity of the geometry it was considered to include only the laminar flow in the porous-model. The results suggest that the inclusion of the porous-model significantly increased both local and total deposition inside the nasal cavity and pharynx. For the non-porous model the velocity of the fluid and particles were found to decrease, but were found to increase in the porous model. Decrease in porosity contributes to an increase in deposition in the anterior region and also caused a forward shift in the pattern of the local deposition efficiency. The one-way coupling used in this model accounted for an inertial loss on the particle motion and that increased with an increase in particle size.

Considering these preliminary results, it can be seen that there is a need to further investigate the use of a porous medium to enhance our knowledge of the mechanisms of targeted delivery of therapeutic sprays and also to study the impact of environmental pollution in the nasal cavity. Though these predictions form a basis of

fundamental understanding, experiments are required to validate the model. The Large Eddy Simulation (LES) turbulence model could also be incorporated for higher flow rates. These unresolved issues form a foundation for our continued research.

6.4 Airway bifurcation and trachea airway

6.4.1 Model Validation

The DE of aerosol particle in double bifurcation airway model for different flow rates and particle sizes (i.e. Stokes number) has been validated with various experimental data sets (cf. Kim & Fisher, 1999; Schlesinger et al., 1982). Kim & Fisher (1999) suggested modified logistic functions to describe DE vs. Stokes number for the first two bifurcations, which were based on the trend lines fitted on experimental data using double-bifurcating symmetrical glass tube models with steady inhalation. However, the equation was bounded in range of St 0.01 to 0.2 due to the setting of the experiment. Schlesinger et al. (1982) measured the DE on the replicate hollow casts from a solid cast of a human tracheobronchial tree for the first five branching generations. Similarly, the DE was plotted against the Stokes number for different bifurcations under constant flow rates. Figure 6.24 shows the experimental data and CFD predicted deposition efficiencies for the first two bifurcations in range of St 0.01 to 0.12. When comparing the experimental results between a replicate human cast model and a symmetrical glass tube model, there is small differences in DE when the Stokes number is less than 0.1. Similarly, when comparing DE between CFD prediction and experimental data, the differences are approximately within 5% in DE value.

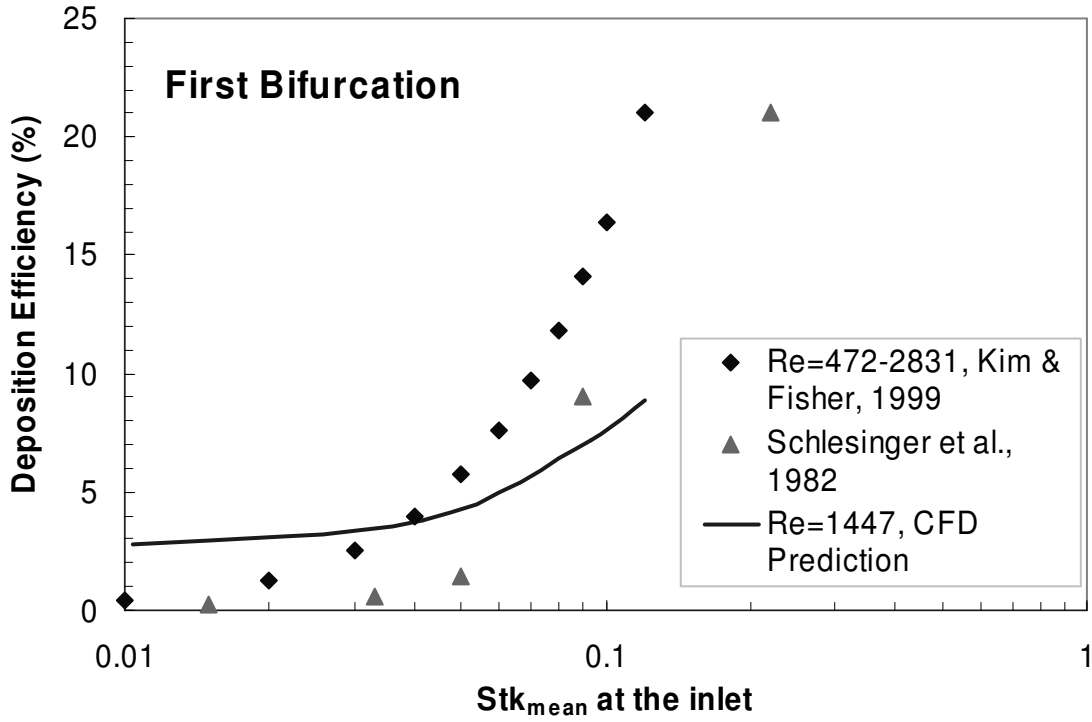
First Bifurcation
Deposition Efficiency (%)
25
20
15
10
5
0
0.01
0.1
1
Stk mean at the inlet
Re=472-2831, Kim & Fisher, 1999
Schlesinger et al., 1982
Re=1447, CFD Prediction

(a)

(b)

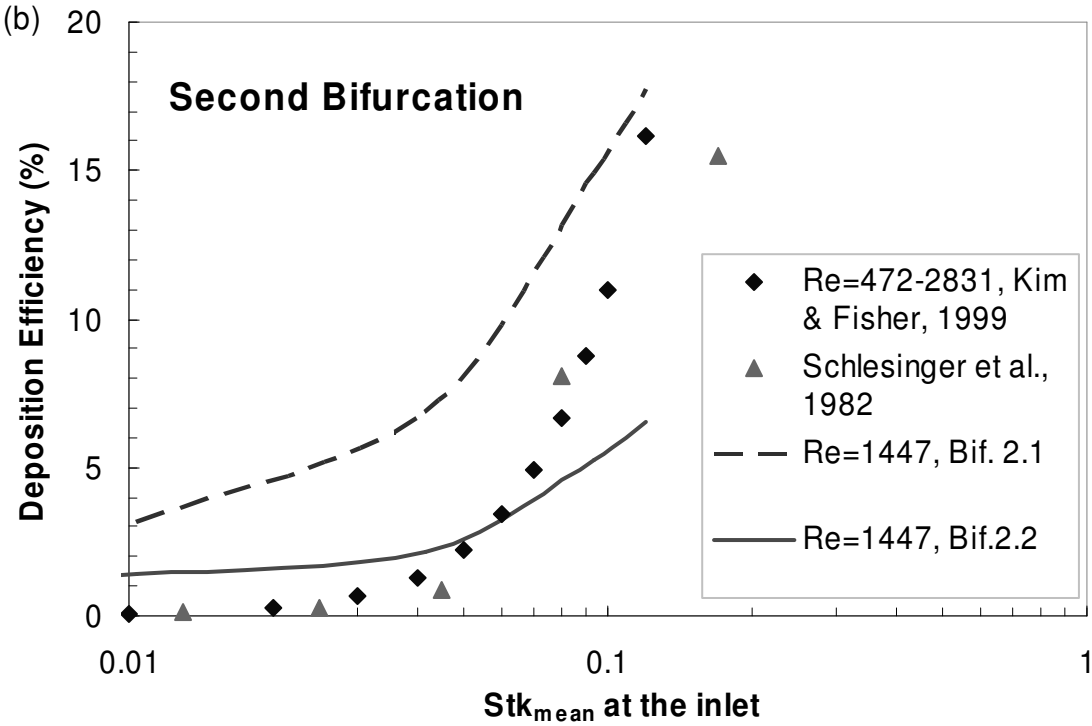
Second Bifurcation
Deposition Efficiency (%)
20
15
10
5
0
0.01
0.1
1
Stk mean at the inlet
Re=472-2831, Kim & Fisher, 1999
Schlesinger et al., 1982
Re=1447, Bif. 2.1
Re=1447, Bif.2.2

(b)

Fig. 6.24 Comparison of the predicted and experimental particle deposition efficiency (DE) in double bifurcation models under steady inhalation (a) DE at the first bifurcation; and (b) DE at the second bifurcation.

Due to the difficulty in precisely controlling the experimental conditions, such as flow rate and aerosol size, the Reynolds number and Stokes number fluctuated in a measurable range. In addition, the small differences between the experimental measurements and computational predictions can be caused by discrepancies in model geometries (e.g. branching angle of bifurcation, bronchial length, etc.) and the method of deposition measurements. In addition, Zhang and Finlay (2005) proved that cartilaginous rings increase DE significantly in the trachea and conjectured that cartilaginous rings may be a critical element in influencing the prediction of particle deposition. Since the model was constructed based on a realistic airway, the model is unique in terms of geometrical details. Therefore, it is not practical to divide the bifurcation zones and generations based on other results that were mentioned previously. However, the general configuration in dividing the bifurcation zones were cautiously compared with the experimental setup by Kim & Fisher (1999) and Schlesinger et al. (1982) in order to achieve comparable results. Therefore, when neglecting the experimental uncertainties and differences in geometry, the characteristics of the CFD results correspond to the experimental data reasonably well.

In summary, the present CFD model is proven by the reasonable agreements between experimental data and other CFD predictions. The results show that the current CFD model setting is sufficient to provide tolerable accurate information in terms of fluid-particle dynamics and particle deposition in a realistic double bifurcation lung airway model.

6.4.2 Axial velocity and secondary velocity profiles

In order to investigate the development of particle deposition within airways, the normalized axial and secondary velocity profiles of air flow are drawn and two inspiratory conditions (resting and moderate exercise) were compared. Figure 6.25 shows two sets of axial velocity profiles in the trachea at two flow rates (15 and 60 l/min). The flow rate used here corresponds to the flow rate in the trachea. In Figure 6.25(c), the positions of stations for axial velocity profiles are marked with the thinner line with letter T, Lb or Rb next to it and the abscissa (0 and 1) shows how the lines are placed in the profiles. Similarly, secondary velocity profiles (in Fig. 6.26) are marked with a thicker line with A-A', B-B' or C-C' marks which specify the position of sections. The velocity profiles were validated with Chang and El Masry's (1982) experimental data (plotted as square dots), in which they measured steady inspiratory velocity profile using a scaled human tracheobronchial airways model, which the model configurations were very close to the CFD model used here. The numerical results generally have good agreement with experimental results in terms of characteristic features. The small differences in some of the stations are to be expected since the experimental model was made of smooth plastic tubes. Also, the flow rate used in experiment and numerical simulation were different. The Reynolds numbers obtained in trachea were 2123 and 8846 in Chang and El Masry's (1982) experiment compared to1447 and 5789 in this numerical study.

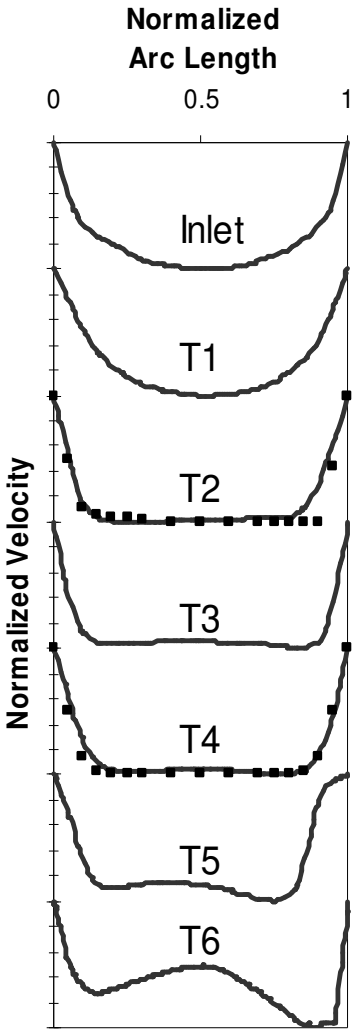
Normalized
Arc Length
0
0.5
1
Normalized Velocity
Inlet
T1
T2
T3
T4
T5
T6

(a)

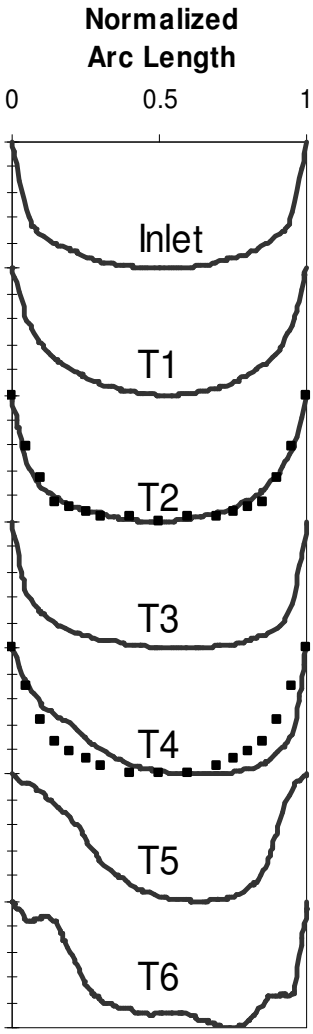
Normalized
Arc Length
0
0.5
1
Inlet
T1
T2
T3
T4
T5
T6

(b)

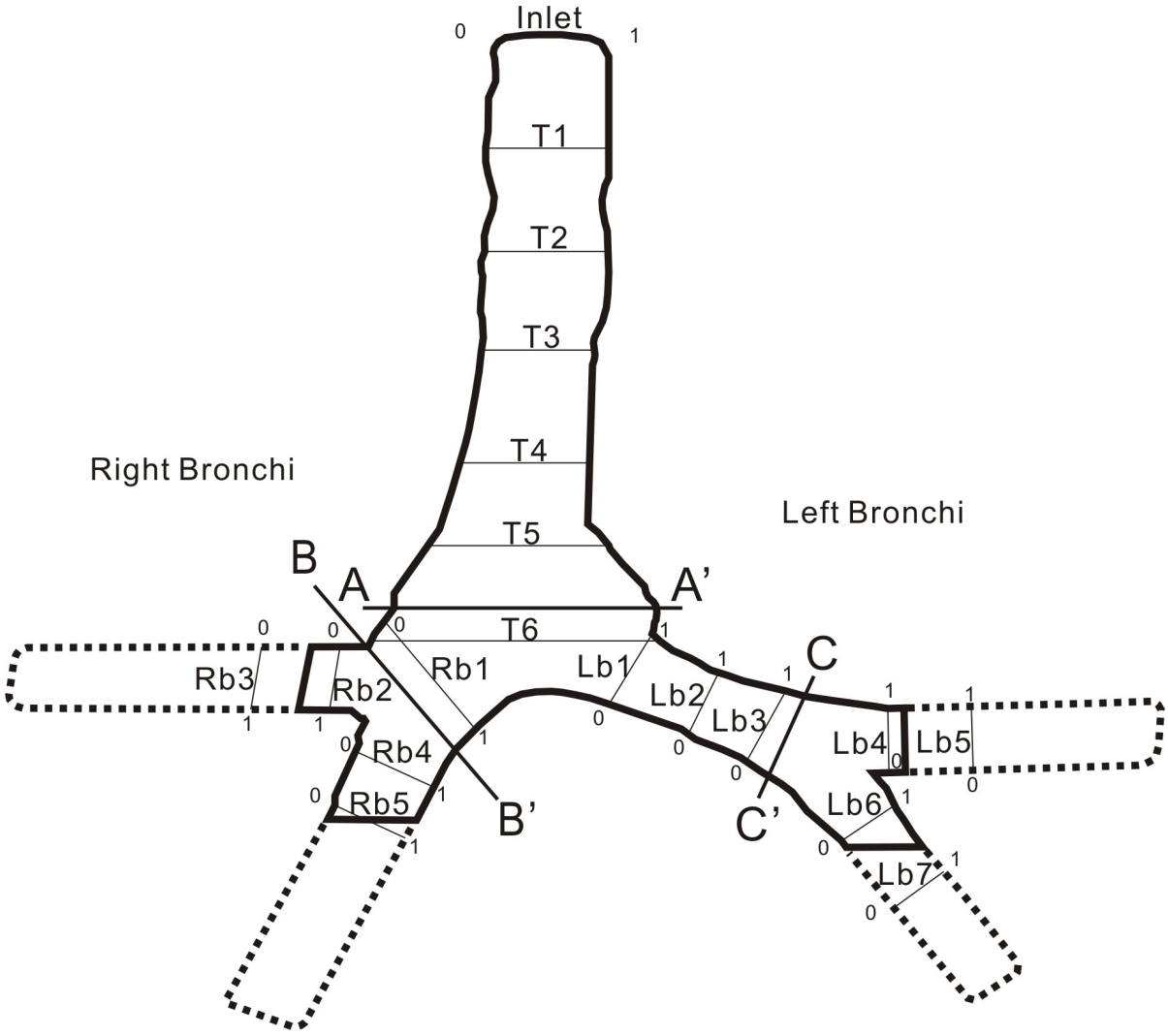

(c)

Fig. 6.25 Normalized velocity profile at trachea for an inspiratory flow rate at (a) 15 l/min and (b) 60 l/min, plotted as a function of the normalized arc length. The experimental data of Chang & El Masry (1982) are plotted as (■) for the corresponding stations. Abscissa 0 and 1 correspond to the marks, 0 and 1 in (c). (c) View of station position (The letter T represents Trachea; Rb and Lb represent the Right and Left side of Bronchus respectively. The thicker line with A-A', B-B' and C-C' indicate the position of section that is taken to visualize the secondary flow in Fig. 6.26.)

Figure 6.25(a) and (b) show that both entering profiles were of a parabolic shape, although they were beginning to develop into a different profile shape, due to the different flow rate. Figure 6.25(a) shows that the profiles from station T2 were flatter than the profiles in Fig. 6.25(b). Also, the profiles started to develop into a bi-peak structure from station T5 to T6. Comparatively, the profiles in Fig. 6.25(b) were parabolic in shape and these shapes almost stayed the same until the flow met the first bifurcation. The reason that the higher flow rate (60 l/min) had a parabolic shape was due to higher viscous effects, which were gradually propagated toward the centre of the trachea. In other words, the less viscous effect in the lower flow rate (15 l/min) caused a flatter shape in the centre of the trachea. In addition, both velocity profiles at T5 had a low velocity zone near either one or both ends but both profiles at T6 show that the fluid recovered its inertia force. This phenomenon indicates that there were flow separations between T5 and T6 near the outer wall due to a sudden change in diameter. However, the higher velocity profiles at T4 to T6 also show that, due to greater inertial force, the flow separation seemed to be more sensitive to change in diameter. T4 already shows a drop in velocity near right side (abscissa 0) of the wall and continued this low velocity till the fluid met the first bifurcation. Therefore, the velocity profiles in the lower flow rate at station T6 was more moderate compared to the higher flow rate, which has peak flow concentrated in the middle of the airway.

Similarly, the secondary velocity profile in Fig. 6.26 (section A-A") also reflects the characteristic of the peak structure (high velocity zone in lightest color) in both flow rates. The lower flow rate had the high velocity zone distributed more evenly over the left and right bronchus, as indicated by velocity contour graph. On the contrary, the higher flow rate had the high velocity zone concentrated in the middle of the trachea.

The secondary velocity vector graph is also a good indicator of showing how particles are distributed within airways. It shows that the direction of the flow in lower flow rate had a “more complete shape” and larger vortex than higher flow rate whereas the vortex in left hand side of Fig. 6.26(b) (right bronchus) was weak in velocity magnitude and displayed turbulence.

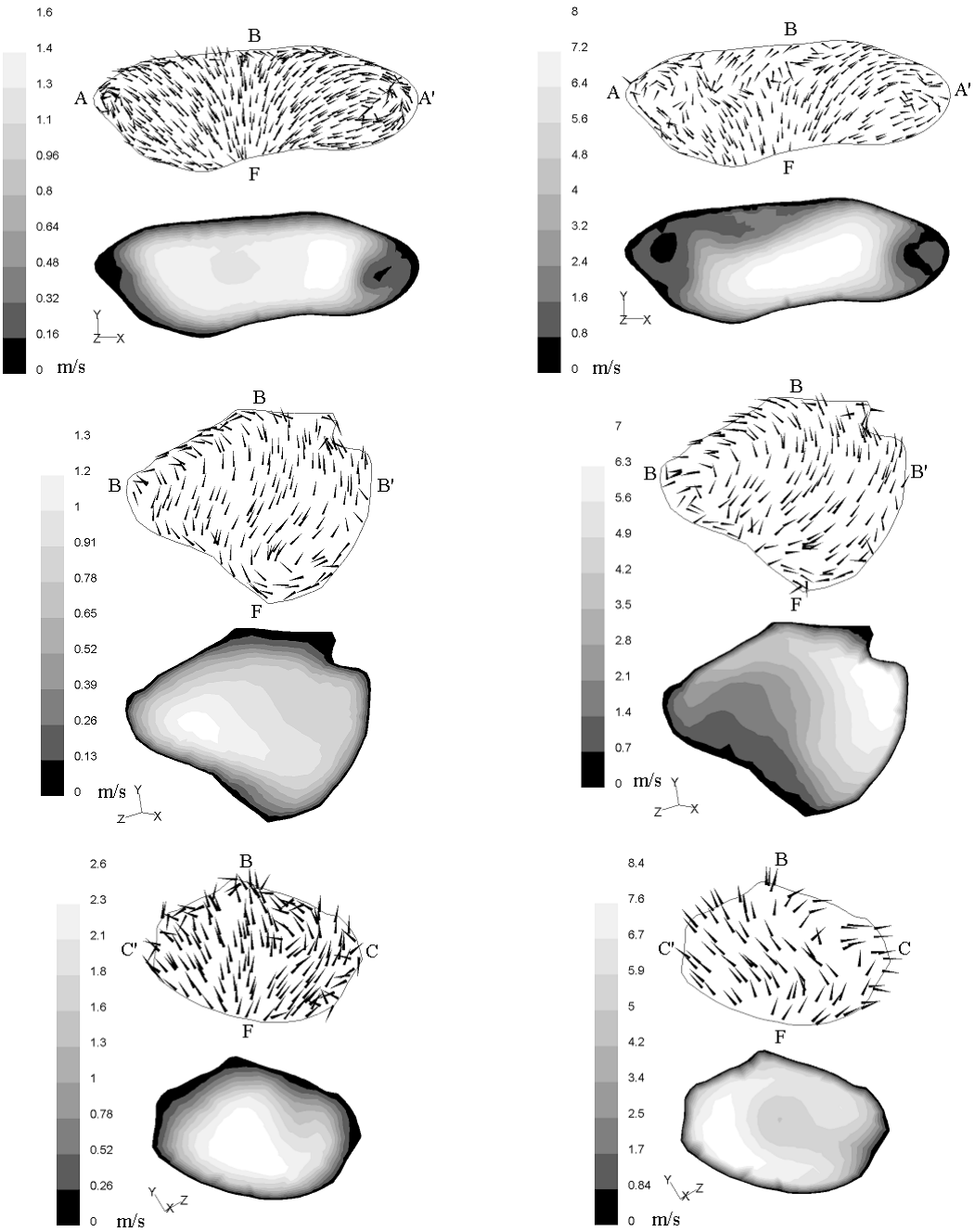

Fig. 6.26 Secondary velocity vector and velocity contours plots at section A-A', B-B' and C-C' (Refer Fig. 6.25(c) for position of sections) for an inspiratory flow rate at (a) 15 l/min and (b) 60 l/min. The letters (B and F) on top and bottom of the vector graphs indicate where the Back and Front of the section are.

Figure 6.27 depicts the common and the difference of velocity profile that both flow conditions (15 and 60 l/min) had. The velocity profiles in the right bronchus (Rb1) at the lower flow rate was more moderate than higher flow rate and had a high peak near the lateral wall (abscissa 0) while the profile of the higher flow rate was highly skewed toward the inner wall of the bifurcation. The secondary profiles at section B-B' in Fig. 6.26 correspond to the previous descriptions, but the velocity vector graph also indicates that the fluid at lower flow rate only tended to move toward the back of the airway due to the upstream vortex shading (cf. section A-A'). Whereas, the fluid motion at higher flow rate not only tended to move toward the back of the airway, it also moved toward the inner wall of the bifurcation (B').

Further downstream in the right upper (Rb2 and Rb3) and lower (Rb4 and Rb5) bronchi, the axial velocity profiles generally continued the basic structure from the previous profiles (Rb1). At lower flow rate, the profiles in the upper bronchi were skewed toward the inner wall of the second bifurcation while the velocity magnitudes were lower near the outer wall (abscissa 0). This phenomenon is likely to be caused by the flow separation or mild reverse flow near the bend of the first bifurcation (near Rb2) (Daily and Harleman, 1966). However, the higher flow rate was able to overcome the adverse pressure gradient near the outer wall of the first bifurcation due to its greater momentum (as discussed by Chang and El Masry (1982)). The velocity profiles

in the lower bronchi at the lower flow rate were fairly blunt and almost symmetrical due to the small branching angle. On the other hand, due to the greater inertia forces (higher flow rate) from the upstream which caused significant pressure on the carina ridge of the second bifurcation, the velocity near the inner wall was either mild and reversed or very slow, so the velocity profiles were low in the inner wall and high in the outer wall of the second bifurcation.

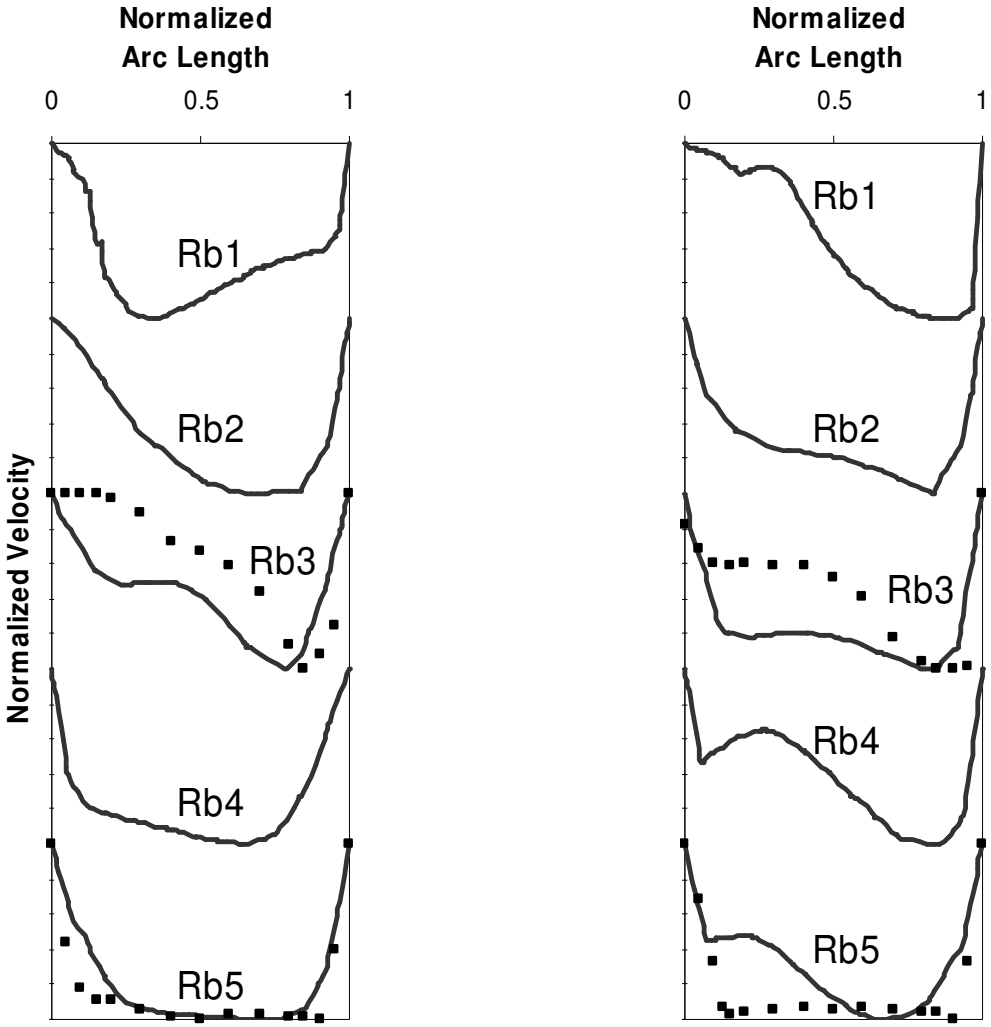

(a) (b)

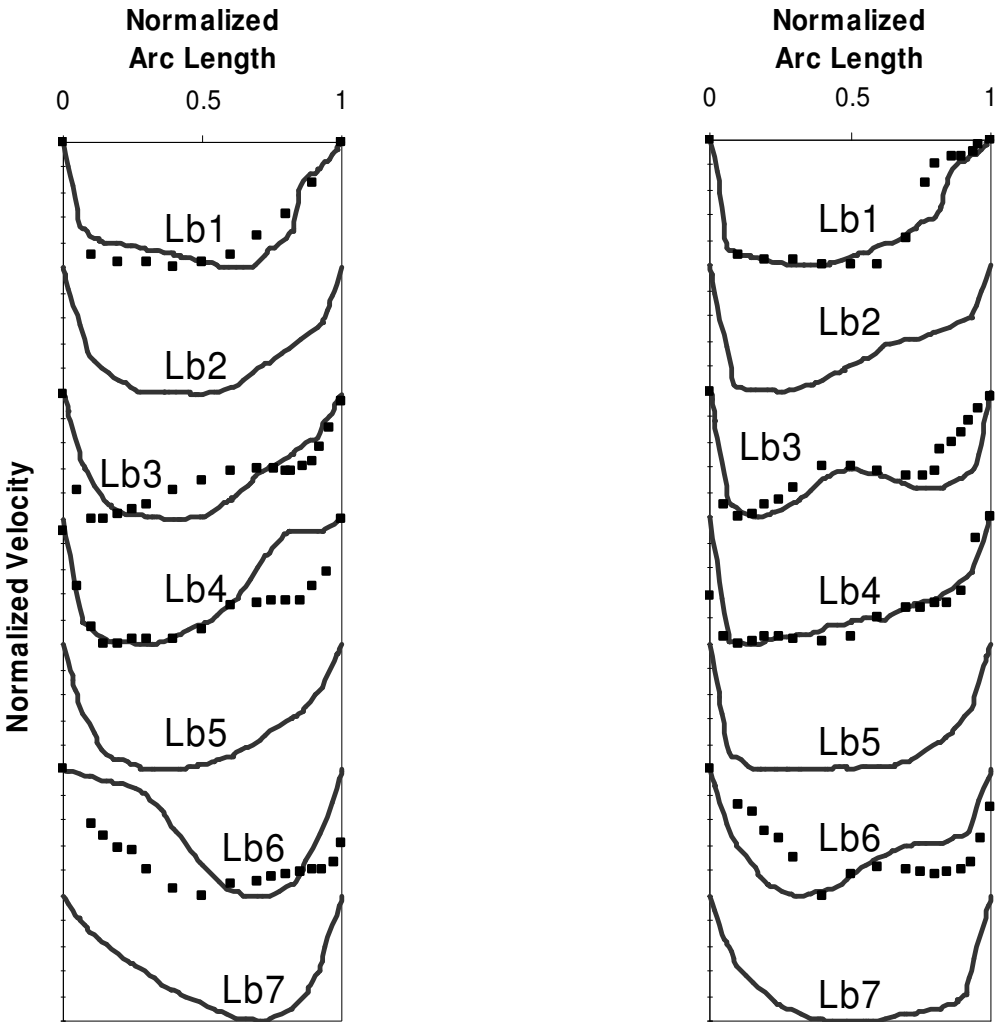

(c) (d)

Fig. 6.27 Normalized velocity profile at bronchus for an inspiratory flow rate at (a) & (c) 15 l/min and (b) & (d) 60 l/min, plotted as a function of the normalized arc length. (Refer Fig. 6.25(c) for station position)

Three sets of velocity profiles at left bronchus (Lb1 Lb2 and Lb3) are presented in Fig. 6.27. At the lower flow rate, profile at Lb1 was like a mirror image of the profile at the other side (Rb1) where the low velocity zone near the outer wall (abscissa 1) was caused by flow separation. But, the profiles at Lb2 and Lb3 show that the flow separation was reattached at a short distance from Lb1 due to the low velocity flow. With the higher flow rate, the profile at Lb1 had slow fluid motion near outer wall of

the first bifurcation due to large branching angle where again the flow separation or mild reverse flow occurred near the outer wall of bifurcation. But the fluid at Lb2 and Lb3, near the outer wall (abscissa 1) soon accelerated from a low velocity. This phenomenon can be explained by the transverse momentum exchange associated with higher Reynolds number flows as suggested by Chang and El Masry (1982). The secondary profiles at section C-C' in Fig. 6.26 is virtually showing Lb3, but in a transverse plane, whereas the high velocity zone concentrated in the middle of the airway for the low flow rate condition. Here the fluid only tended to move toward the back of the airway due to the upstream vortex shading (cf. section A-A'). In contrast, the fluid motion at the higher flow rate was not only tended to move toward the back of the airway, but it also moved towards the inner wall (C').

At flow rate of 15 l/min, both the upper (Lb4 and Lb5) and the lower (Lb6 and Lb7) bronchi had peak velocities skewed toward the inner wall of the second bifurcation and a very low velocity near outer wall. This indicated flow separation. In comparison, there was no flow separation observed near the outer wall using the 60 l/min flow rate. Also the peak flow in the upper bronchi (Lb4) skewed toward the inner wall was relatively moderate compare to Lb4 at the 15 l/min flow rate. Surprisingly, the peak flow in the lower bronchi (Lb6) skewed more towards the outer wall of the second bifurcation, which is also the extension from the inner wall of the first bifurcation.

6.4.3 Regional deposition efficiencies

Deposition efficiency (DE) is an important quantitative parameter, defined as the percentage of particles that are trapped on a designated airway surface (such as bifurcation or zone) with respect to the total number of particles entering the respiratory system. Figure 6.28 compares the deposition efficiencies at the first bifurcation (B1)

and the second bifurcations at right bronchi (B2.1) and left bronchi (B2.2) and indicates how the flow rate affects the DE within different bifurcations. Figure 6.29 and 6.30 summarize all the DE results collected within this numerical simulation and illustrate them with respect to individual bifurcation in three different inlet flow rates. Then, the DE results are not only made against particle diameter, but also against the mean Stokes number, as measured at the inlet, which is calculated by a number of variables (mean inlet velocity, particle diameter) and constants (particle density, inlet diameter and air dynamic viscosity). Figure 6.29(b), 6.30(b) and (d) reveal the DE characteristic in combination of fluid velocities (i.e. flow rates) and particle sizes.

Figure 6.28a shows that the DE at 15 l/min (inlet flow rate) in every bifurcation was quite even for particle sizes ranging from 1 to 5 micrometres and the DE in all bifurcations increased with the particle size. The DE at the right second bifurcation (B2.1) increased more considerably than both B1 and B2.2 as soon as particle size exceeded 5 micrometres. This was due to the fact that there was a peak velocity flow (cf. Fig. 6.25a – Profile T6) near the carina ridge in the right second bifurcation. Therefore, the peak velocity flow gave greater inertial force to the particles on the surroundings of the ridge and hence created higher particle deposition. As a result, the DE would increase further for larger particles due to the greater impact of the particles. Nevertheless, the second bifurcation in both sides (B2.1 and B2.2) seemed to reach their maximum DE in the tendency of the line when particle size reached 20 micrometres and on the contrary, the DE in the first bifurcation tended to increase further if the particle size were raised even more than 20 micrometres. Likewise, these similar behaviours were also observed in Fig. 6.28(b) when the inlet flow rate was 60 l/min. There were differences in that the DE in the first bifurcation at 60 l/min inlet

flow rate was higher than 15 l/min inlet flow rate for all particle sizes. This is due to the greater inertial force given by the larger flow rate. Also the DE in the second bifurcations reached the maximum DE with smaller particles (10μm) at 60 l/min compared to 15 l/min condition (20μm). Nonetheless, the DE in the right second bifurcation (B2.1) was still considerably higher than the left second bifurcation (B2.2). This was also shown by comparing Figure 6.29e and f with a Stokes number smaller than 0.2. The reason that B2.1 had a higher DE than B2.2 was that the left bronchus (B2.2 side) is considerably longer than right bronchus. This means that particles have to travel further to reach the region of B2.2 which in turn reduces the chance for a particle to be trapped in region B2.2 because a part of the particles were trapped along the left bronchus (as shown in Fig. 6.31 to 6.34).

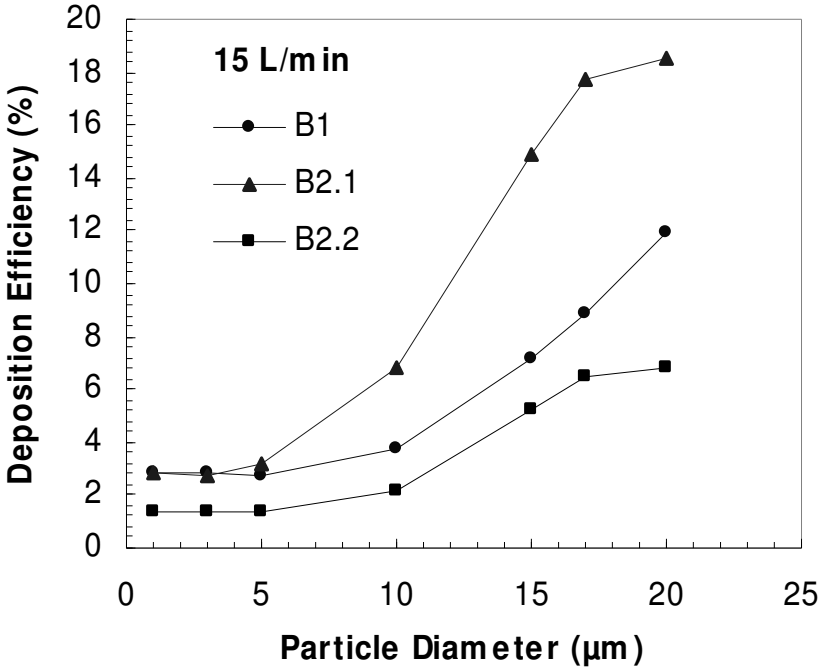

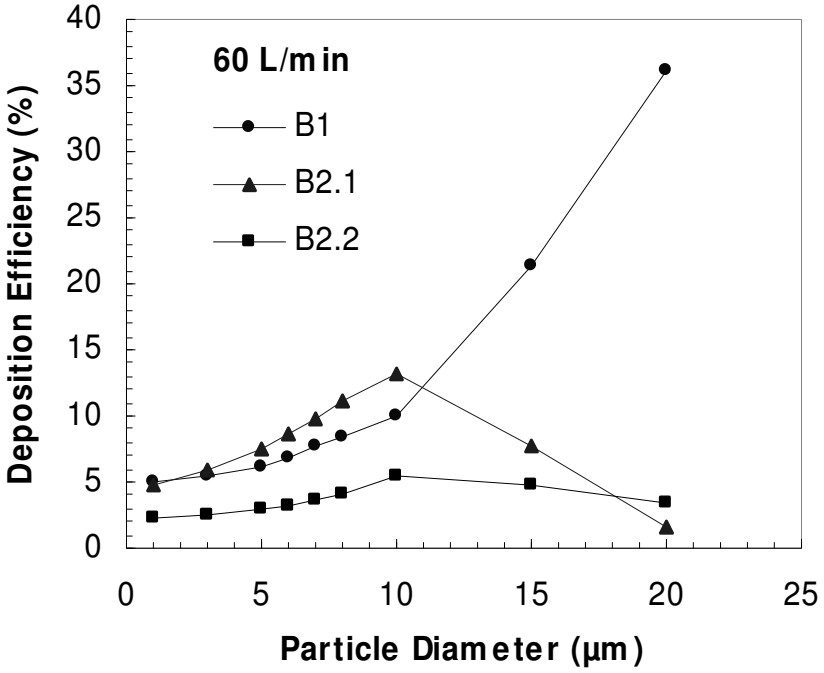

Fig. 6.28 Plot of deposition efficiencies for two flow rates

Figure 6.29a shows that a higher flow rate gave a higher DE in the first bifurcation. This was more noticeable when the particle size increased. As expected, the high inertial force created by large particles and/or high flow rate led to a high DE. It should be noted that this only happened in the first bifurcation. In the second bifurcations, the previous characteristic only applied for certain ranges of small particles. As depicted in Figure 6.29c and d, the DE dropped when the particle size rose to a certain point. (e.g. at 60 l/min, DE dropped at 10µm in B2.1) This was due to the fact that more particles were already trapped in the first bifurcation as particle size increased (or flow rate increased) and it hence decreased the number of particles traveling to lower generations. As a result, the lower flow rate was more efficient to transport larger particles (e.g. 15 to 20µm) to the second bifurcation as shown in Figure 6.29c and d. On the other hand, a higher flow rate was better in transporting smaller

particle (e.g. 1 to 10 μm) to lower bifurcations. Moreover, Figure 6.29b, e and f proved that mean Stokes number at the inlet is actually a good index of predicting DE. There are minor DE differences, however there are acceptable when the possible error (discussed in Model Validation) was taken into account.

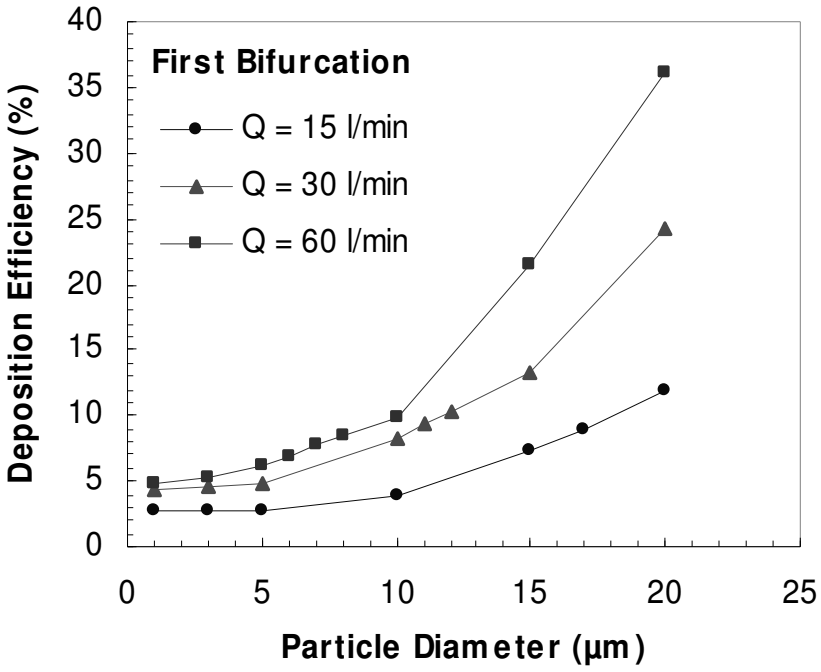

(a)

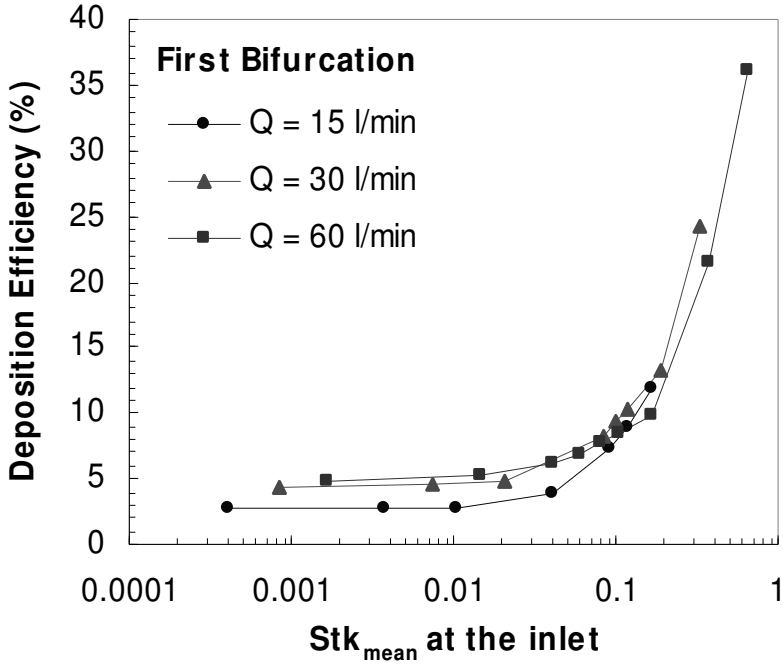
First Bifurcation
Q = 15 l/min
Q = 30 l/min
Q = 60 l/min
Deposition Efficiency (%)
0
5
10
15
20
25
30
35
40
0.0001
0.001
0.01
0.1
1
Stk mean at the inlet

(b)

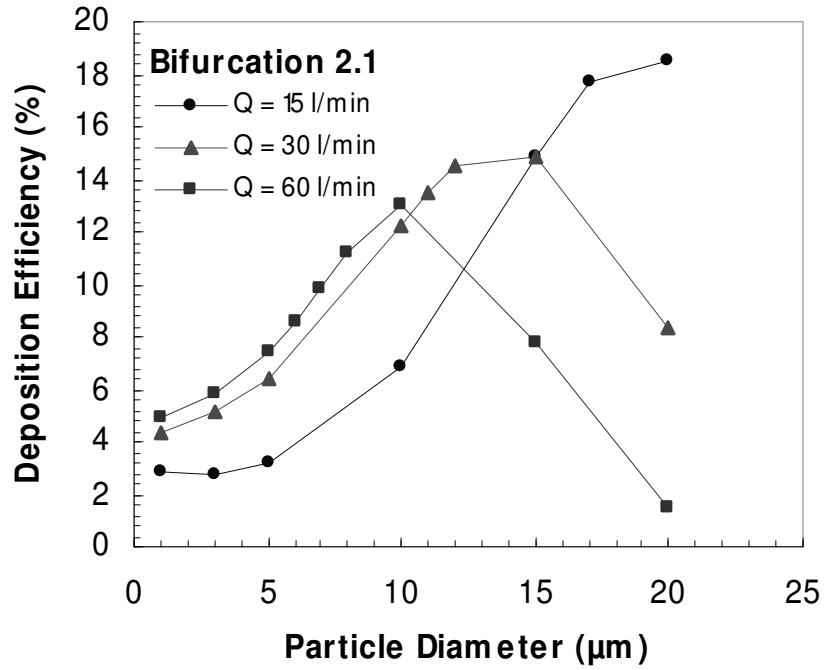
Bifurcation 2.1
Q = 15 l/min
Q = 30 l/min
Q = 60 l/min
Deposition Efficiency (%)
0
2
4
6
8
10
12
14
16
18
20
0
5
10
15
20
25
Particle Diameter (µm)

(c)

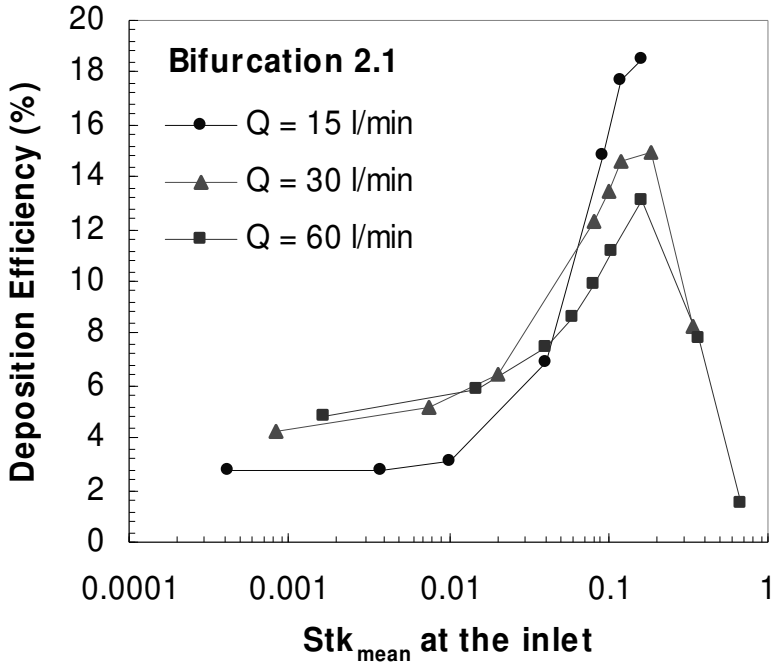
Bifurcation 2.1
Q = 15 l/min
Q = 30 l/min
Q = 60 l/min
Deposition Efficiency (%)
0
2
4
6
8
10
12
14
16
18
20
0.0001
0.001
0.01
0.1
1
Stk mean at the inlet

(d)

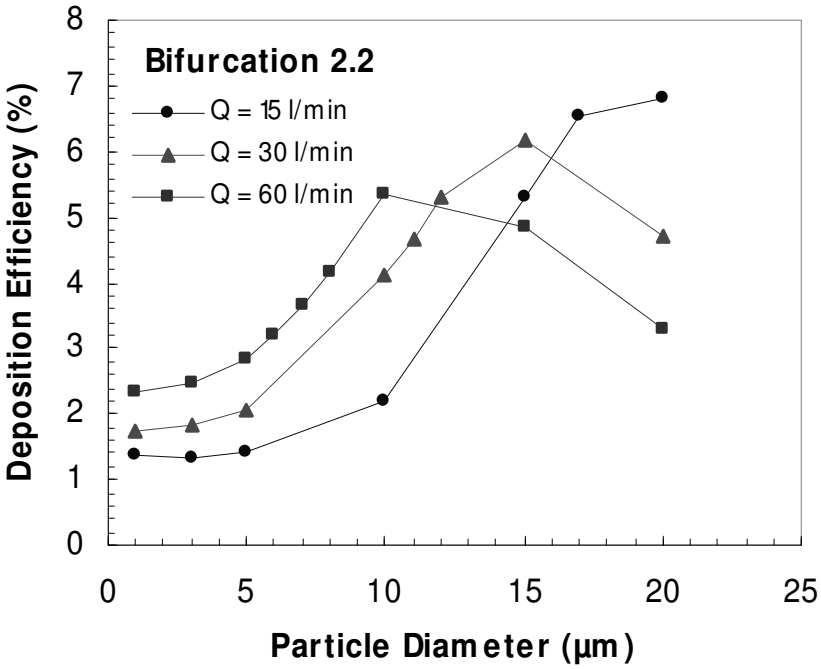
Bifurcation 2.2
Q = 15 l/min
Q = 30 l/min
Q = 60 l/min
Deposition Efficiency (%)
0
1
2
3
4
5
6
7
8
0
5
10
15
20
25
Particle Diameter (µm)

(e)

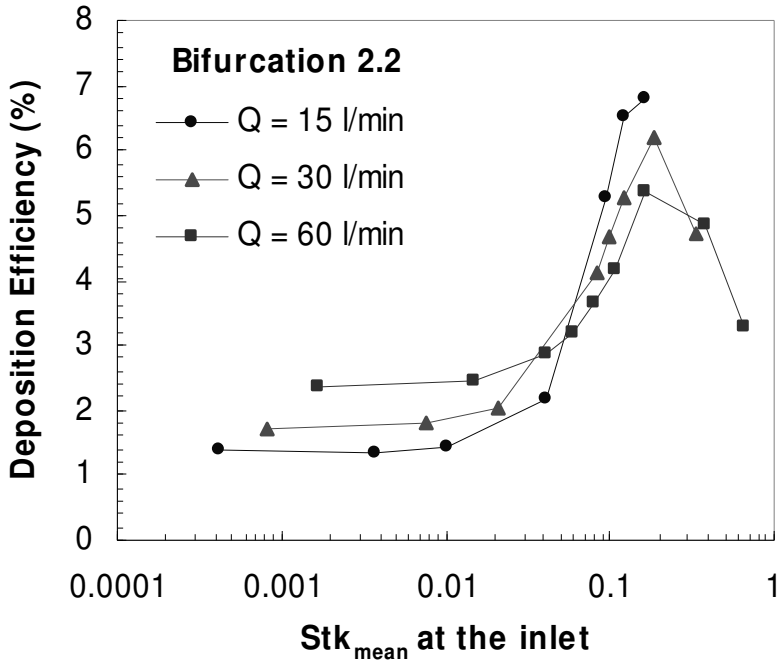

(f)

Fig. 6.29 Plot of deposition efficiencies for first bifurcation in the bifurcation airway model against particle diameter and mean Stokes number at the inlet

6.4.4 Particle deposition patterns at final stage

Four graphical deposition patterns were illustrated on a three-dimensional airway model using four typical respiratory conditions (combination of two flow rates and two particle sizes) as shown in Fig. 6.31 to 6.34. Although, the plot of DE against inlet mean Stokes number (St) already addressed the DE information in three typical locations (three bifurcations), the complete view of the deposition pattern can definitely help to investigate how the flow pattern affects the particle deposited into the airway in a more "viewable" term.

Figure 6.30 illustrates the total percentage of particles deposited into the wall of the whole airway model. It shows that over the whole model the DE did not have the

same characteristic as the DE in bifurcations in the plot of DE against St. Moreover, there was a large gap between the different flow rate's DE when St was less than 0.1. This is because the DE in the trachea and the first bifurcation dominated the DE in the whole model. Furthermore, DE in these two locations was especially sensitive to flow rate, rather than the particle size. Therefore, a high flow rate could directly increase DE in the trachea and the first bifurcation with no relation to Stokes number. This can be seen when two same Stokes number conditions were compared (Fig. 6.32, DE = 55% @ St 0.166; Figure 6.33, DE = 59% @ St 0.166). Both DE and St were almost the same, but the deposition patterns were markedly different, especially the pattern along the trachea.

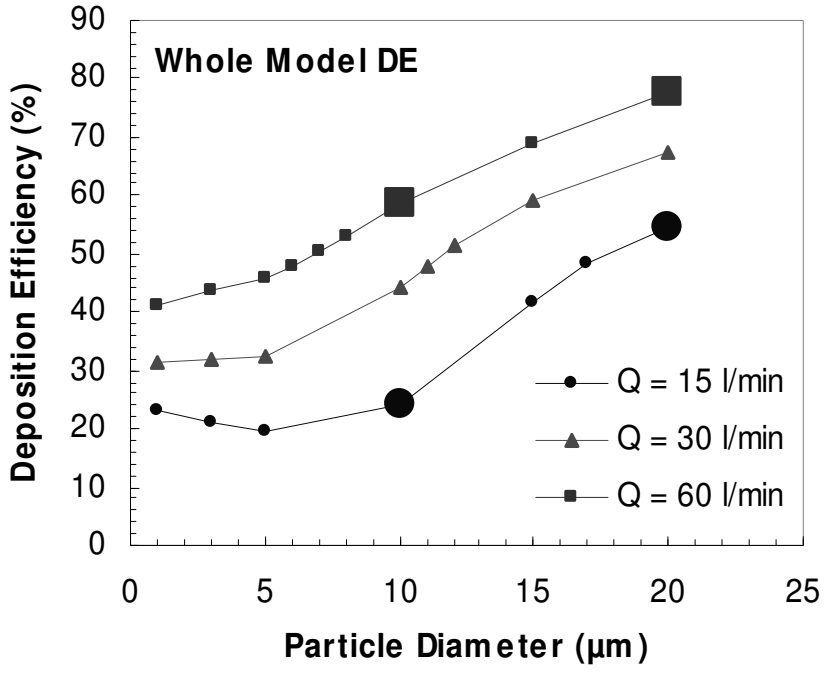

(a)

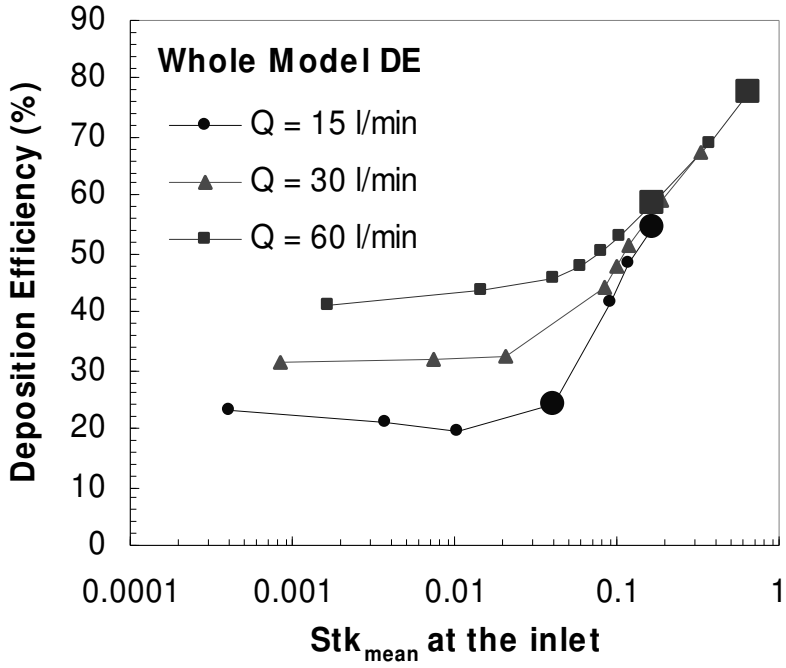

(b)

Fig. 6.30 Plot of deposition efficiencies in the whole bifurcation airway model against (a) particle diameter and (b) mean Stokes number at the inlet. Enlarged points represent four selected conditions as shown in Figure 6.31 to 6.34.

Figure 6.31 shows that the particles were diffused into every region quite evenly, although particle deposition was relatively concentrated in the bottom part of the airway due to air flow direction. Because of the low Stokes number, low DE in the whole model was expected as in Fig. 6.30. The axial velocity profile at station T6 in the trachea for 15 l/min flow rate demonstrated that the "M" shape velocity profile gave relatively high particle densities in both sides (B2.1 & B2.2) and low densities in the middle (B1). Correspondingly, the velocity profile at station Rb1 was moderate so that both the outside and the inside wall of second bifurcation (B2.1), as well as the carina ridge, collected noticeable amount of particles. At another side, the velocity profile at station Lb3 skewed slightly toward the bottom bronchus, but still retained a moderate velocity in the middle. As a result, the bottom left bronchus and the carina ridge

captured a higher amount of particles (see Box B2.2 in Fig. 6.32). These phenomena were more obvious in Fig. 6.32 where larger particles were injected with the same flow rate. The difference was that the locations mentioned contained higher particle densities and were less diffuse.

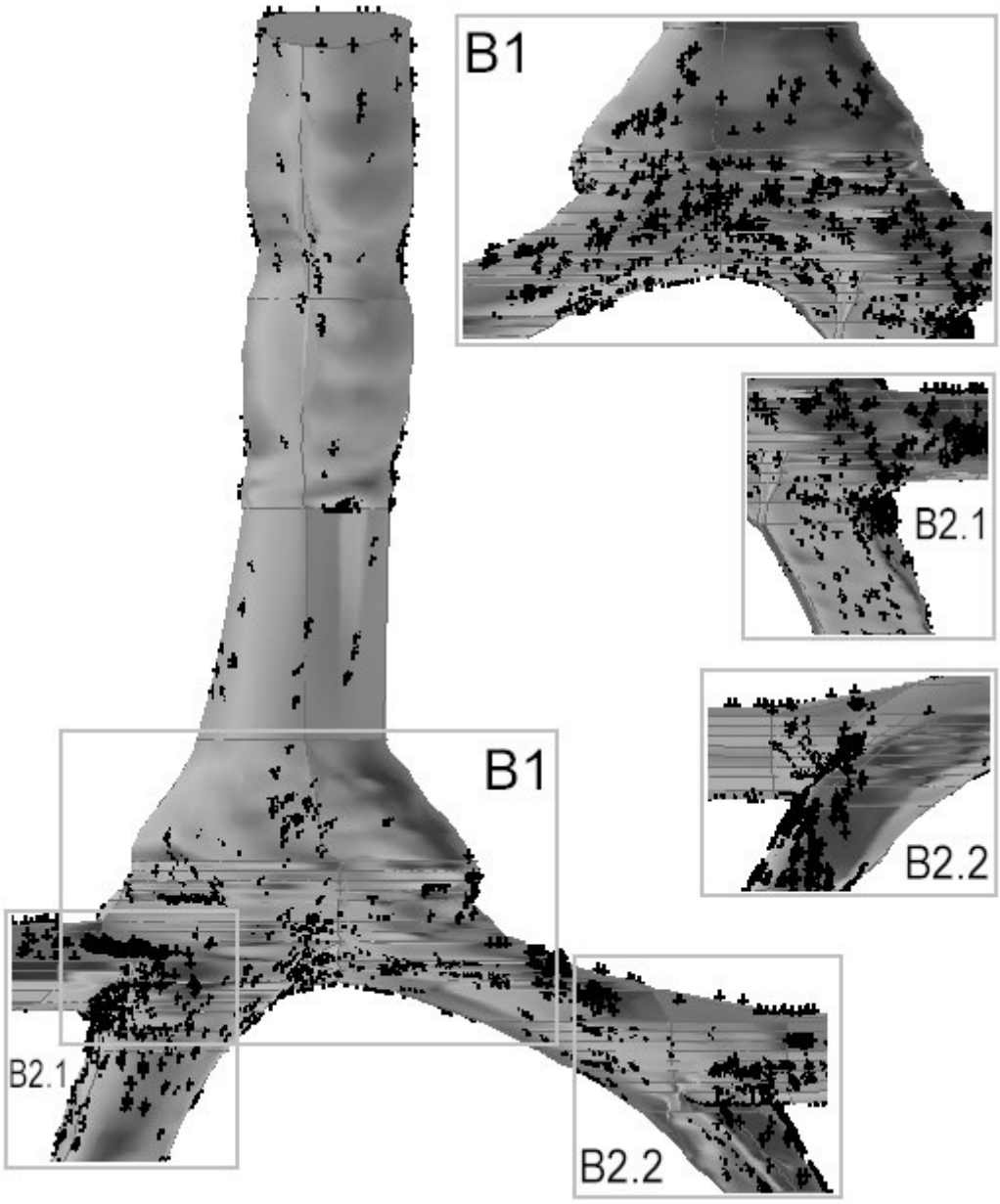

Fig. 6.31 Deposition pattern in front and back views for 15 l/min with particle diameter in 10 μm (St_{mean} = 0.042, Re_{mean} = 1447). Square windows are the back view of the bifurcations.

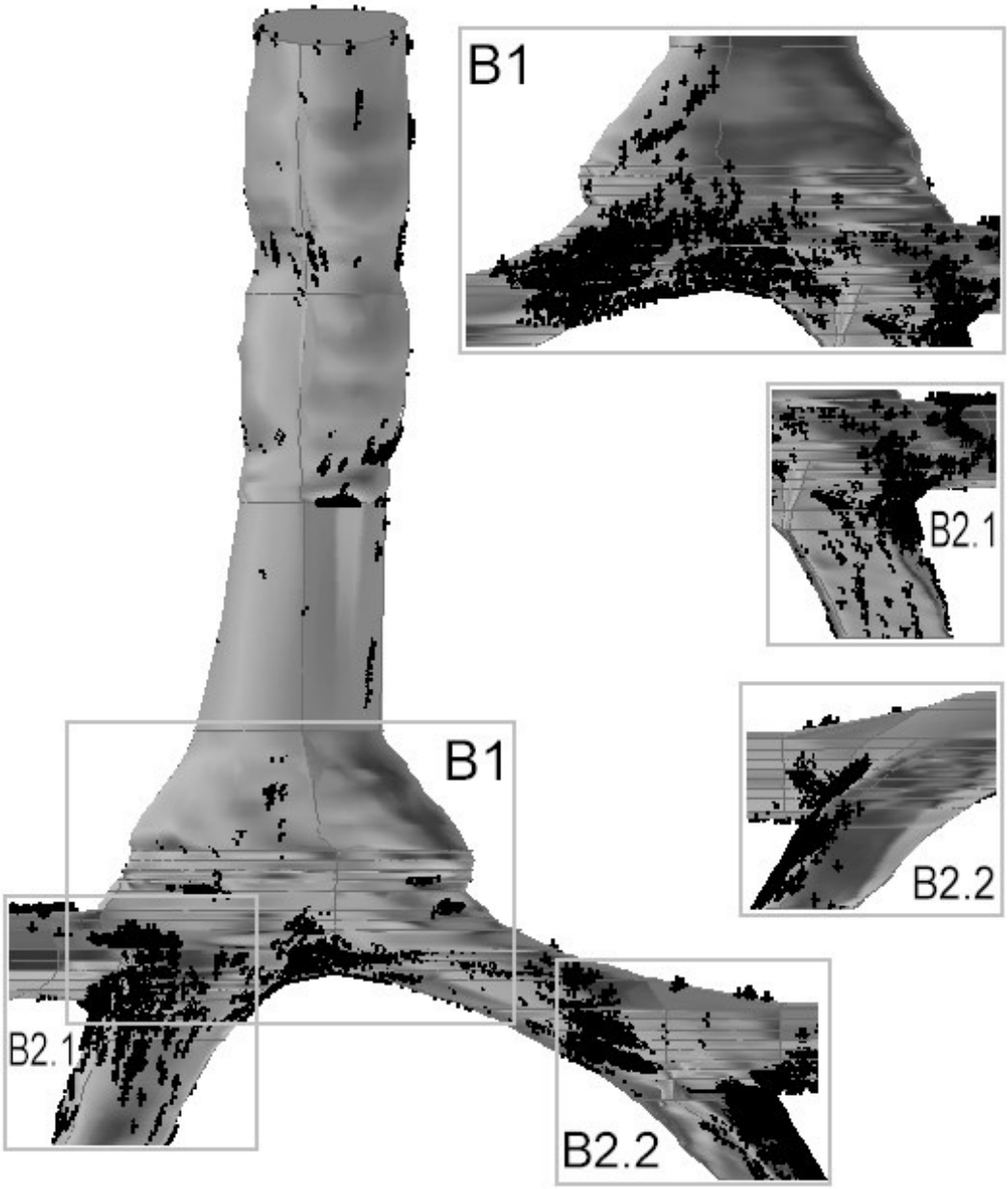

Fig. 6.32 Deposition pattern in front and back views for 15 l/min with particle diameter in 20 μm (St_{mean} = 0.166, Re_{mean} = 1447)

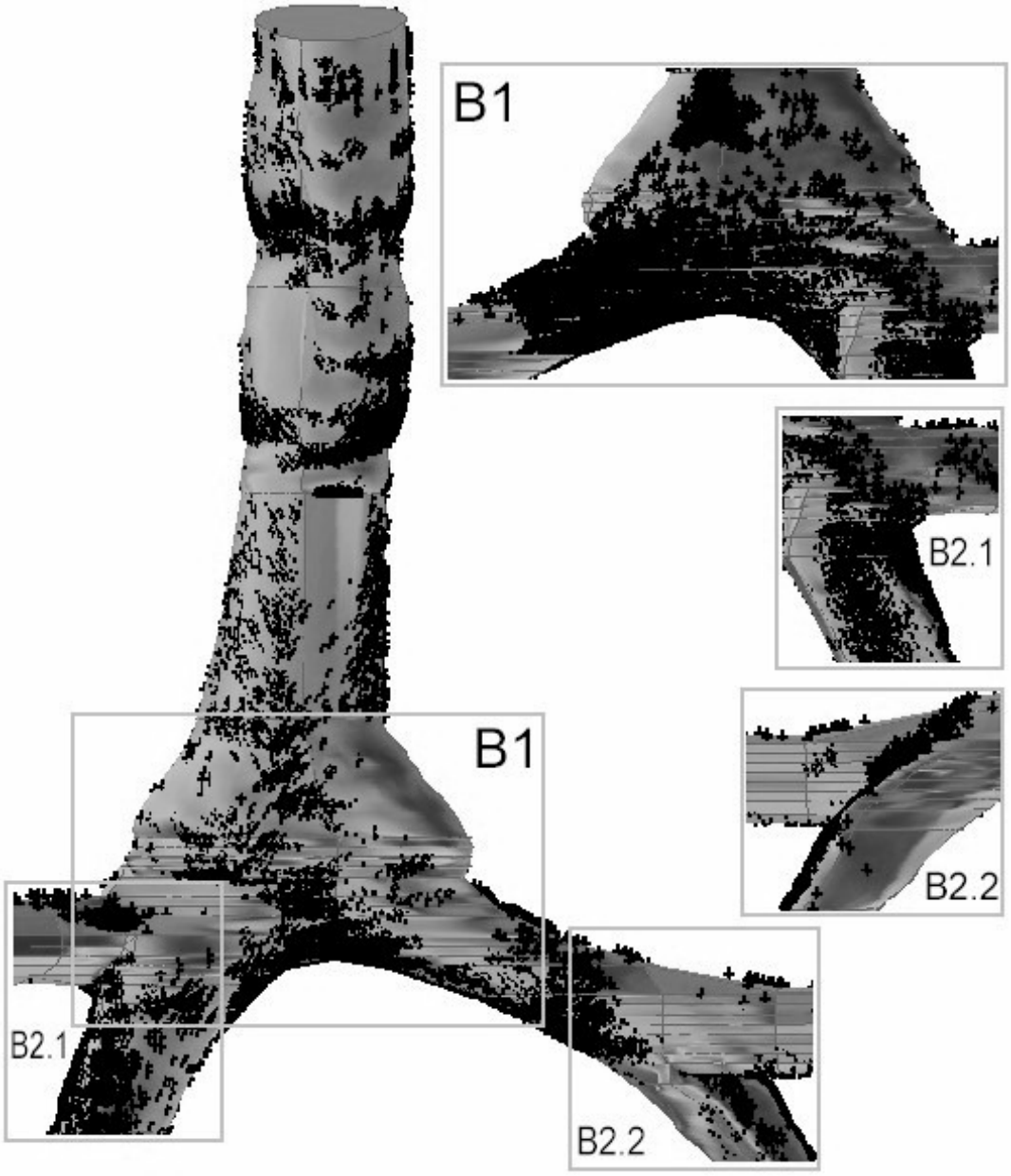

Fig. 6.33 Deposition pattern in front and back views for 60 l/min with particle diameter in 10 μm (St_{mean} = 0.166, Re_{mean} = 5789)

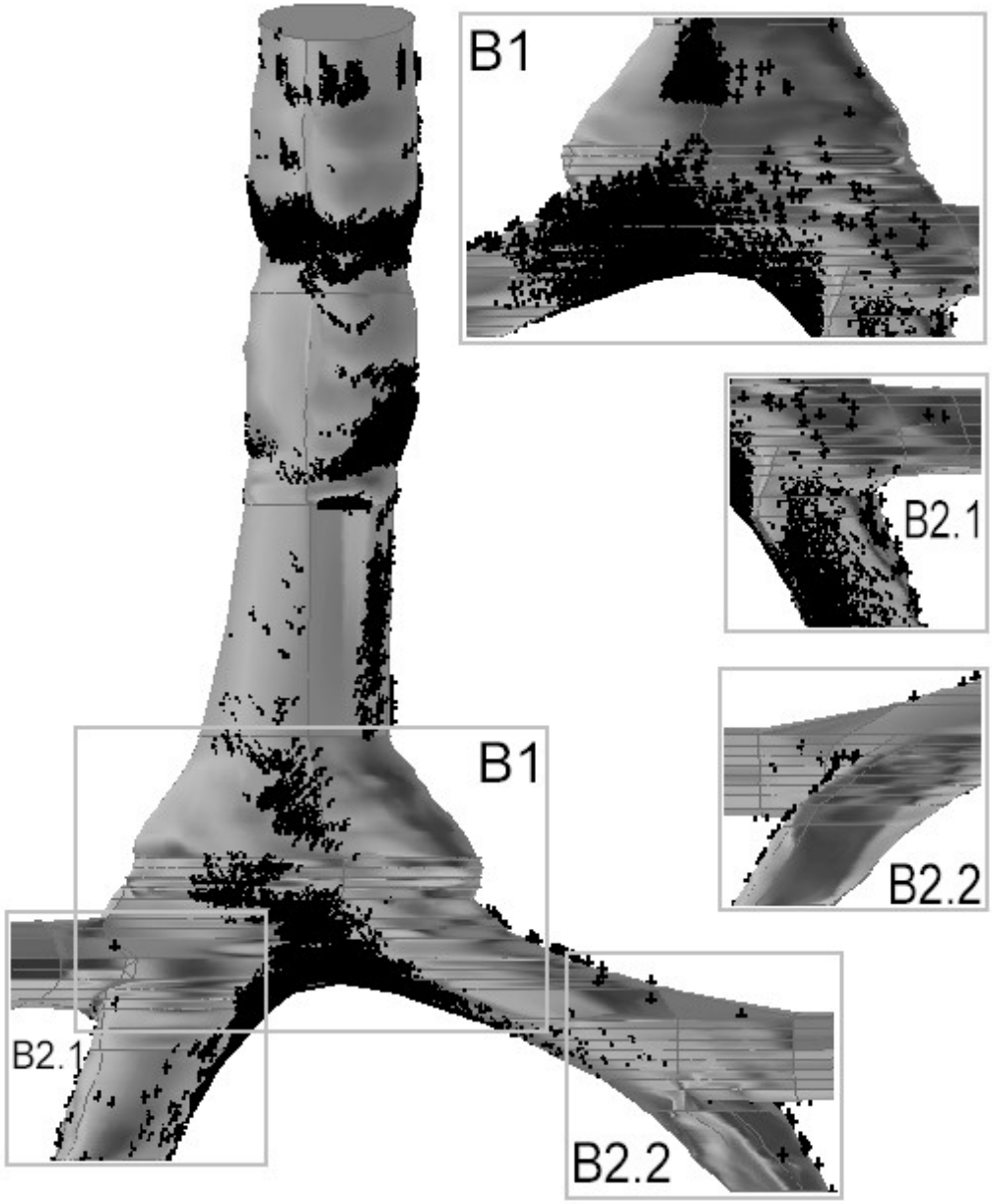

Fig. 6.34 Deposition pattern in front and back views for 60 l/min with particle diameter in 20 μm (St_{mean} = 0.665, Re_{mean} = 5789)

Figure 6.33 and 6.34 show that a high flow rate increased the chance for the region facing directly towards the flow to collect a larger amount of particles. When smaller particles were injected (Fig. 6.33), a diffusive phenomenon (not quite following the air flow direction) dominated the behavior of particle transportation. This was why

a large amount of particles deposited along the trachea. However, due to the moderate Stokes number, the model also contained high particle densities in all bifurcations and the inner wall leading down from the carina ridge in all bifurcations. On the contrary, when large particle injected, convective phenomenon (particle follow the air flow direction) became dominated. In addition, particle densities were more intensive and concentrated into smaller areas in the cartilaginous rings along the trachea, the first bifurcation and the inner wall leading down from the carina ridge in the first bifurcation as shown in Fig. 6.34. The condition shown in Fig. 6.34 seemed to capture fewer particles than in Fig. 6.33, but in fact, the total DE in the whole model in Fig. 6.34 was much higher (≈ 20%) than Fig. 6.33 as reflected in Fig. 6.30.

Chapter 7: Conclusions and Recommendations

7.1 Conclusions

The first outcome of this thesis presents a numerical and experimental study of the airflow in nasopharynx and pharynx using both RSM model and PIV techniques. The RSM turbulence model has shown to better capture the characteristics of strong secondary flow, anisotropy of shear stresses and curved streamline within the complex geometrical structure of realistic nasopharynx and pharynx airway generated by CT scan images. The flow patterns and velocity vectors obtained by Particle Image Velocimetry (PIV) was used to validate the RSM results. The results demonstrate that the RSM is capable of capturing the characteristics of complex flow patterns in human airway.

The topography of velocity, turbulent kinetic energy and WSS in the airway was predicted by RSM under normal breathing conditions. The RSM model revealed a substantial difference in both of the magnitude and spatial distribution of the velocity, turbulent kinetic energy and WSS values everywhere within the airway. This study particularly showed the existence of high WSS values that also concurred with high velocities and turbulent kinetic energy levels in the pharynx region. The presence of high WSS in the pharynx region are anatomic locations predisposed for possible lesion development. These lesions on the layers of soft tissues surrounding the pharynx region expose the surfaces to possible infection and inflammation especially for cases of heavy smoking, which can probably lead to the risk of contracting cancer because of the formation of malignant tumors. Results indicated that the dominant high WSS values

can reach a maximum of 0.5 Pa and 10 Pa for low and high inhalation activities at the pharynx.

Secondly, particle depositional studies from nasal sprays are important for efficient drug delivery. The main influences on deposition involve the nasal cavity geometry and the nasal spray device of which its parameters are controlled by the product design. It is known that larger particle sizes (>>10 μm) at a flow rate of 333 ml/s impact in the anterior portion of the nose, leaving a significant portion of the nasal cavity unexposed to the drugs. Studies have found correlations for the spray cone angles and particle sizes with deposition efficiencies. This study extends these ideas to incorporate other parameters such as the insertion angle of the nasal spray and the injected particle velocity to observe its effect on deposition. A numerical method utilizing a particle tracking procedure found that the most important parameter was the particle's Stokes number which affected all other parameters on the deposition efficiency.

Thirdly, a prediction of particle deposition efficiency through an inertial and viscous regime in a porous model vestibule region of the nasal cavity is described. For the porous filter media with uniform isotropic permeability, Darcy's law is used to describe the pressure-velocity relationship. Deposition efficiency was calculated for mono-sized particles of aerodynamic diameter between 0.5 and 100µm under constant inspiratory flow rate of 12 l/min. It was found that the inclusion of a porous region in the nasal vestibule region contributes to a significant increase in the deposition efficiency as well as causing a forward shift in the area averaged velocity pattern of the fluid. Information on the deposition efficiency of aerosol particles in the nasal airways

is used for both optimizing the delivery of therapeutic aerosols into the nose and risk assessment of toxic airborne pollutants inhaled through the nose into the respiratory system.

Finally, Velocity profiles, local deposition efficiencies (DE) and deposition patterns of aerosol particles in the first three generations (i.e. double bifurcations) of an airway model have been simulated numerically, in which the airway model was constructed from CT scan data of real human tracheobronchial airways. Three steady inhalation conditions, i.e., 15, 30 and 60 l/min, were simulated and a range of micron-particle sizes (1-20 μm diameters) were injected into the model. Results were then compared with experimental and other numerical results which had employed either similar model geometry or test conditions. The effects of inhalation conditions on velocity profiles and particle deposition were studied. The data indicated that the local deposition efficiencies in the first bifurcation increased with a rise in the Stokes number (St) within St range from 0.0004 to 0.7. Within the same St range, DE in the second bifurcations (both left and right) was dropped dramatically after St increased to 0.17. Also, the second bifurcation in the right side (B2.1, closer to first bifurcation than left side, B2.2) was found to show a much higher (almost double) DE than the left side. This may be due to the fact that the left main bronchus is longer and has greater angulation than the right main bronchus.

7.2 Recommendations

This CFD study examined the incorporation of a simple porous model to emulate the nasal hair growth by assuming virtual pore holes inside the vestibule region. Given the complexity of the geometry it was considered to include only the

laminar flow in the porous-model. The results suggest that the inclusion of the porous-model significantly increased both local and total deposition inside the nasal cavity and pharynx. For the non-porous model the velocity of the fluid and particles were found to decrease, but were found to increase in the porous model. Decrease in porosity contributes to an increase in deposition in the anterior region and also caused a forward shift in the pattern of the local deposition efficiency. The one-way coupling used in this model accounted for an inertial loss on the particle motion and that increased with an increase in particle size.

Considering these preliminary results, it can be seen that there is a need to further investigate the use of a porous medium to enhance our knowledge of the mechanisms of targeted delivery of therapeutic sprays and also to study the impact of environmental pollution in the nasal cavity. Though these predictions form a basis of fundamental understanding, experiments are required to validate the model. The Large Eddy Simulation (LES) turbulence model could also be incorporated for higher flow rates. These unresolved issues form a foundation for our continued research.

Several assumptions were made when carrying out this analysis and these has limited the present work to extrapolatable to real world scenarios. In terms of simulation, gravitational force is neglected and only constant particle entrance profile is studied. In anatomical and physiological terms, larynx and generations after third generations are excluded and thus, the larynx effect and effects of flow on upstream airways from additional downstream bifurcations are neglected. Only one constant inhalation is considered but in reality, tidal and cyclic breathing was proved to have

great effect in particle deposition. As a result, further study should import user define functions to simulate these inlet boundaries.

References

Balásházy, I., Hofmann, W., and Heistracher, T. 2003. Local particle deposition patterns may play a key role in the development of lung cancer. *Journal of Applied Physiology.* 94:1719-1725.

Chang, H. K., and El Masry, O. A. 1982. A model study of flow dynamics in human central airways. Part I: Axial velocity profiles. *Respiration Physiology.* 49:75-95.

Cheng, Y.S., Holmes, T.D., and Gao, J., 2001, Characterization of nasal spray pumps and deposition pattern in a replica of the human nasal airway. *J. Aerosol Med,* 14, 267-280.

Clark, A.R. 1995. The use of laser diffraction for the evaluation of the aerosol clouds generated by medical nebulizers. *International Journal of Pharmaceutics.* Volume 115, Issue 1, 69-78.

Crowe, C., Sommerfeld, M., and Tsuji, Y. (1998). *Multiphase Flows with Droplets and Particles, CRC Press LLC p. 25.*

Daily, J. W., and Harleman, D. R. F. 1966. *Fluid Dynamics*. New York, US: Addison-Wesley.

Frey, J.M., Schmitz, P., Dufreche, J., and Gohr Pinheriro, I., 1999, Particle deposition in porous media: analysis of hydrodynamic and weak inertial effects. *Transport in porous media,* 37, 25-54.

Girardin, M., Bilcen, E., and Arbour, P., 1983, Experimental study of velocity fields in a human nasal fossa by laser anemometry. *Ann. Otol. Rhinol. Laryngol*. 92: 231-236.

Hahn, T., Scherer, P.W., and Mozell, M.M., 1993, Velocity profiles measured for air flow through a large-scale model of the human nasal cavity. *J. Appl. Physiol,* 75, 2273-2287.

Haußerman, S., Bailey, A. G., Bailey, M. R., Etherington, G., andYoungman, M. 2002, The influence of breathing patterns on particle deposition in a nasal replicate cast, *J. Aerosol Sci.* 33:923–933.

Hornung, D.E., Leopold, D.A., Youngentob, S.L., Sheehe, P.R., Gagne, G.M., Thomas, F.D., Mozell, M.M., 1987, Airflow Patterns in a Human Nasal Model. *Arch Otolaryngol Head Neck Surg.* 1987;113(2):169-172.

Horschler, I., Meinke, M., and Schr¨oder, W. 2003, Numerical Simulation of the Flow Field in a Model of the Nasal Cavity, *Comput. Fluids.* 32:39–45.

Horsfield, K.,1974, The relation between structure and function in the airways of the lung, *British Journal of Diseases of the Chest*, Volume 68, 1974, Pages 145-160

Kelly, J. T., Asgharian B., Kimbell, J. S., and Wong, B. A. 2004, Particle Deposition in Human Nasal Airway Replicas Manufactured by Different Methods. Part 1: Inertial Regime Particles, *Aerosol Sci. Technol.* 38:1063–1071

Kim, C. S., and Fisher, D. M. 1999. Deposition characteristics of aerosol particles in sequentially bifurcating airway models. *Aerosol Science and Technology.* 31:198-220.

Kreuzer, M., Muller, M. K., Brachner, A., Gerken, M., Grosche, B., Wiethege, T., and Wichmann, H. E. 2000. Histopathologic findings of lung carcinoma in German uranium miners. *Cancer* 89:2613-2621.

Launder, E., and Spalding, D. B. (1974). The numerical computation of turbulent flows. *Computing Methods Appl Mech Eng*. 3:269-289.

Lien, F.S, and Leschziner, M.A, 1994, Assessment of turbulence-transport models including non-linear rng eddy-viscosity formulation and second-moment closure for flow over a backward-facing step. *Computers & Fluids*, Volume 23, Issue 8, November 1994, Pages 983-1004

Mygind, N., and Dahl, R., 1998, Anatomy, physiology and function of the nasal cavities in health and disease. *Adv. Drug Delivery Rev,* 29, 3-12.

Pope, C. A., Dockery, D. W., and Schwartz, J. 1995. Review of epidemiological evidence of health effects of particulate air pollution. *Inhalation Toxicology.* 7:1-18.

Proctor, D.F. 1982, The mucociliary system. In: the Nose, Upper Airway Physiology and the Atmospheric Environment, pp.245-278. Elsevier, Amsterdam.

Schlesinger, R. B., Gurman, J. L., and Lippmann, M. 1982. Particle deposition within bronchial airways: Comparisons using constant and cyclic inspiratory flows. *Annals of Occupational Hygiene.* 26:47-64.

Shih, TH, Liou, WW, Shabbir, A, Yang, ZG, & Zhu, J 1995, 'A new k-ε eddy viscosity model for high Reynolds number turbulent flows', *Computers & Fluids*, Vol. 24, pp. 227-238.

Schroter, R.C. and Sudlow, M.F., 1969, Flow patterns in models of the human bronchial airways, *Respiration Physiology*, Volume 7, Issue 3, October 1969, Pages 341-355

Smith, S.J., Bernstein J.A. 1996, Therapeutic uses of lung aerosols. In: Inhalation Aerosols: Physical and Biological Basis for Therapy, pp.233-247. Marcel Dekker, New York.

Stapleton, K.W., Guentsch, E., Hoskinson, M.K., and Finlay, W.H., 2000, On the suitability of *k-ε* turbulence modeling for aerosol deposition in the mouth and throat: a comparison with experiment, *J. Aerosol Sci.* Vol 31, No. 6, pp. 739-749.

Swift, D. L. 1991, Inspiratory Inertial Deposition of Aerosols in Human Nasal Airway Replicate Casts: Implication for the Proposed NCRP Lung Model, *Rad. Prot. Dosimetry* 18(1/3):29–34.

Swift, D.L., Proctor, D.F, 1967, Human respiratory deposition of particles during oronasal breathing, *Atmospheric Environment (1967)*, Volume 16, Issue 9, 1982, Pages 2279-2282 Yakhot, V, & Orszag, SA 1986, 'Renormalization group analysis of turbulence i. basic theory', Journal *of Scientific Computing*, Vol. 1, pp. 3-51.

Zhang, Y., Finlay, W. H., and Matida, E. A. 2004, Particle Deposition Measurements and Numerical Simulation in a Highly Idealized Mouth-Throat, *J. Aerosol Sci.*, 35:789–803.

Zhang, Y., and Finlay, W. H. 2005. Measurement of the effect of cartilaginous rings on particle deposition in a proximal lung bifurcation model. *Aerosol Science and Technology.* 39:394-399.

Zwartz, G. J., and Guilmette R. A. 2001, Effect of Flow Rate on Particle Deposition in a Replica of a Human Nasal Airway, *Inha. Toxicol.* 13:109–127